17th INTERNATIONAL CONGRESS
of the Geological Society of Greece

BULLETIN OF THE GEOLOGICAL
SOCIETY OF GREECE, SP. PUBL.

EXTENDED ABSTRACT 116

Integrating Geotechnical Data and Site Response Analyses in the Municipality of Chalandri, Athens, Greece

Ioannidou Despoina Civil Engineer T.E. MSc, d.ioannidou12@gmail.com, CLPW, Athens, Greece & University of the Aegean, Greece
Ktenidou Olga – Joan Civil Engineer, PhD, Researcher National Observatory of Athens, Greece

ABSTRACT: I

n this work, the properties and the dynamic response of the soil formations in the area of Chalandri are investigated. Its main points are the collection and synthesis of all available data from 92 sampling boreholes, the estimation of shear velocity (Vs) through empirical correlations, the 1-D dynamic analysis of soil profiles modelled from 42 borehole locations, the zonation of the area according to site response and the production of maps showing the spatial distribution of the main characteristics of ground motions (fundamental period and amplification factor). Finally, these results were correlated with the building damage caused by the 1981 earthquake in Alkyonides.

INTRODUCTION

Local soil conditions are one of the most important factors determining the strong ground motion and consequently the seismic hazard at a specific location. Site effects have been known to modify the duration, amplitude and frequency content of ground shaking. The most commonly considered case is that of increased amplitude at specific frequencies related to the material properties (e.g. shear-wave velocity) and geometry (e.g. layer thickness), which is referred to as site amplification. Simpler cases refer to simple soil layers over bedrock while more complex ones include basin edges, topographic features, and other cases of lateral discontinuities (Bard, 1999, (Kausel & Roesset, 1984), (Pitilakis et al, 1999a) (Chavez-Garcia et al, 2000), (Raptakis et al, 2005).

The present work, which is the result of postgraduate work within the framework of the inter-institutional postgraduate program "Natural Hazards and Disaster Management" (co-organized by the University of the Aegean, the Aristotle University of Thessaloniki and the National Observatory of Athens), aims to utilize as much as possible the available information for an initial assessment of the seismic response at a large number of points in the Municipality of Chalandri, taking into account the influence of local soil conditions and their change within the area. The Municipality of Chalandri was chosen as a study area due to its size and population, but also due to the availability of a large number of data that remained unexploited for decades.

COLLECTION AND PROCESSING OF GEOTECHNICAL AND GEOPHYSICAL DATA

An extensive effort to collect data and technical information from boreholes and geotechnical surveys carried out in past decades for the Municipality of Chalandri in the Prefecture of Attica. This search, resulted in the discovery of 10 geotechnical surveys consisting of 92 sampling boreholes, which occupy most of the Municipality (as it was defined in earlier days, before its extension north), and one cross-hole test site (figure 1).

All boreholes and geotechnical surveys were drawn from the project archive of the "Geotechnical Engineering and Geology" department of the Central Laboratory of Public Works (TGMT/KEDE/YPOME).

The geological background of the Municipality of Chalandri is structured by alpine formations ('Allochthonous Unit of Attica" which includes the 'Athenian Schists" and the 'Upper Cretaceous Limestones") which are covered by significantly thick Post-alpine formations, (Lekkas et al., 1999). The Post-alpine formations are represented by Neogene and Quaternary sediments. The Neogene sediments found in Chalandri are continental formations of Upper Miocene age. (Mariolakos & Fountoulis, 2002). The Quaternary deposits that overlie all of the previous formations are loose deposits from river alluvium, of mixed phase.

From the processing and evaluation of the data from the boreholes, it became possible to distinguish the soils into three soil units I, II, III. These units represent the geological formations of the subsoil of Chalandri and are categorized into geotechnical units Ia, Ib, Ic for the Quaternary deposits and IIa, IIb for the Neogene sediments (Upper Tertiary deposits). This distinction was the result of the evaluation of the physical and geotechnical properties of the soil materials, with the aim of grouping them into specific units, characterized by a certain framework of homogeneity in terms of their mechanical behavior. The geotechnical units (Ia, Ib, Ic) consist of alternations of sandy clay with clayey silty sand and gravels of clayey composition. Unit IIb consists of lean and fat clay and unit IIa consists of marls which overlie unit IIb. Finally, unit III represents the rocky bedrock of the municipality, which consists mainly of clayey shale and cohesive shale (Table 1).

After the thorough recording and detailed statistical processing of 793 samples and 2734 tests, which included data from tests of physical properties (grain size distribution analysis, Atteberg limits, etc.), mechanical properties (unconfined compressive strength, etc.), the SPT standard penetration test, the Chalandri area is characterized by a general geotechnical section, which consists of recent deposits (manmade fill, sandy clays, sandy silts, sandy gravels), of Upper Tertiary deposits consisting mostly of reddish-brown sandy clay and interspersed in places with layers of clayey marl and loose conglomerates and bedrock, which consists of Athenian Schist, limestone and cohesive conglomerates.

The difference seen in the processing of geological and geotechnical data is the progressive increase in the thickness of the Upper Tertiary deposits and correspondingly the increase in the depth of the rocky bedrock (Figure 2).

Therefore, according to this important detail, the area was divided, depending on the depth of the rocky bedrock, into six (6) zones, which are: Zone A: 0 – 5m., Zone B: 5 – 10m., Zone C: 10 – 20m., Zone D: 20 – 30m., Zone E: 30 – 40m. and Zone ST: >40m. (Figure 3). There is a clear NNW-SSE trending boundary in the zonation map which represents the Chalandri fault (Christoulas, et al 1983), and marks an abrupt change in sediment thickness either side.

It is worth noting that no rocky bedrock was found in zone ST, although the deepest drillings exceeded the drilling depth of 70m. Also, zone ST was deemed appropriate to be divided into two subzones (subzone ST and ST_1), which present a differentiation in terms of stratigraphy. Specifically, subzone ST_1 consists of layers of conglomerates and marls before the reddish-brown sandy clay which is the main material of the Upper Tertiary deposits.

Figure 1: Locations of 92 sampling boreholes

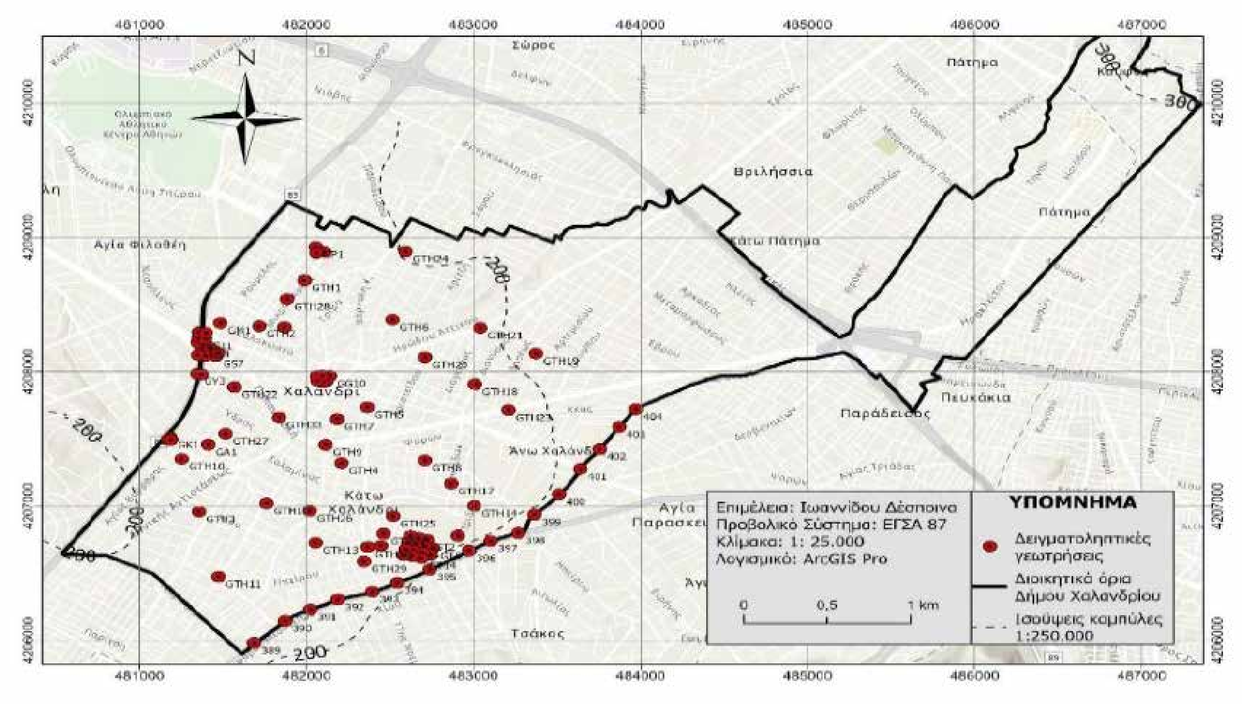

Table 1: Definition of geological – geotechnical units

GEOLOGICAL UNIT	GEOTECHNICAL UNIT	DESCRIPTION OF GEOTECHNICAL UNIT
Quaternary deposits I	A	Manmade fill
	Ia	Brown, reddish brown, yellow brown, white brown, brownish brown silty clay SAND
	Ib	Brown, reddish brown, yellow brown, ash brown sandy CLAY
	Ic	Brown, reddish brown, brownish-ash silty clayey GRAVEL
Upper Tertiary deposits II	IIa	Brown, brownish-yellow clay MARL
	IIb	Reddish brown CLAY with sand
Bedrock III		Red, brownish-ash, ash yellow CONGLOMERATES Brownish-ash, ash yellow, ash green, ash, brownish-brown CLAY SHALE and reddish, whitish-brown LIMESTONE

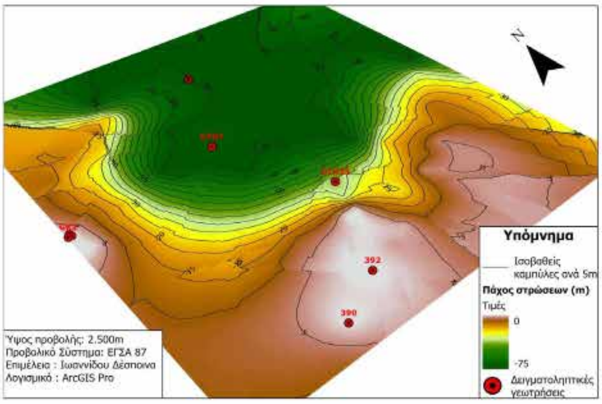

Figure 2: Spatial distribution map of layer thickness

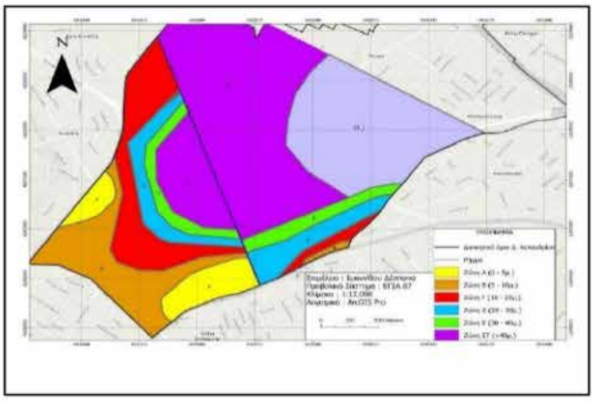

Figure 3: Division of study area into zones according to depth of bedrock

STUDY OF SEISMIC RESPONSE OF SOIL FORMATIONS

The shear wave propagation velocity Vs, in soil formations, due to the lack of a sufficient number of geophysical tests, was estimated approximately through the very extensive data of the standard penetration test Nspt (621 tests). After reviewing the literature and comparing a large number of relationships, the following empirical relationships were selected, from studies in Greek soils.

(Raptakis, et al 1994)

$Vs\ (m/sec) = 99.95\ (N_{60})^{0.237}$ (Medium – Dense sands, Nspt>10) (1)

$Vs\ (m/sec) = 192.41\ (N_{60})^{0.131}$ (Gravel soils) (2)

$Vs\ (m/sec) = 10.78\ (N_{60}) - 299.3$ (Marls) (3)

(Athanasopoulos, 1995)

$Vs\ (m/sec) = 85.3\ (Nspt)^{0.42}$ (Gravel soils) (4)

(Tsiabaos & Sabatakakis, 2011)

$Vs\ (m/sec) = 112.2\ (N_{60})^{0.324}$ (Clay soils and marls) (5)

$Vs\ (m/sec) = 79.7\ (N_{60})^{0.365}$ (Sandy soils) (6)

For soils consisting of clays, Vs was estimated approximately by the empirical correlation of the results of the single cross-hole test with the average of the Nspt blows for the corresponding depths of the cross-hole test values, of all the projects under study through the following relationship:

$Vs\ (m/sec) = 7.39\ (Nspt)^{0.95}$ (7)

The data and the trend line for relationship (7) are shown in figure 4.

Figure 4: Correlation between Nspt and Vs values for clays (Nspt>8) (left) and normalized consistency ratio $C_{(d)}$ (right).

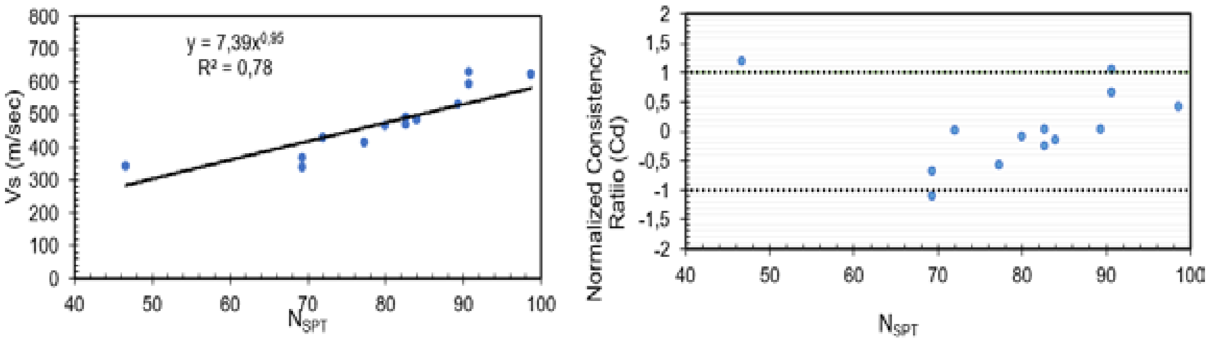

The normalized coherence ratio C(d) is given by equation 8:

$C(d) = (Vsm – Vsc) / Nspt$ (8)

where Vsm are the measured values from the cross-hole test, Vsc are the calculated values from equation (7), and Nspt are the uncorrected values of the SPT blows. Figure 4 (right) shows the comparison between the Vsm and Vsc values. The C(d) values appear close to 0, which means that the proposed equation performs well in predicting Vsc (Table 2).

The Vs adopted for the bedrock of Chalandri is 1600 m/sec for the clayey shale of Athens (Koukis & Sabatakakis, 2000). For the seismic bedrock of zones ST and ST_1 the shear velocities adopted are 750 m/sec and 850 m/sec respectively, values representative of very hard soils and sandy clays (Chen & Ong, 2012), (Jia, 2018).

In every location of the soil profiles analyzed, the average mass density of the rocky bedrock was assumed to be equal to 23 kN/m3 (Koukis & Sabatakakis, 2000) while the seismic bedrock (zone ST and ST_1) was assumed to be 22 kN/m^3 since no harder formation has been found in this zone and the average density value for the Upper Tertiary deposits was calculated to be 22 kN/m^3. The hysteretic damping ratio was assumed to be equal to 2% for the rocky-seismic bedrock and 3% for the soil layers overlying the bedrock.

Table 2: Average SPT blow counts and shear wave velocities Vs for the geotechnical units of the Municipality of Chalandri

GEOTECHNICAL UNIT	Nspt	N_{60}	Raptakis et. al (1994)	Tsiambaos G. et. al (2010)	Average price	Average price	Raptakis et. al (1994)	Athanasopoulos G.A. (1995)	Average price	Raptakis et. al (1994)	Tsiambaos G. et. al (2010)	Average price	Resulting empirical relationship N_{spt}	Resulting empirical relationship N_{60}	Average price
			Medium to dense sands	Sandy soil			Gravelly soil	Gravelly soil		Marls	Marls		Clayey soil	Clayey soil	
			$Vs=99.95N_{60}^{0.237}$	$Vs=79.7N_{60}^{0.365}$			$Vs=192.41N_{60}^{0.131}$	$Vs=85.3N_{spt}^{0.42}$		$Vs=10.78N_{60}-299.3$	$Vs=112.2N_{60}^{0.324}$		$Vs=7.39N_{spt}^{0.95}$	$Vs=9.71N_{60}^{0.95}$	
A	51	38	237	301	**269**	**271***									
Ia	53	40	240	306	**273**										
Ib	57	43											344	346	**345**
Ic	60	45					317	476	**396**						
IIa	87	65								401	434	**418**			
IIb	101	76											593	594	**593**

*Because geotechnical units A and Ia have similar geotechnical properties and the average velocities Vs estimated are practically the same, for reasons of simplification of the seismic analysis, the two units were merged.

The seismic excitation used for the analysis of the seismic ground response is the Athens earthquake of September 7, 1999, with a magnitude of Mw 5.9. The accelerogram chosen as the input motion was recorded at the DMK station (EKEFE Demokritos) of the National Earthquake Research Center in the area of Agia Paraskevi (NOA, 1975) and had an epicentral distance from the rupture of 25 km (esm-db.eu, Luzi et al., 2020) (figure 5). This station was chosen because it is the only one in the vicinity that lies on rock conditions. Figure 6 shows the acceleration time series at DMK station, as well as the acceleration response spectrum in the 3 components of the recording.

After merging similar soil profiles, 42 soil profiles were solved in the Chalandri area using 1D equivalent linear analysis method with the DEEPSOIL software (Hashash et al., 2020). According to this method, for any seismic excitation, the differential equations are solved using Fourier analysis in the frequency domain. Using this model and the corresponding geotechnical and dynamic properties and layer thicknesses for each zone, the corresponding transfer functions were calculated for each soil profile (Figure 7, where the groups of transfer functions for zones A, C, ST and the corresponding response spectra for damping ratio of ξ=5%, i.e. for a reinforced concrete structure, are shown).

Figure 5: Location of the DMK accelerometer (red cicle)

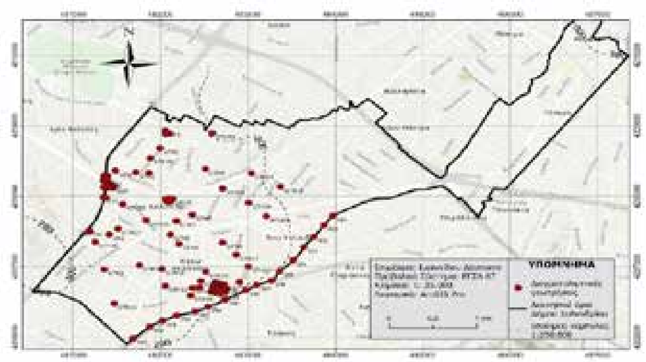

Figure 6: Acceleration time series and response spectra at DMK station

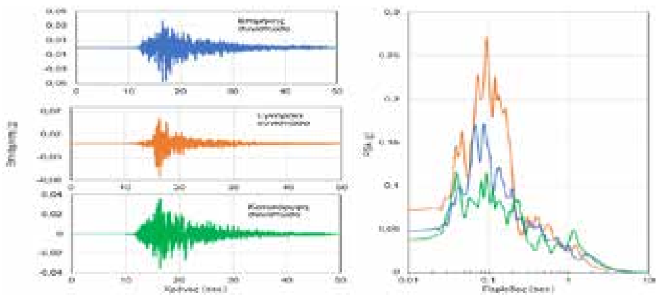

Figures 8 and 9 show the spatial distribution of the fundamental period T0 and the amplification factor in this period A0. Among the calculated values, the other values were estimated using the spatial interpolation method "Krigging". The maps, in addition to the spatial distribution of the above parameters, also show the locations of the buildings that suffered significant damage from the 1981 Alkyonides earthquake (Christoulas et al., 1983). Also shown are the EC8 soil categories for each soil profile as calculated from the relation for shallow seismic profiles (>30m):

Log Vs 30 = (a + b) log (Vs (d))¯(Boore, 2004) (9)

where Vs (d), the average velocity value for a soil profile depth of less than 30 m, a and b, coefficients for each 1m. from 10m. to 29m.

Figure 7: Transfer functions (left) and response spectra (right) computed from the 1D analyses at each borehole location within each zone (zones A,C,ST)

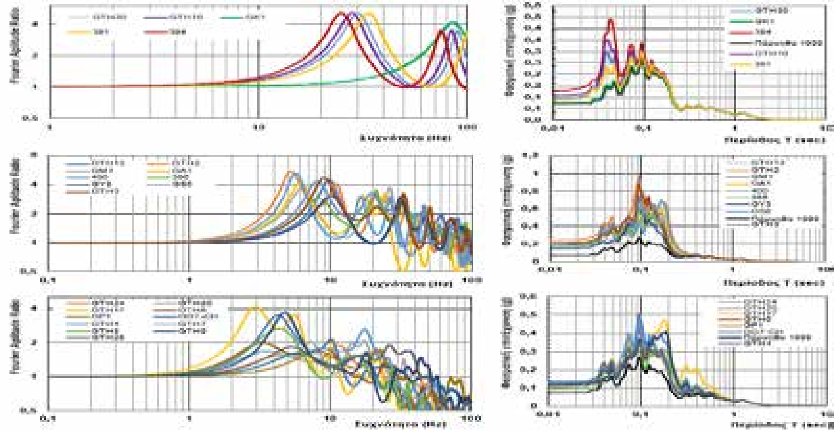

Figure 8: Spatial distribution map of fundamental period T0

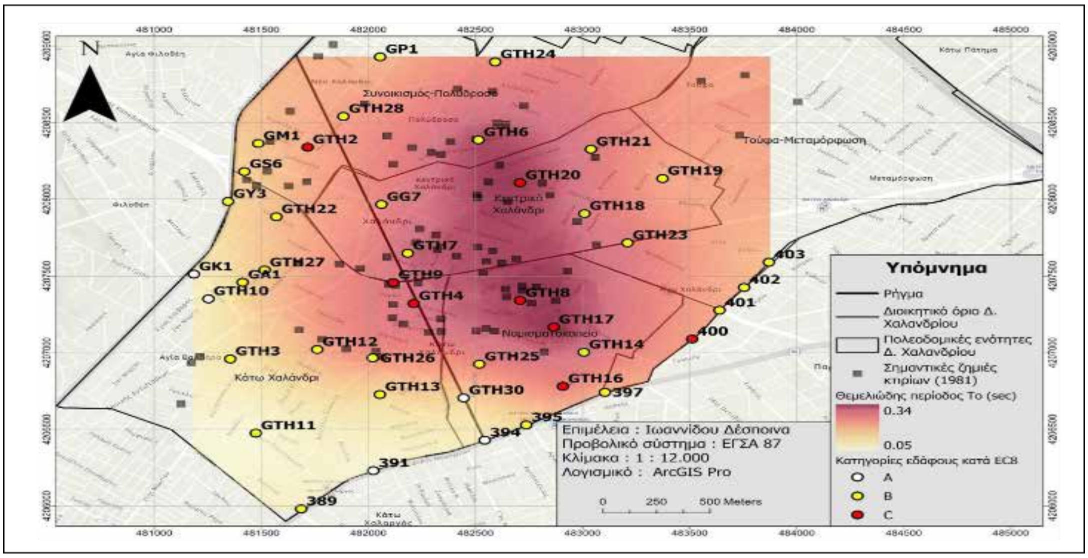

Figure 9: Spatial distribution map of amplification factor A0

Studying the maps of figures 8 and 9, and comparing the most significant building damages caused by the Alkyonides earthquake in 1981, most of the damages are observed in the northeastern and eastern part of Chalandri and mainly in central Chalandri, where the thickness of the soil deposits exceeds 20m. (zones D, E, ST), giving periods from 0.15 to 0.34 sec, values that affect single-storey to four-storey buildings. In the SW part of Chalandri, the damages appear at soil deposit depths of up to 10m. and are clearly less than in the previous case.

Evaluating all the above results and observations and according to the spatial distribution maps that were constructed, we reach the following conclusions:

- In the area of eastern Chalandri (central Chalandri, Synoikismos – Polydroso) the deepest soil deposits prevail without the rocky subsoil being known, resulting in the longest fundamental periods found of the order of 0.12sec – 0.34sec. These conclusions are restricted by the lack of basement rock in the boreholes in zone ST.

- In the area of the Nomismatokopeio, in addition to the deep deposits that prevail, the soils are looser (small number of Nspt blows, category C according to EC8), resulting in large amplification factor of the order of 4 due to the stronger impedance with the considered subsoil.
- Finally, in Kato Chalandri it seems that two areas with different depths of soil deposits prevail. To the west and around the administrative boundaries of the Municipality, shallow soil deposits prevail with cohesive soils with fundamental period of the order of 0.06sec, while further east, the deposits become deeper with looser soils giving amplification factor of the order of 4 and fundamental period of the order of 0.20sec. This is probably why the damage in the Kato Chalandri area is concentrated in its eastern part.

In this study, despite the large amount of geotechnical data collected and analyzed, unfortunately it was not possible to find geophysical data, with the exception of a cross-hole test. Thus, the estimation of Vs was based on empirical formulas in correlation with the Nspt blows and the results of a single cross-hole test. This lack of data constitutes one of the main limitations of the present study, combined with the fact that the depth of most boreholes does not reach 30 meters and often does not reach the bedrock (this latter limitation leads to the lack of content of the seismic analyses at shorter periods that would be associated with the deeper soil layers). On the other hand, the relatively small difference between the Vs of the soil layers leads to relatively low levels of amplification, which for higher impedance values would potentially lead to higher ground motion around the resonance frequencies. In the future, and towards a more theoretical investigation of uncertainties, a new analysis could be carried out including variations in the Vs values, following statistical processing and randomization of the profiles. Furthermore, given that maximum ground accelerations greater than 0.20 g were estimated at the surface of some soil profiles, it would be advisable to carry out a non-linear analysis of the soil formations. This could lead (due to the reduction of the stiffness and the velocity Vs in the shallower layers) to somewhat lower amplifications and natural frequencies.

BIBLIOGRAPHY

Αθανασόπουλος, Γ. (1995). Εμπειρικές συσχετίσεις Vs - Nspt και Go - Nspt από αποτελέσματα δοκιμών σε Ελληνικά εδάφη. Τεχνικά Χρονικά, 7-28.

Λέκκας, Ε., Σούκης, Κ., Λόζιος, Σ., & Αντωνίου, Β. (1999). Χρήση των ΓΠΣ (GIS) στον Αντισεισμικό Σχεδιασμό και την οργάνωση του Δήμου Χαλανδρίου. Πρακτικά 5ου Πανελλήνιου Γεωγραφικού Συνεδρίου. Αθήνα: ΕΓΕ

Χριστούλας, Σ., Τσιαμπάος, Γ., & Σαμπατακάκης, Ν. (1983). Γεωτεχνική Έρευνα: Έδαφος Θεμελιώσεως περιοχής Χαλανδρίου και σεισμοί του 1981. ΚΕΔΕ ΕΚ1α. Αθήνα: Μη δημοσιευμένη έκθεση.

Bard, P. Y., 1999. Local effects on strong ground motion: Physical basis and estimation methods in view of microzoning studies, in Proceedings, Advanced Study Course on Seismotectonic and Microzonation Techniques in Earthquake Engineering 4, Kefallinia, Greece, pp. 127–218

Boore, D. (2004). Estimating Vs(30) (or NEHRP Site Classes) from Shallow Velocity Models (Depths < 30 m). Bulletin of the Seismological Society of America, pp. 591– 597.

Chavez-Garcia, J., Raptakis, G., Makra, A., & Pitilakis, K. (2000). Site Effects at EUROSEIST - II: Results from 2D Numerical Modelling and Comparison with Observations. Soil Dynamics and Earthquake Engineering (1), pp. 23-39.

Chen, S., & Ong, C. (2012). Spectral Analysis of Surface Wave for Empirical Elastic Design of Anchored Foundations. Advances in Civil Engineering. doi:10.1155/2012/635257

Hashash, Y., Musgrove, M., Harmon, J., Ilhan, O., Xing, G., Numanoglu, O., Park, D. (2020). DEEPSOIL 7.0. User Manual. Urbana, Illinois, USA.

Jia, J. (2018). Soil Dynamics and Foundation Modeling (Τόμ. Chapter 2). Springer International Publishing AG.

Kausel, E., & Roesset, J. (1984). Soil amplification: some refinements. International Journal of Soil Dynamics and Earthquake Engineering, pp. 116-123.

Koukis, G., & Sabatakakis, N. (2000). Engineering geological environment of Athens, Greece. Bulletin of Engineering Geology and the Environment, pp. 127-135. doi:10.1007/s100640000058

Mariolakos, I., & Fountoulis, I. (2002). The Athens Earthquake September 7, 1999 Neotectonic Regime and Geodynamic Phenomena. NATO Science Series, pp. 113- 126.

Luzi L., et al. (2020). Engineering Strong Motion Database (ESM) V2.0. INGV. https://doi.org/10.13127/ESM.2

National Observatory of Athens, Institute of Geodynamics, Athens. (1975). https://doi.org/10.7914/SN/HL

Pitilakis, K., Raptakis, G., & Makra, A. (1999a). Site Effects: Recent Consideration and Design Provisions. Proceedings of the 2nd International Conference on Earthquake Geotechnical Engineering. Lisbon.

Raptakis, D., Anastasiadis, A., Pitilakis, K., & Lontzetidis, K. (1994). Shear wave velocities and damping of Greek natural soils. 11th European Conference on Earthquake Engineenng, (pp. 477-482). Vienna.

Raptakis, G., Manakou, M., Chavez-Garcia, J., Makra, A., & Pitilakis, K. (2005). 3D Configuration of Mygdonian Basin and Preliminary Estimate of its Site Responce. Soil Dynamics and Earthquake Engineering (11), pp. 871-887.

Tsiabaos, G., & Sabatakakis, N. (2011). Empirical estimation of shear wave velocity from in situ tests. Bull. Eng. Geol. Environ., pp. 291-297. doi:10.1007/s10064-010-0324- 9

Seismic vulnerability of cultural heritage. The case of the archaeological museum of Rhodes: building performance, safety of the public and exhibits

Irakleidis A.-K.[1] Ktenidou O.-J.[2]

(1) Civil Engineer, graduate of the Inter-Institutional Master Course «Natural Hazards and Disaster Mitigation»

(2) Senior Researcher at National Observatory of Athens, Greece

Introduction / Background

Natural disasters and especially earthquakes in seismically active areas such as Greece, constitute the most significant risk that threatens tangible cultural heritage: buildings and other structures (bridges, aqueducts, etc.), archaeological and historical sites but also artifacts of everyday life, funerary objects, works of art, etc. that are kept in warehouses or exhibited in museums.

The vulnerability of buildings belonging to cultural heritage is high: constructed of load-bearing masonry – a brittle material – they do not possess the structural characteristics that allow them to absorb the energy released by an earthquake, without being subject to damage and ultimately collapse. Respectively, objects placed on pedestals, shelves, in display cases or suspended from ceilings and walls, etc., under a strong earthquake run a high risk of suffering damage that is often irreversible, even when the museums themselves remain intact.

In recent major earthquakes in Greece, as well as in other seismically active countries, monuments and museum exhbits were the ones that were most affected.

The aim of this paper is to demonstrate the relationship between the requirement for the protection of human life, while simultaneously protecting the monumental values carried by buildings and objects that belong to cultural heritage.

A case study of a building located in an area with a rich seismic history was examined, for which it was possible to collect data in order to highlight the objectives of the work. The Archaeological Museum of Rhodes was chosen, that is a building built from the island's Hospitaller Knights of St. John (1310-1522) as their New Hospital. The building was completed in 1489 and is located within the Medieval City of Rhodes, an area where data on the dynamic behavior of its soil formations is available from previous studies, while the bibliography is rich in data for the structural types and the mechanical properties of the materials of the buildings of this World Heritage Site.

The seismic vulnerability of the building was studied with modern computational methods, following the provisions of the Code for interventions in buildings made of load-bearing masonry (KADET), while the stability of exhibits on pedestals was calculated with procedures proposed in the American regulation FEMA P-58 and other sources. The results of the preliminary analyzes are interesting. On the one hand, as expected, the iconic medieval building turns out to fall short of modern requirements for the seismic vulnerability of museum buildings. On the other hand, museum exhibits that are placed on the museum floors with conventional support methods (usually on pedestals that are not anchored to the floor) prove to be particularly vulnerable to earthquakes – indeed considerably smaller than those expected to cause damage to the building itself. The above results are consistent with what has been observed in recent and past earthquakes. For this reason, extensive research on this field is undergoing internationally in order to mitigate seismic risk for monuments and museum exhibits.

Seismic vulnerability of the archaeological museum of Rhodes

From an architectural point of view, the building under study is a Gothic building with Renaissance elements. In plan, it covers an area of approximately 3600 m^2 with a maximum dimension in the N-S direction of 65 m and in the E-W direction of 60 m. It has two floors and its main morphological characteristic is the large atrium in the center that covers an area of approximately 500 m^2, which is surrounded by the rooms. The first floor is dominated by the large "patients' hall", an elongated hall on the facade of the building (eastern side) measuring 54.0 m x 14.0 m, with a central arcade consisting of 7 intermediate octagonal columns. The height of the large hall is greater than the rest of the floor by approximately 3.0 m and dominates the facade of the building.

The buildings' load bearing walls are made of three-leaf masonries. The main building material is the local yellowish sandstone, which is the material of all the buildings of the medieval city and its fortresses. The mechanical characteristics of the walls were assumed to be the same as those used in a recent research work for the nearby Arsenal de Milly (Cattari et al, 2015). The ground floor ceiling is made of masonry vaults, while the first floor is covered with reinforced concrete slabs that are the result of the most recent large scale intervention on the building, dated back in the 1920's when Rhodes came under the Italian colonial rule.

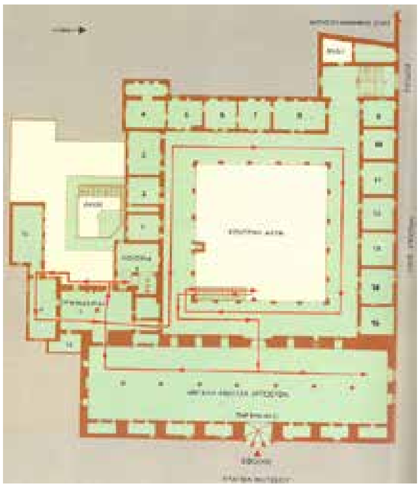

Figure 1: Plan of the 1st floor of the museum (source: I. Kollias, 1991, The Knights of Rhodes)

The underground conditions of the Medieval City of Rhodes were studied in the past by the Aristotle Polytechnic School (1997) and results for the dynamic response at the ground surface were taken into account in the analyses. In the next figure the division of the medieval city of Rhodes in distinct zones is presented.

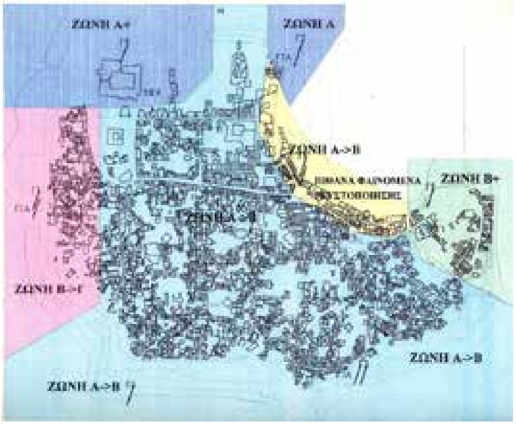

Figure 2: Division of the Medieval City into distinct zones according to their seismic response

The building was simulated with the equivalent frame model method, using the specialized commercial software package 3MURI. This method reduces the plane walls into three types of elements: piers (vertical elements), lintels (horizontal elements) and rigid nodes.

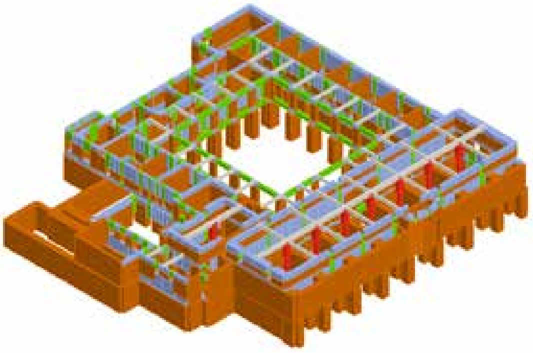

Figure 3: Three-dimensional model of equivalent frames (3MURI software)

Two types of analysis were performed on the geometric model of the building:
a) Modal analysis, which determines the vibration modes of the building and their degree of participation in the overall response of the structure, and

b) equivalent static nonlinear analysis (pushover).

The modal analysis of the model provides all possible eigenmodes of the building's oscillation and contributes to a better understanding of its dynamic behavior in the frequency domain.

From the analysis performed, it was found that the significant eigenmodes that oscillate at least 75% of the seismic mass of the building per direction are more than one and they are ranging between 0,13s and 0,23s – it is a very stiff building indeed. This fact is not surprising. Despite the existence of rigid concrete slabs on the roof of the first floor, diaphragmatic behavior is not ensured. The slabs lack of continuity over the entire surface of the building's floor plan, as they are interrupted by the large atrium in the center the different level of the building's two largest rooms at the first floor.

On the other hand, the pushover analysis helps to identify the weaknesses of the structural system and assess its seismic adequacy for a selected performance level and level of the seismic hazard. A variety of performance levels may be introduced and checked depending on the significance and the level of exposure of the examined building. In the case study, these levels were determined by the current Greek regulation (KADET) for museum buildings, which are significantly higher than those for typical residential buildings.

Despite certain limitations of the application of pushover method to this building, it provides some useful insight to its response. The building shows significant damage for most of the examined scenarios at its upper floor, while the ground floor remains intact. This means that if a desired level of safety, as determined by the current seismic regulations should be reached, measures to strengthen the building's upper floor should be studied and implemented.

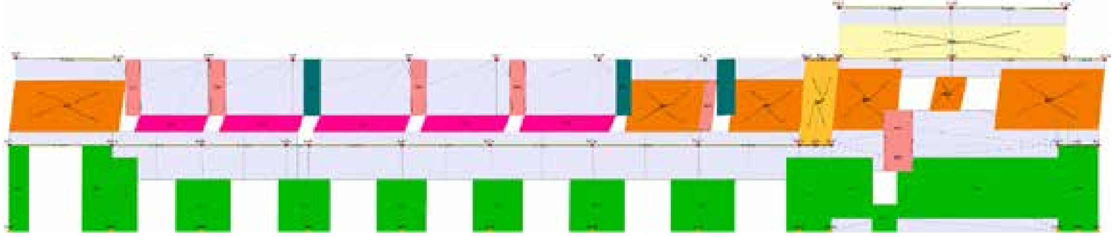

Figure 4: Illustration of the plane model of a characteristic wall of the building at the last step of the pushover analysis (3MURI software). With different colors are shown the different modes and levels of failure of the elements.

Seismic vulnerability of museum artifacts

The stability of museum artifacts depends on many factors, such as the characteristics of the incoming earthquake, the response at each point of the building, the location, the materials involved and the method of support of the exhibits etc. In the present study, a simplified method of analysis of the stability of museum exhibits that are mounted on pedestals that rest freely on the museum floor was used. The procedure is provided in the American code FEMA P-58 and its application field includes the seismic stability of building equipment items, such as libraries, devices freely placed on the floor, etc.

In the method, two limit states are examined: the limit state against overturning and the limit state against sliding, whichever appears first. Its philosophy is based on the assumption that objects are allowed to slide or rock, up to a maximum limit, which is determined by a median maximum floor velocity. This limit is determined in such a way that if the object slides, the distance traveled does not endanger its integrity due to a fall or collision, while if the object rocks, it does not risk overturning after a few rocking cycles. In the present work, although median maximum floor velocity is calculated, a more conservative approach is adopted due to the great importance of the exhibits: it is the onset of rocking or sliding which signals failure. And as the sliding coefficient is a more controllable parameter, the critical acceleration $S_{aO}S_{aO}$ for the onset of rocking was considered as a criterion of failure.

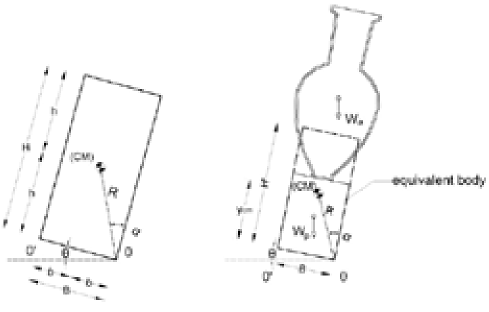

(a) (b)

Figure 5: Geometric definitions of the method by Spyrakos et al (2017)

Using the formulas of the aforementioned method, the stability of a large number of objects from the museum's sculpture exhibition was examined, taking into account in a simplified manner their actual geometric characteristics. From the calculations performed, it was found that failure of exhibits is expected even for small earthquakes. The percentage of failure is increased when artifacts are exhibited on a higher floor, where seismic acceleration is amplified compared to the ground acceleration.

It is indicated that for an earthquake for which the museum building should not develop damage (performance level A2 according to the Greek intervention code), at least 7% of the exhibits are expected to begin to rock. This percentage is increasing significantly if these exhibits are placed on a floor.

It is concluded that even if the results of the simplified calculations presented in this chapter are conservative and based on assumptions that have large margins of error, they confirm what is already known from recent international and local experience: museum artifacts are not earthquake-proof and the main risk they run does not come so much from the failure of the building as from the loss of their stability due to strong ground motion.

From this point of view, such simple calculation methods are extremely useful for quickly assessing the risk of overturning or sliding of exhibits, but they certainly do not replace more detailed and accurate methodologies which, however, require reliable data in order to be useful and practically usable.

Discussion

Seismic safety of museums and artifacts is a subject of great scientific and technological interest, on which research is being developed internationally. The building under study, the archaeological museum of Rhodes has a monumental character and at the same time it hosts an important archaeological exhibition. Thus, both the integrity of the building and the safety of the exhibits are of great importance.

The methodology used and analyses performed under the present work meet certain limitations and further work is needed. More specifically, regarding the study of the building, a more detailed knowledge of its structural system and the materials it consists of is required. More sophisticated analyses would give a better insight to its seismic response at every location, which would be particularly useful for a reliable analysis of the seismic performance of the building and for the stability analysis of the exhibits as well. Furthermore, more complex models for the calculation of the rocking characteristics of artifacts, based on detailed geometric mapping would provide a better understanding of their safety margins under earthquake loading and in the selection and development of new appropriate methods of supporting and displaying museum artifacts.

Acknowledgements

Among the people who helped in one way or another in the preparation of this work, we feel the need to acknowledge the contribution of Dr. Dimitrios Vamvatsikos, associate professor at NTUA, whose initial ideas and directions formed the basis for the present work.

References

Αριστοτέλειο Πανεπιστήμιο Θεσσαλονίκης, Τμήμα Πολιτικών Μηχανικών, Τομέας Γεωτεχνικής Μηχανικής. ΤΔΠΕΑΕ Επιτροπή Παρακολούθησης Μνημείων Μεσαιωνικής Πόλης Ρόδου. Ερευνητικό Πρόγραμμα 9233 – Στερεωτικά Προβλήματα Οχυρώσεων της Μεσαιωνικής Πόλης της Ρόδου, Μάρτιος 2000.

Βαδαλούκας Γ., Βιντζηλαίου Ε., Γκανάς Α., Γιαρλέλης Χ.,Ζιωτοπούλου Κ., Θεοδουλίδης Ν., Καρασαντέ Η.,Μάργαρης Β., Μυλωνάκης Γ., Παπαχρηστίδης Α., Ρεπαπής Κ., Ψαρρόπουλος Π., Σέξτος Α. (2020). Σεισμός Σάμου, 30 Οκτωβρίου 2020-Προκαταρκτική Έκθεση της ΕΤΑΜ, 65 σελ.

Βλάχος Ν., Διαμαντόπουλος Σ., Φραγκιαδάκης Μ. Σεισμική συμπεριφορά έργων τέχνης που εδράζονται σε άκαμπτη λικνιζόμενη βάση. 4ο Πανελλήνιο Συνέδριο Αντισεισμικής Μηχανικής και Τεχνικής Σεισμολογίας., Αθήνα, 5-7 Σεπτεμβρίου 2019

Λέκκας, Ε., Σταυρακάκης Γ., Σακελλαρίου Δ., Λόζιος, Σ. (1995). Εφαρμοσμένο ερευνητικό πρόγραμμα: Αντισεισμικός Σχεδιασμός και Οργάνωση Δήμου Ρόδου. Εθνικό και Καποδιστριακό Πανεπιστήμιο Αθηνών. Σχολή Θετικών Επιστημών – Τμήμα Γεωλογίας. Τομέας Δυναμικής Τεκτονικής και Εφαρμοσμένης Γεωλογίας. Έκδοση: ΤΕΕ – ΤΜΗΜΑ ΔΩΔΕΚΑΝΗΣΟΥ, Δεκέμβριος 1995.

Λέκκας, Ε., Λόζιος, Σ., Σκούρτσος, Ε., Βασιλάκης, Ε., Δανάμος, Γ. (2008). Πιλοτικό Πρόγραμμα Πολιτικής Προστασίας για την αντιμετώπιση των Φυσικών Κινδύνων στη Ν.Α. Δωδεκανήσου. Μέρος Β. Ανάλυση Φυσικών Κινδύνων. Τεύχος Β-10. Νήσος Ρόδος. Εθνικό και Καποδιστριακό Πανεπιστήμιο Αθηνών, Τμήμα Γεωλογίας και Γεωπεριβάλλοντος, 56 σελ.

Λέκκας, Ε., Παπανικολάου, Δ., Σακελλαρίου, Δ. (1998). Νεοτεκτονικός Χάρτης της Ελλάδας, Φύλλο Ρόδος, κλίμακα 1:100.000. Ευρωπαϊκό Κέντρο Πρόληψης και Πρόγνωσης Σεισμών, Οργανισμός Αντισεισμικού Σχεδιασμού και Προστασίας, Επιτροπή Τεκτονικής της Ελληνικής Γεωλογικής Εταιρίας.

Μαυρούλης Σπυρίδων. Σύνταξη οδηγιών για τη διεξαγωγή Άσκησης Εκκένωσης της Μεσαιωνικής Πόλης της Ρόδου. Ο.Α.Σ.Π. Δράση του ΕΚΠΠΣ – Preseismic assessment of the traditional dwellings, vulnerability assessment and evacuation of the old town of Rhodes. Νοέμβριος 2021.

Παπαδόπουλος Α. Γεράσιμος (2014), Ρόδος - Οι Σεισμοί και τα Τσουνάμι από την Αρχαιότητα μέχρι Σήμερα. Εκδόσεις Οσελότος

Σπυράκος Κωνσταντίνος. Κατασκευές από τοιχοποιία. Αποτίμηση και επεμβάσεις για σεισμικά φορτία (2019). Α΄ έκδοση ISBN: 9786180012569 Εκδόσεις ΕΡΓΟΝΟΜΟΣ

Υπουργείο Πολιτισμού, Γενική Διεύθυνση Αρχαιοτήτων, Διεύθυνση Συντήρησης Αρχαιοτήτων. Σεισμοί και Αρχαιότητες. Προληπτικά και Πρώτα Σωστικά Μέτρα. Σ.Γκιώση, Μ.Κρίνη, Θ.Μαραγκού, Π.Πρόκος. Αθήνα, 2002 ISBN: 960-214-686-9

Ψυχάρης Ι., Ταφλαμπάς Ι. Προκαταρκτική εκτίμηση της εδαφικής κίνησης στην πόλη της Κω στο σεισμό της 21.07.2017, Νοέμβριος 2017, https://psycharis.weebly.com/uploads/1/6/2/5/16258088/kos.pdf

Ψυχάρης Ι. και συνεργάτες. Καταρρεύσεις αρχαίων μνημείων και καινοτόμες μέθοδοι βελτίωσης της σεισμικής τους συμπεριφοράς. Η περίπτωση του σεισμού της Κω 2017. https://5psamts.eltam.org/katarrefseis-archaion-mnimeion-kai-kainotomes-methodoi-veltiosis-tis-seismikis-tous-syberiforas-i-periptosi-tou-seismou-tis-ko-2017/

Χρήστου Α. (2020). Προσομοιώσεις της ισχυρής σεισμικής κίνησης στο κοντινό πεδίο του σεισμού της Κω-Αλικαρνασσού 2017. Μεταπτυχιακή διπλωματική εργασία. Τμήμα Γεωλογίας, Τομέας Γεωφυσικής ΑΠΘ. Τριμελής Εξεταστική Επιτροπή: Κυρατζή Α., Θεοδουλίδης Ν., Ρουμελιώτη Ζ.

Ambraseys, N.N., Adams, R.D. The Rhodes earthquake of 26 June 1926. *Journal of Seismology* **2**, 267–292 (1998). https://doi.org/10.1023/A:1009706415417

Baggio S., Berto L., Rocca I., Saetta A. Vulnerability assessment and seismic mitigation intervention for artistic assets: from theory to practice, Engineering Structures, Volume 167, 2018, Pages 272-286, ISSN 0141-0296, https://doi.org/10.1016/j.engstruct.2018.03.093.

Bommer, J. J., & Alarcon, J. E. (2006). THE PREDICTION AND USE OF PEAK GROUND VELOCITY. Journal of Earthquake Engineering, 10(1), 1–31. https://doi.org/10.1080/13632460609350586

Booth, E. (2007). The Estimation of Peak Ground-motion Parameters from Spectral Ordinates. Journal of Earthquake Engineering, 11(1), 13–32. https://doi.org/10.1080/13632460601123156

Cattari, S., Karatzetzou, A., Degli Abbati, S., Pitilakis, D., Negulescu, C., Gkoktsi, K. (2015). Seismic Performance Based Assessment of the Arsenal de Milly of the Medieval City of Rhodes. In: Psycharis, I., Pantazopoulou, S., Papadrakakis, M. (eds) Seismic Assessment, Behavior and Retrofit of Heritage Buildings and Monuments. Computational Methods in Applied Sciences, vol 37. Springer, Cham. https://doi.org/10.1007/978-3-319-16130-3_15

Diamantopoulos, Spyridon & Fragiadakis, Michalis & Sextos, Anastasios. (2019). Dynamic response of museum artefacts standing on a pedestal.

EPPO//LCR-NTUA Chronopoulos M., Psycharis I., Trezos K. (2016): Draft proposal for Aseismic Design of Non-Structural Components.

FEMA P-58-1, December 2018. Seismic Performance Assessment of Buildings. Volume 1 – Methodology Second Edition

Fragiadakis, Michalis & DiSarno, L. & Saetta, A. & Castellano, Maria Gabriella & Irene, Rocca & Diamantopoulos, Spyridon & Crozet, Vincent & Politopoulos, Ioannis & Chaudat, Thierry & Vasic, S. & Bal, İhsan & Smyrou, Eleni & Psycharis, I. & Hutchinson, Tara & Berto, L.. (2020). Experimental seismic assessment and protection of museum artefacts. 3381-3396. 10.47964/1120.9277.20698.

Ishiyama Yuji Motions of rigid bodies and criteria for overturning by earthquake excitations. Earthquake engineering and Structural Dynamics, Vol.10, 635-650 (1982)

Karaferi E., Melissianos V., Vamvatsikos D. (2022) A preliminary urban seismic risk model for the City of Rhodes Greece. 3rd European conference on earthquake engineering & seismology Bucharest, Romania, 2022

Karatzetzou, A., Pitilakis, D., Kržan, M. et al. Soil–foundation–structure interaction and vulnerability assessment of the Neoclassical School in Rhodes, Greece. Bull Earthquake Eng 13, 411–428 (2015). https://doi.org/10.1007/s10518-014-9637-6

Karatzetzou, A., Negulescu, C., Manakou, M. et al. Ambient vibration measurements on monuments in the Medieval City of Rhodes, Greece. Bull Earthquake Eng 13, 331–345 (2015). https://doi.org/10.1007/s10518-014-9649-2

Kassaras, I., Kapetanidis, V., Ganas, A., Tzanis, A., Kosma, C., Karakonstantis, A., Valkaniotis, S.,Chailas, S., Kouskouna, V., Papadimitriou, P. (2020). The New Seismotectonic Atlas of Greece (v1.0) and Its Implementation. Geosciences, 10 (11), 447. https://doi.org/10.3390/geosciences10110447

Koumousis Vlasis (2008) Seismic Isolation System for the Statue of Hermes at the Archaeological Museum of Olympia. Advances in Protection of Museum Collections from Earthquake Damage. Pages 125-134. Publisher J. Paul Getty Museum. Symposium held at the J.Paul Getty Museum at the villa on May 3-4, 2006.

Lagomarsino, S. Seismic assessment of rocking masonry structures. Bull Earthquake Eng 13, 97–128 (2015). https://doi.org/10.1007/s10518-014-9609-x

Lekkas, E., Lozios, S., Sakellariou, D. (1997a). Neotectonic and Engineering Geological Mapping of the area of Rhodos Municipality, Greece, as a tool for Earthquake Planning and Organization. Proceedings of the International Symposium on Enginnering Geology and the Environment, organized by the Greek National Group of IAEG / Athens / Greece, 23-27 June 1997, Enginnering Geology and the Environment, Marinos, P.G., Koukis, G.C., Tsiambaos, G.C., Stournaras, G.C. (eds), p. 1335-1340.

Lekkas, E ., Lozios, S ., Sakellariou, D . (1997b). Rhodes Island. In: The Islands of the Aegean World, Lekkas, E., Kaplanides, A., Lozios, S. and Sakellariou, D. (eds), International Symposium Engineering Geology and the Environment, Post Symposium Tour 3 - “The Islands of the Aegean World”.

Lekkas, E., Papanikolaou, D., Sakellariou, D. (1998b). Neotectonic Map of Greece, Rhodes Sheet, scale 1: 100,000. European

Center for Earthquake Prevention and Forecasting, Organization for Earthquake Planning and Protection, Tectonic Committee of the Hellenic Geological Society.

Lekkas, E., Sakellariou, D., Bertakis, G., Lozios, S. (1998a). Location of geohazards at Rhodes island, SE Greece. Proceedings of the Eighth International Association for Engineering Geology and the Environment, 21-25 September 1998, Vancouver, Canada, Moore, D., Hungr, O. (eds), p. 953-958.

Lekkas, E., Sakellariou, D., Lozios, S. (1998c). A Proposal for Earthquake Emergency Planning of Rhodes Municipality (Greece). WIT Press, vol. 31, 10 p., doi: 10.2495/RISK980161

Papayanni I, Stefanidou M,Konopisi S, Anastasiou E, PachtaV (2004) Stability issues of the fortification of the Medieval City of Rhodes, Technical report (in Greek). Laboratory of BuildingMaterials, Civil Engineering Department, Aristotle University of Thessaloniki

Pitilakis, D., Karatzetzou, A. Dynamic stiffness of monumental flexible masonry foundations. Bull Earthquake Eng 13, 67–82 (2015). https://doi.org/10.1007/s10518-014-9611-3

Pitilakis, K., Riga, E., Apostolaki, S. et al. Seismic hazard zonation map and definition of seismic actions for Greece in the context of the ongoing revision of EC8. Bull Earthquake Eng (2024). https://doi.org/10.1007/s10518-024-01919-8

J. Podany, Advances in the Protection of Museum Collections from Earthquake Damage, Los Angeles, USA, J. Paul Getty Museum, 2008.

Prota A., Zito M., D’Angela D., Toscano G., Ceraldi C., Fiorillo A. & Magliulo G. (2022) Preliminary Results of Shake Table Tests of a Typical Museum Display Case Containing an Art Object. Advances in Civil Engineering https://doi.org/10.1155/2022/3975958

Prota A., Zito M., D’Angela D., Toscano G., Ceraldi C., Fiorillo A. & Magliulo G. (2023). Dynamic Properties and Seismic Response of a Museum Display Case with an Art Object. In: Cimellaro, G.P. (eds) Seismic Isolation, Energy Dissipation and Active Vibration Control of Structures. WCSI 2022. Lecture Notes in Civil Engineering, vol 309. Springer, Cham. https://doi.org/10.1007/978-3-031-21187-4_72

Spyrakos, Constantine & Maniatakis, Charilaos & Taflampas, Ioannis. (2008). Assessment of seismic risk for museum artifacts. The 14th World Conference on Earthquake Engineering October 12-17, 2008, Beijing, China

Spyrakos, Constantine & Maniatakis, Charilaos & Taflampas, Ioannis. (2017). Application of predictive models to assess failure of museum artifacts under seismic loads. Journal of Cultural Heritage. 23. 11-21. 10.1016/j.culher.2016.10.001.

Jie Qin, Botao Ma, Maomao Song, Mansheng Zhang, Zhizhong Guan, Ling Zhang and Jiaqi Ge. Preventive Seismic Protection Technologies to Museum Collections: Quanzhou Museum of China Case Study. Journal of Physics: Conference Series, Volume 1624, Advanced Algorithms, Analysis Model, Optimization Design and Its Application DOI 10.1088/1742-6596/1624/4/042073

Weiguo Yang, Xiaoguang Zou, Meng Wang, Pei Liu, Rapid seismic risk assessment method for museum exhibition halls based on seismic safety of artifacts, Engineering Failure Analysis, Volume 153, 2023, 107552, ISSN 1350-6307, https://doi.org/10.1016/j.engfailanal.2023.107552.

http://odysseus.culture.gr/h/4/gh41.jsp?obj_id=3665

https://oasp.gr/eleghos-mi-domikis-trototitas

https://www.archaiologia.gr/blog/2014/01/29/kefalonia-mouseio/

http://www.gein.noa.gr/Documents/pdf/ekthesi_G_I_26-2-2014_v2.pdf

https://www.gein.noa.gr/Documents/pdf/Kefalonia2014_ekthesi_G_I.pdf

https://kefalonianmantata.gr/διεθνής-ημέρα-μουσείων-μια-απογοητευ/

https://www.itsak.gr/uploads/news/earthquake_reports/EQ_COS_20170721_M6.6.pdf

https://www.eltam.org/images/nltr/newsletters/20201125/etam_report_samos2020earthquake.pdf

https://www.protothema.gr/culture/article/1060445/o-seismos-traumatise-mouseia-kai-arhaiologikous-horous-se-samo-kai-hio/

https://www.rodiaki.gr/article/362325/oi-filoi-poybombardizan-alyphta-th-mesaiwnikh-polh

https://culturalheritagestudies.ceu.edu/concept-and-history-cultural-heritage

17th INTERNATIONAL CONGRESS
of the Geological Society of Greece

BULLETIN OF THE GEOLOGICAL SOCIETY OF GREECE, SP. PUBL.

EXTENDED ABSTRACT 118

Rock slope stability analysis on the road axis of Kleisoura – Kastoria, Greece

Irakliotis A. W.[1] Papathanassiou G.[1]

(1) School of Geology, Aristotle University of Thessaloniki, Greece, airak@geo.auth.gr

Background

Transport corridors, like other infrastructure such as fuel lines, telecommunication, water, sewage and energy corridors, are highly vulnerable to landslide phenomena. Landslides pose a threat to both infrastructure and human lives, with their impacts ranging from minor disruptions to economic catastrophes (Crozier et al., 2005). A variety of transport infrastructure projects require the excavation of rock cuts. The design process of rock cuts is usually concerned with details of the structural geology, meaning the orientation and characteristics of the discontinuities. In cases where the rock strength is much higher than the stresses in the rock, where there is little concern of fracturing, the design of slopes is primarily concerned with the stability of rock blocks formed by the discontinuities (Wyllie et al., 2017). The process of studying the discontinuities that characterize a certain rock mass should always involve a field investigation where geotechnical data is collected. This typically involves the collection of the discontinuities' orientation measurements using a geological compass, their characteristics, such as spacing, length and roughness, using a line measure and a profilometer, the compressive strength of their surfaces using a Schmidt hammer and more. In recent years remote sensing technologies such as the use of Terrestrial Laser Scanners or Airborne Laser Scanners have been extensively used to help assess hazards in rock slopes, particularly in regard to the mapping of discontinuities. A similar approach can be achieved using an Unmanned Aerial Vehicle (UAV) combined with the application of the photogrammetry method (Papathanassiou, 2022). Useful data, such as discontinuity orientation and certain characteristics, can then be extracted and used in rock slope stability analysis, in combination with the field obtained data.

Objectives

The present study focuses on the stability analysis of a rock slope along the Kleisoura – Kastoria road axis. One of its objectives is to highlight the usage of modern remote sensing techniques, particularly the use of Unmanned Aerial Vehicles, in the mapping of rock slopes and the evaluation of their stability. For the purposes of stability analysis both traditional and modern data collection methods have been utilized. The main objective is the assessment of the rock mass behavior, in order to predict future failures and suggest remedial measures to protect the infrastructure.

Methods

The methodology applied in this study can be divided into three parts.

The first part consists of the site reconnaissance where all available data concerning the study area was collected. This includes geographical, geological and hydrogeological data, as well as information concerning the tectonics and seismicity of the study area.

The second part includes the engineering geological field survey, where all necessary measurements, such as discontinuity orientations and characteristics, Schmidt hammer measurements, photographs and samples were collected. This phase also included the acquisition of all the necessary photographs for the creation of a 3D point cloud, using the methodology of UAV-based photogrammetry, described by Vasuki et al. (2014).

The third part of this study involves processing data acquired through field investigation and the analysis of the 3D point cloud. This includes generating stereographic plots to display discontinuity orientations and conducting relevant kinematic analyses. Noise removal from the 3D point cloud was performed to exclude elements not representing the anisotropic rock mass, such as vegetation, fallen rock blocks, and highly weathered material. The edited point cloud was then used for semi-automatic extraction of the main discontinuity set orientations using the open-source Discontinuity Set Extractor (DSE) software (Riquelme et al., 2014). Discontinuity spacing was then calculated through both manual analysis and automatic methods using DSE as a complementary approach (Riquelme et al., 2015). The volume of formed rock blocks was determined using two approaches: analyzing failed rock blocks present in the point cloud and applying Palmstrom's formula (Palmstrom, 2005) in combination with the previously quantified discontinuity spacings. Finally, areas of the slope most prone to rockfalls were identified, and rockfall trajectory simulations were performed. Based on these results, remedial measures were proposed and quantified for the studied slope.

Results

The studied slope consists of crystalline rock, specifically gneiss, belonging to the bedrock of the Pelagonic geotectonic zone. It is characterized by three main discontinuity sets, while a fourth set is only observed locally. The rock exhibits varying degrees of weathering; in some areas, it is slightly weathered, while in others it is completely weathered, with some areas locally forming residual soil. The discontinuities vary in roughness, with JRC values ranging between 7 and 12. Clay infill material was observed in some of the discontinuities, and dripping water was also locally present. The minimum representative friction angle used in the kinematic analyses was calculated to be 43°. According to the kinematic analyses, the most common type of potential failure identified was wedge failure, followed by a small number of flexural toppling and planar failures. The blocks formed in the rock mass are characterized as small to medium in volume. The suggested remedial measure to protect the slope from potential rockfalls is the installation of a draped mesh, as there is insufficient space to construct a ditch capable of catching rockfalls on its own.

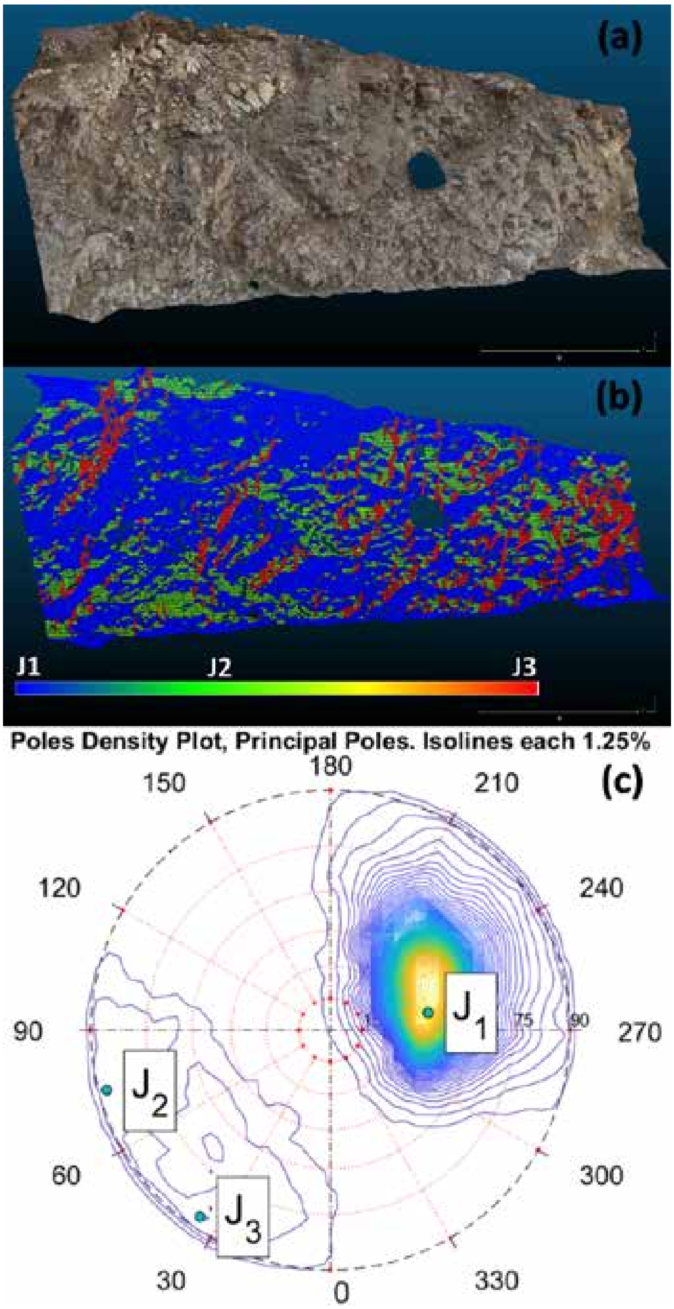

Figure 1. (a) Isometric front view of part of the slope, (b) the visual interpretation of the three main discontinuity sets extracted from the DSE analysis on the 3D point cloud and (c) the stereographic projection of the DSE derived discontinuity sets from the same part of the slope.

Acknowledgements

Part of the transportation costs to the study area were covered by the Research Committee of Aristotle University of Thessaloniki, as part of the corresponding author's master's thesis. Part of the analyses were performed using software provided by RocScience Inc. (Toronto, ON, Canada) under an academic license granted by the Department of Geology, Aristotle University of Thessaloniki.

References

Crozier, M. J., & Glade, T., 2005. Landslide Hazard and Risk: Issues, Concepts and Approach. in: Glade, T., Anderson, M., Crozier, M. J. (Eds.), Landslide Hazard and Risk, 1-40

Palmstrom, A., 2005. Measurements of and correlations between block size and rock quality designation (RQD). Tunnelling and Underground Space Technology, 20(4), 362–377.

Papathanassiou, G., 2022. Engineering Geology and Geohazards, Kallipos Open Academic Editions.

Riquelme, A. J., Abellán, A., Tomás, R., & Jaboyedoff, M., 2014. A new approach for semi-automatic rock mass joints recognition from 3D point clouds. Computers & Geosciences, 68, 38–52.

Riquelme, A. J., Abellán, A., & Tomás, R., 2015. Discontinuity spacing analysis in rock masses using 3D point clouds. Engineering Geology, 195, 185–195.

Vasuki, Y., Holden, E.-J., Kovesi, P., & Micklethwaite, S., 2014. Semi-automatic mapping of geological Structures using UAV-based photogrammetric data: An image analysis approach. Computers & Geosciences, 69, 22–32.

Wyllie, D. C., & Mah, C. (2017). Rock Slope Engineering, 3rd ed. CRC Press.

17th INTERNATIONAL CONGRESS
of the Geological Society of Greece

BULLETIN OF THE GEOLOGICAL SOCIETY OF GREECE, SP. PUBL.

EXTENDED ABSTRACT 119

Relict Taxa and Refugial Dynamics in the Corinth Gulf: Insights from the Pollen Record

Kafetzidou A.[1], Fatourou E.[1], Panagiotopoulos K.[2], Marret F.[3], Koukousioura O.[4,5] and Kouli K.[1]
(1) University of Athens, Greece, akafetzidou@geol.uoa.gr (2) Forschungszentrum Jülich, Germany (3) University of Liverpool, UK (4) University of Cologne, Germany (5) Aristotle University of Thessaloniki, Greece

Introduction / Background

Long pollen sequences covering the Quaternary period have enabled us to gain insight into the long-term variability and migration of the vegetation in the Mediterranean Basin in relation to climatic cycles (e.g., Magri *et al.,* 2017). Climatic fluctuations and ecological competition led to the gradual disappearance of several tree taxa, including Taxodioideae, Sequoioideae, *Sciadopitys, Tsuga, Castanea, Engelhardia*, and *Diospyros* (Suc *et al.,* 1995; Svenning, 2003; Farjon, 2005; Bertini, 2010; Popescu *et al*., 2010). Deteriorated climatic conditions during glacial intervals forced the most demanding taxa into refugial areas, such as the Pindus Mountain Range, or southern regions of Italy and Greece (Suc et *al.,* 1995; Svenning, 2003; Bertini, 2010; Popescu *et al*., 2010). Existing high-resolution pollen records from the southern Balkan show that the amplitude and timing of millennial-scale oscillations in temperate tree abundances depend on the latitude and altitude of the study area as well as its proximity to temperate tree refugia. Long pollen records located in mid-altitudes (between 400 and 850 m above sea level) across the Pindus Mountain Range, such as the Ioannina, Prespa and Ohrid Lakes sites suggest the survival of temperate tree populations during successive glacial-interglacial cycles (Tzedakis *et al.,* 2002, 2004; Panagiotopoulos *et al.,* 2014; Sadori *et al.,* 2016). Opposingly, in the Tenaghi Philippon pollen record from the north-eastern Greece, temperate trees often disappear and only occur during interglacial intervals. The vegetation at Tenaghi Philippon seems to have reacted in a more sensitive way to the climatic cycles, possibly due to the reduction in temperature and moisture (e.g., Tzedakis *et al*., 2006; Pross *et al.,* 2015; Koutsodendris *et al.,* 2023). The Quaternary climate-driven shifts significantly affected ecosystems, particularly at mid-latitudes (Lisiecki and Raymo, 2005; Joannin *et al.,* 2011). In Mediterranean Europe, the shift from the 41,000-year to the 100,000-year climatic oscillations resulted in an increase of in aridity, further impoverishing vegetation communities due to long-term cooling trends (Joannin *et al.,* 2011). This resulted in the gradual extinction of several tree taxa such as *Cedrus, Carya, Pterocarya, Juglans*, and *Zelkova* (Suc *et al.,* 1995; Svenning, 2003; Bertini, 2010). However, the sporadic and scattered nature of records only provides a partial chronostratigraphical overview of their distributions and extinctions, necessitating macroregional-scale adaptations. Despite the existence of some long continuous pollen records from the Balkan Peninsula, most of them are either far from tree refugial areas (e.g. the Tenaghi Philippon record that includes the MPT) or do not include the MPT interval (e.g., Ioannina, Prespa and Kopais). The evolution of north-south and west-east environmental gradients over long time scales, notably the sustained west-east precipitation gradient, has profoundly shaped the plant ecosystems in the southern Balkan Peninsula. This is evidenced by the contrasting vegetational responses observed between Tenaghi Philippon (e.g., Tzedakis *et al.,* 2006; Koutsodendris *et al.,* 2023) in the east and other western Balkan sites such as Lake Ohrid (Sadori et al., 2016; Donders *et al.,* 2021), Ioannina (e.g., Tzedakis *et al.,* 2002, 2003, 2004) and Prespa (Panagiotopoulos *et al.,* 2013, 2014). These findings highlight the need for further analysis of long-term pollen archives from the Balkan Peninsula to better understand the evolution of regional flora and the timing of relict species extinctions in the eastern Mediterranean.

The Gulf of Corinth pollen record provides significant insights into the persistence of relict taxa such as *Liquidambar*, *Carya*, *Pterocarya*, and *Cedrus* throughout the Pleistocene. These taxa, key components of temperate and riparian forests, persisted through multiple glacial-interglacial cycles, indicating the Gulf of Corinth region as a refugium in southeastern Europe. The region's unique climatic, topographic, and hydrological conditions enabled the survival of these taxa despite broader climatic fluctuations. *Liquidambar* displayed remarkable resilience, with a near-continuous presence from MIS 8 (300 ka) to ~13 ka BP, thriving during glacial phases in humid conditions. *Carya* persisted from MIS 24 (~923 ka) to MIS 8, with low percentages correlating with localized humid microclimates influenced by marine humidity. *Pterocarya* was present from MIS 13 (~500 ka) to MIS 3 (~36 ka), reaching higher abundances during glacial periods, indicating stable hydrological conditions in wet environments such as floodplains. Similarly, *Cedrus*, which gradually disappeared from the central and northern Balkans by the end of the Pleistocene, remained present in Gulf of Corinth sediments, suggesting local persistence rather than long-distance transport. These findings underscore the Gulf of Corinth's biogeographical significance as a biodiversity hotspot, providing exceptional conditions that allowed the persistence of relict taxa during the glacial maxima and interglacial periods of Quaternary.

The study highlights the region's role as a corridor for species persistence and migration in the Mediterranean. Understanding the resilience of these taxa offers valuable insights into reconstructing past vegetation dynamics, identifying refugia, and predicting ecosystem responses to future climate change. The preservation and further study of this paleoenvironmental archive are important for advancing our knowledge of plant resilience, refugial dynamics, and climatic stability in the Mediterranean region.

Acknowledgements

The study material was retrieved during the IODP Exp. 381. The research work was supported by the Hellenic Foundation of Research and Innovation (H.F.R.I) under the “First Call for H.F.R.I. Research Projects to support Faculty members and Researchers and the procurement of high-cost research equipment grant” (Project Number: 1026, Quaternary Environmental Changes in the Corinth Rift Area: the IODP 381 palynological record: QECCoRA).

References

Bertini, A., 2010. Pliocene to Pleistocene palynoflora and vegetation in Italy: State of the art. Quaternary International 225, 5-24.

Combourieu-Nebout, N., Bertini, A., Russo-Ermolli, E., Peyron, O., Klotz, S., Montade, V., Fauquette, S., Allen, J., Fusco, F., Goring, S., Huntley, B., Joannin, S., Lebreton, V., Magri, D., Martinetto, E., Orain, R., Sadori, L., 2015. Climate changes in the central Mediterranean and Italian vegetation dynamics since the Pliocene. Review of Palaeobotany and Palynology 218, 127-147.

Donders, T., Panagiotopoulos, K., Koutsodendris, A., Bertini, A., Mercuri, A. M., Masi, A., Combourieu-Nebout, N., Joannin, S., Kouli, K., Kousis, I., Peyron, O., Torri, P., Florenzano, A., Francke, A., Wagner, B., Sadori, L., 2021. 1.36 million years of Mediterranean forest refugium dynamics in response to glacial–interglacial cycle strength. Proceedings of the National Academy of Sciences 118.

Farjon, A., 2005. A Monograph of Cupressaceae and Sciadopitys. Royal Botanic Garden, Kew.

Joannin, S., Bassinot, F., Nebout, N.C., Peyron, O., Beaudouin, C., 2011. Vegetation response to obliquity and precession forcing during the Mid-Pleistocene Transition in Western Mediterranean region (ODP site 976). Quaternary Science Reviews 30, 280e297

Koutsodendris, A., Dakos, V., Fletcher, W. J., Knipping, M., Kotthoff, U., Milner, A. M., Müller, U.C., Kaboth-Bahr, S., Kern, O.A., Kolb, L., Vakhrameeva, P., Wulf, S., Christanis, K., Schmiedl, G., Pross, J., 2023. Atmospheric CO2 forcing on Mediterranean biomes during the past 500 kyrs. Nature Communications 14, 1664.

Lisiecki L.E., Raymo M.E., 2005. A Pliocene-Pleistocene stack of 57 globally distributed benthic δ18O records. Paleoceanography 20.

Magri, D., Di Rita, F., Aranbarri, J., Fletcher, W., González-Sampériz, P., 2017. Quaternary disappearance of tree taxa from Southern Europe: Timing and trends. Quaternary Science Reviews 163, 23-55.

Magri, D., Palombo, M.R., 2013. Early to Middle Pleistocene dynamics of plant and mammal communities in SouthWest Europe. Quaternary International 288, 63-72.

Panagiotopoulos, K., Aufgebauer, A., Schäbitz, F., Wagner, B., 2013. Vegetation and climate history of the Lake Prespa region since the Lateglacial. Quaternary International 293, 157-169.

Panagiotopoulos, K., Böhm, A., Leng, M. J., Wagner, B., Schäbitz, F., 2014. Climate variability over the last 92 ka in SW Balkans from analysis of sediments from Lake Prespa. Climate of the Past 10, 643-660.

Popescu, S.-M., Biltekin, D., Winter, H., Suc, J.-P., Melinte-Dobrinescu, M.C., Klotz, S., Rabineau, M., Combourieu-Nebout, N., Clauzon, G., Deaconu, F., 2010. Pliocene and Lower Pleistocene vegetation and climate changes at the European scale: long pollen records and climatostratigraphy. Quaternary International 219, 152-167.

Postigo-Mijarra, J.M., Morla, C., Barrón, E., Morales-Molino, C., García, S., 2010. Patterns of extinction and persistence of Arctotertiary flora in Iberia during the Quaternary. Review of Palaeobotany and Palynology 162, 416-426.

Sadori, L., Koutsodendris, A., Panagiotopoulos, K., Masi, A., Bertini, A., Combourieu-Nebout, N., Francke, A., Kouli, K., Joannin, S., Mercuri, A-M., Peyron, O., Torri, P., Wagner, B., Zanchetta, G., Sinopoli, G., Donders, T.H., 2016. Pollen-based paleoenvironmental and paleoclimatic change at Lake Ohrid (south-eastern Europe) during the past 500 ka. Biogeosciences 13, 1423-1437.

Suc, J.P., Bertini, A., Combourieu-Nebout, N., Diniz, F., Leroy, S., Russo-Ermolli, E., Zheng, Z., Bessais, E., Ferrier, J., 1995. Structure of West Mediterranean vegetation and climate since 5.3 ma. Acta Zoologica Cracoviensia 38, 3-16.

Svenning, J., 2003. Deterministic Plio‐Pleistocene extinctions in the European cool‐temperate tree flora. Ecology Letters 6, 646-653.

Tzedakis, P.C., Frogley, M.R., Heaton, T.H.E., 2003. Last interglacial conditions in southern Europe: evidence from Ioannina, northwest Greece. Global and Planetary Change 36, 157-170.

Tzedakis, P.C., Frogley, M.R., Lawson, I.T., Preece, R.C., Cacho, I., de Abreu, L., 2004. Ecological Thresholds and Patterns of MillennialScale Climate Variability: The Response of Vegetation in Greece during the Last Glacial Period. Geology 32, 109-112.

Tzedakis, P. C., Hooghiemstra, H., Pälike, H., 2006. The last 1.35 million years at Tenaghi Philippon: revised chronostratigraphy and long-term vegetation trends. Quaternary Science Reviews 25, 3416-3430.

Tzedakis, P. C., Lawson, I. T., Frogley, M. R., Hewitt, G. M., Preece, R. C., 2002. Buffered tree population changes in a Quaternary refugium: evolutionary implications. Science 297, 2044-2047.

17th INTERNATIONAL CONGRESS
of the Geological Society of Greece

BULLETIN OF THE GEOLOGICAL SOCIETY OF GREECE, SP. PUBL.

EXTENDED ABSTRACT 120

Rare Insights in the Oligocene flora of Thrace (Greece): Preliminary results from the Rhodopi Petrified Forest

Kafetzidou A.[1], Koukousioura O.[2], Zotiadis V.[3], Kouli K.[1]
(1) National and Kapodistrian University of Athens, akafetzidou@geol.uoa.gr (2) Aristotle University of Thessaloniki, Greece (3) Edafomichaniki S.A., Athens, Greece

New fossil discoveries in the area of Thrace offer remarkable insights into the Oligocene vegetation and paleoenvironmental conditions of southeastern Europe. The plant fossil sites, representing some of the oldest Petrified Forests in Greece, preserve a diverse assemblage of both permineralized wood remains as well as leaf imprints of angiosperm trees. The fossil-bearing deposits comprise of successive pyroclastic series mainly consisting of tuffs intercalated with layers of sandstones, clays and marls. The pyroclastic sequence is linked to the volcanic activity in the Rhodope region during the Late Eocene to Oligocene (Georgiev and Marchev, 2005; Voudouris *et al.*, 2007).

Numerous permineralized well preserved wood specimens were identified, exhibiting the dominance of Fagaceae, mainly *Quercoxylon* sp., and the presence of thermophilic Lauraceae. The occurrence of several leaf litter horizons is recorded within the marl layers of the sequence. Among leaf imprints, the key taxa identified include Fagaceae (*Eotrigonobalanus* sp., *Quercus* spp.), *Myrica* spp., *Ziziphus* sp., *Laurophyllum* spp, *Dicotylophyllum* sp. and representatives of the Leguminosae (Figure 1).

Figure 1. a, b) Logging of the petrified trunks; c) branched petrified trunk; d) leaf imprints (scale: 10 cm).

Our findings show great similarities to those from the neighboring Bulgarian fossiliferous sites, as well as the petrified forest of Evros (Iamandei *et al.,* 2014, 2016, 2024; Velitzelos *et al*., 2014; Velitzelos *et al*., 1999, 2002). In the Bulgarian sites, petrified trunks within tuffs had provided a radiometric age (^{40}Ar/^{39}Ar) of approximately 31 million years (e.g., Iamandei *et al*., 2014, 2016), confirming the Early Oligocene age of the fossils (Georgiev and Marchev, 2005). The volcanic activity, attributed to centers in Kotyli and Kalotycho (Caracciolo *et al.*, 2011), played a key role in the rapid burial and exceptional preservation of plant material. The studied fossil-bearing area in combination with the petrified forest of Evros (Velitzelos *et al.,* 2014; Velitzelos *et al.,* 1999, 2002) represent some of the oldest occurrences of paleovegetation in Greece.

References

Caracciolo, L., Critelli, S., Innocenti, F., Kolios, N., Manetti P., 2011. Unravelling the provenance from Eocene-Oligocene sandstones of the Thrace Basin, North-East Greece. Sedimentology 58, 1988-2011.

Georgiev, S., Marchev, P., 2005. Oligocene pyroclastic rocks and a petrified forest in the Nanovitsa depression. Bulgarian Academy of Sciences, Geochemistry, Mineralogy and Petrology 42, 47-65.

Iamandei S., Iamandei, E., Bozukov, V., Tsenov, B., 2014. Oligocene fossil woods from Rhodopes, Bulgaria. Acta Palaeontologica Romaniae 9, 15-25.

Iamandei S., Iamandei, E., Bozukov, V., Tsenov, B., 2016. New Oligocene fossil woods from Rhodopes, Bulgaria. Acta Palaeontologica Romaniae 12, 47-65.

Iamandei S., Iamandei E., Velitzelos D., Velitzelos E., 2024. Palaeoxylotomical studies in the Cenozoic petrified forests of Greece. Part three – dicots. Acta Palaeontologica Romaniae 20, 61-96

Velitzelos D., Bouchal J.M., Denk T., 2014. Review of the Cenozoic floras and vegetation of Greece. Review of Palaeobotany and Palynology 204, 56-117

Velitzelos, E., Kvaček, Z., Velitzelos, D., 2002. New Oligocene leaf floras from the volcanic complex of the Evros Mountains. 6th European Paleobotany-Palynology Conference Athens, Greece 2002, Book of Abstracts, 185-186.

Velitzelos, E., Kvaček, Z., Walther, H., 1999. Erster Nachweis von *Eotrigonobalanus furcinervis* (Rossm.) Walther & Kvaček (Fagaceae) in Griechenland. Feddes Repertorium 110, 349-358.

Voudouris, P., Velitzelos, D., Velitzelos, E., Thewald, U., 2007. Petrified wood occurrences in western Thrace and Limnos Island: Mineralogy, geochemistry and depositional environment. Proceedings of the 11th International Congress, Bulletin of the Geological Society of Greece XXXX/1, 238-250.

17th INTERNATIONAL CONGRESS of the Geological Society of Greece

BULLETIN OF THE GEOLOGICAL SOCIETY OF GREECE, SP. PUBL.

EXTENDED ABSTRACT 121

Mapping the Geological Landscape of NW Bay of Navarino Through Time

Kaimakami M.[1]

(1) *University of Peloponnese, Kalamata, Greece, mariakaim04@gmail.com*

Abstract

This study explores the geological landscape of the northwest bay of Navarino and its influence on human settlement patterns. Using field surveys, GIS mapping, and optical microscopy, the research identifies key geological formations and their relationship with archaeological remains. The findings suggest that elevated limestone areas, such as the hills of Prophitis Ilias and Koukouras, were preferred for habitation, while fewer artifacts were found in the surrounding lagoon and cultivated areas. The study highlights the need for further research to confirm these observations and deepen our understanding of the region's historical development.

Introduction

The northwest bay of Navarino, located between modern Pylos and Romanos, is a significant cultural and environmental area, forming part of the Natura 2000 network. This study focuses on the region's geological and archaeological features, including the Gialova lagoon, Voidokoilia beach, Coryphasium peninsula, and surrounding hills and fields. Major archaeological discoveries include the Mycenaean tholos tomb of Thrasymedes, the Frankish Palaiokastro, and Nestor's Cave with Neolithic occupation traces. Since 2021, the Pylos Geoarchaeological Program (GEAPP) has been conducting research to investigate the area's natural and cultural environment. This study aims to analyze the geological landscape in relation to archaeological findings.

Geomorphology

The study area is part of the Gavrovo-Tripoli geotectonic zone, characterized by carbonate sedimentation from the Upper Triassic to the Upper Eocene. The western region, particularly the Coryphasium peninsula and nearby hills, consists mainly of Paleocene to Eocene limestone, while the Gialova lagoon lies on Holocene alluvial and fluvial deposits. Coastal sand dunes of Holocene-age, reaching up to 10 meters in height, dominate the shoreline. Tectonic movements and erosional processes have shaped the area, with evidence of past marine submersion and gradual land emergence over the past 9,000 years.

Historical Background

The Bay of Navarino has a long history of human presence, with research beginning with the University of Minnesota Messenia Expedition (UMME, 1953-1975) and continuing with the Pylos Regional Archaeological Project (PRAP, 1991-1999). Evidence of habitation dates back to the Paleolithic period, including tools and settlement in Nestor's Cave. During the Bronze Age, important settlements and burial monuments, such as the tholos tomb of Thrasymedes, indicate significant activity. In the Classical period, the region witnessed military conflicts, including the Battle of Sphacteria (425 BC). During the Roman and Byzantine eras, it remained an important center, while in the Frankish and Ottoman periods, fortifications were strengthened. The Battle of Navarino (1827) marked a turning point in Greece's independence.

Methodology

A field survey was conducted to record geological and archaeological features. Samples were collected for analysis using optical microscopy, and the data was digitized in ArcGIS 10.4.1. The mapping process included thematic layers for geological formations and archaeological discoveries. The coordinate system used was the Greek Grid Reference System (EGSA '87), and aerial photographs from 1945 were incorporated to enhance accuracy.

Key Sites of Geological and Archaeological Interest

- Voidokoilia Beach: Known for its circular shape, the beach comprises limestone, travertine, and dunes. Archaeological findings include ceramics and limestone walls, suggesting a Mycenaean harbor.
- Gialova Lagoon: A vital wetland with Holocene alluvial deposits with rich biodiversity. Drainage works in the 1960s uncovered a Classical and Roman cemetery.
- Divari Beach &Coryphasium Peninsula: The beach consists of alluvium and dunes, while the limestone-rich peninsula hosts ceramics, bones, and architectural remains.
- Prophitis Ilias Hill: Features prehistoric cemetery remains, limestone blocks with pillar holes, and ceramic depos-

its.

- Koukouras Hill: A primarily limestone hill with architectural structures and large limestone blocks indicating past settlements.
- Almyrolakka, Agios Nikolaos, and Kolopanas Beaches: Characterized by sandstone and brecciated limestone, with prehistoric ceramics and wall remnants.
- Agricultural Fields: Consisting of fertile alluvial soils, these areas exhibit limited archaeological finds due to extensive plowing.
-

Mapping and Rock Identification

The study area consists mainly of limestone, sandstone, breccia and flint. The Coryphasium Peninsula, as well as the hills of Prophitis Ilias and Koukouras, are primarily composed of limestone, while sandstones andfossilized aeolian sand appear on beaches such as Almyrolakka, Agios Nikolaos, and Kolopanas. Breccia was identified on the Coryphasium Peninsula, and flint was also present in various locations. A field survey was conducted to collect rock samples, some of which were analyzed using an optical microscope for better identification. The geological mapping revealed a more diverse rock distribution than previously indicated, enhancing our understanding of the region's geological composition.

Archaeological Findings and Settlement Patterns

Archaeological findings in the study area are mainly concentrated on the Coryphasium Peninsula and the hills of Prophitis Ilias and Koukouras, where limestone dominates. Few remains were found around the Gialova Lagoon, likely due to agricultural activities that have disturbed the soil over time. The region has been continuously inhabited since prehistoric times, with settlements, tombs, and artifacts indicating human presence. Changes in vegetation and land use over millennia have influenced the preservation and visibility of archaeological sites. Drainage works in the 20th century also exposed significant findings, highlighting the need for further research to understand human activity in relation to the landscape.

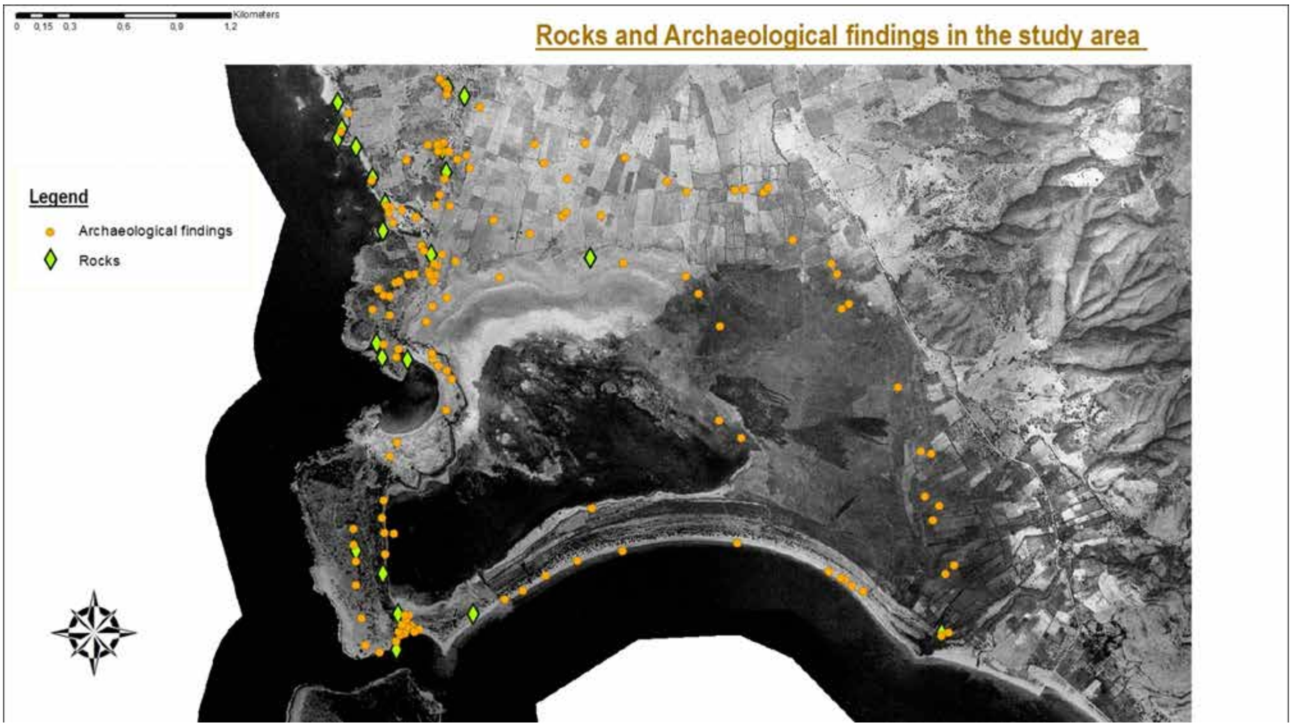

Figure 1. The map of the rocks and the archaeological findings in the study area © Maria Kaimakami.

Discussion

Most archaeological remains are located in elevated limestone areas, suggesting that strategic positioning and material availability influenced settlement choices. The scarcity of finds in the lagoon and cultivated areas may result from erosion, land disturbance, and accessibility issues. Geological mapping identified a wider variety of rock formations than previously recorded, indicating the need for further research. A deeper understanding of archaeological distribution requires investigating environmental, geological, and socio-political factors that shaped human habitation in the area over time.

Conclusions

This research provides an initial understanding of the interaction between geology and human settlement in the northwest bay of Navarino. The concentration of archaeological remains in elevated limestone areas supports the hypothesis that geology influenced habitation choices. However, further research is needed to confirm these patterns, particularly in areas affected by erosion and modern land use. Increased survey efforts are essential to preserve and document archaeological evidence before it is lost. Understanding the geological factors that influenced human settlement in this region can contribute to broader studies of environmental and cultural history in coastal Mediterranean landscapes.

Acknowledgements

ReI thank Dr. G. Malaperdas, Environmentalist Cartographer – Land Surveyor – GIS & R.S. Analyst – Geoinformatics and Earth Studies, for his invaluable assistance with GIS mapping. I also thank E. Zymi, Associate Professor of Classical Archaeology at the Department of History, Archaeology and Cultural Resources Management at the University of Peloponnese, for her invaluable support with the archaeological part of my research and Dr. K. Theodorakopoulou, specializing in geoarchaeology and the use of archaeometric techniques, for her crucial help with the geological part. The first to assist me, N. Zacharias, Professor of Archaeometry, Environmental and Cultural Technology, sadly passed away before the completion of my research.He will be remembered as a distinguished scientist and professor. I am honored to conduct and present this research, as he greatly supported me throughout this endeavor.

References

Agapiou, A., Lysandrou, V., Alexakis, D.D., Themistocleous, K., Cuca, B., Argyriou, A., Sarris, A. and Hadjimitsis, D.G., 2015. Cultural heritage management and monitoring using remote sensing data and GIS: The case study of Paphos area, Cyprus. Computers, Environment and Urban Systems 54, 230–239.

Alcock, S.E, Berlin, A.M., Harrison, A.B., Heath, S., Spencer, J. and Stone, D.L., 2005. The Pylos Regional Archaeological Project, Part VII: Historic Messenia, Geometric through Late Roman. Hesperia 74 (2), 147-209.

Athanassas, C. and Fountoulis, I., 2013. Quaternary Neotectonic Configuration of the Southwestern Peloponnese, Greece, Based on Luminescence Ages of Marine Terraces, Journal of Earth Science 24 (3), 410–427.

Avramidis, P., Iliopoulos, G., Kontopoulos, N., Panagiotaras, D., Barouchas, P., Nikolaou, K. and Papadopoulou, P., 2015. Deposotional environments, sediment characteristics, palaeoecological analysis and environmental assessment of an internationally protected shallow Mediterranean lagoon, Gialova lagoon – Navarino Bay, Greece. Earth and Environmental Science Transactions of the Royal Society of Endinburgh 105, 189-206.

Darvill, T., 2008. The Concise Oxford Dictionary of Archaeology. Second Edition. Oxford University Press, Oxford.

Doula, M.K. and Sarris, A., 2016. Soil environment. Environment and development. Elsevier.

Emmanouilidis, A., 2017. Mid to Holocene Paleoenvironmental study of Gialova lagoon, SW Peloponnese, Greece. Patra.

Hardar, S.K. and Tisljar J., 2014. Introduction to minerology and petrology. Elsevier.

Katsianis, M., Kalayci, T. and Sarris, A., 2022. Bridging Digital Approaches and Legacy in Archaeology. Digital 2 (4), 538-545.

Kennedy, W., 2021. Terra Petraea. The Archaeological Landscape of the Petraean Hinterland from the Hellenistic to the Byzantine Period. Logos Verlag, Berlin.

Kipfer, B.A., 2021. Encyclopedic Dictionary of Archaeology. Second Edition. Springer Nature, Switzerland.

Konstantopoulos, P., 2009. Περιβάλλοντα ιζηματογένεσης και στρωματογραφική διάρθρωση του φλύσχη της Πελοποννήσου - πιθανή γένεση υδρογονανθράκων. Patra.

Kraft, J.C., Rapp Jr., G.R., Aschenbrenner, S.E., 1980. Late Holocene palaeogeomorphic reconstructions in the area of the Bay of Navarino: Sandy Pylos. Journal of Archaeological Science 7, 187-210.

Loy, M., Stocker, S.R. and Davis, J.L., 2021. From Archive to GIS: Recovering Spatial Information for Tholos IV at the Palace of Nestor from the Notebooks of Lord William Taylour. InternetArchaeol 56 (5).

Μαλαπέρδας, Γ., 2023. Χαρτογραφία, Γεωγραφικά Συστήματα Πληροφοριών και Τηλεπισκόπιση, in: Zacharias, N. (Eds), Πολιτιστική Κληρονομιά και Νέες Τεχνολογίες, Papaizisi, Athens, 11-110.

Malaperdas, G. and Zacharias, N., 2018. A Geospatial Analysis of Mycenaean Habitation Sites Using a Geocumulative versus Habitation Approach. Journal of Geoscience and Environment Protection 6, 111-131.

Malaperdas, G., & Panagopoulos, N., 2021. Mapping shoreline changes over the years: The case study of Navarino bay, Pylos, Messenia, Greece. World Journal of Geomatics and Geosciences 1 (1).

Malaperdas, G. &Barberopoulou, A., 2023. Mapping art: 3D geovisualization and virtual worlds in cultural heritage. International Journal of Visual and Performing Arts 5(2).

Malaperdas, G., Grethe, R. and Zacharias, N., 2023. Depicting the past: The significance of old maps and topographic diagrams in Cultural Heritage via GIS in Cultural Heritage. Journal of Archaeological Science: Reports 52 (104276).

Malaperdas, G., Maggidis, C., Karantzali, E., and Zacharias, N., 2023. Field Surveying, Geostatistical and GIS Methods in Archaeology. The Mycenaean Spercheios-Valley Project (MY. SPE. AR. Project 2018-2022). Journal of Archaeology and Anthropology.

Miller, B.A. and Juilleret, J., 2020. The colluvium and alluvium problem: Historical review and current state of definitions. Earth-Science Reviews 209 (103316).

Raith, M.M., Raase, P. and Reinhardt, J., 2011. Guide to Thin Section Microscopy. Second Edition.

Sarris, A., Chliaoutakis, A., Déderix, S. and Donati, J.C., 2013. Reconstructing archaeo-landscapes: myth versus reality as Exploration / Production Analogues. The 6th Symposium of the Hellenic Society for Archaeometry: Craft-based Cultural Influences in the Mediterranean, Athens.

Secchi, M., Zanatta, M., Borovin, E., Bortolotti, M., Kumar, A., Giarola, M., Sanson, A., Orberger, B., Daldosso, N., Gialanella, S., Mariotto, G., Montagna, M. and Lutterotti, L., 2018. Mineralogical investigations using XRD, XRF, and Raman spectroscopy in a combined approach. Journal Raman Spectroscopy, 1–8.

Simpson, R.H., 2014. Mycenaean Messenia and the Kingdom of Pylos. Academic Press Philadelphia, Pennsylvania.

Stamatopoulou, E., Sotiropoulou, M., Karoglou, M. and Bakolas, A., 2021. Characterization of contemporary artworks made on photosensitized canvas by means of optical microscopy and micro-Raman spectroscopy techniques. Microchemical Journal 165 (106110).

Theodorakopoulou, K., 2020. Ανθρωποϊστορίαγραμμένηστηνπέτρα: εποχή του Λίθου και γεωπεριβάλλον. Kardamitsa.

Tsiafakis, D., Evagelidis, V., 2006. GIS as an Interpretative Tool in Greek Archaeological Research. Nottingham.

Valsamaki, I.A., 2012. Πύλος. Μελέτη Διαχείρισης και Ανάπτυξης του Πολιτισμικού τοπίου του όρμου του Ναυαρίνου. Athens.

Willershäuser, T., Vött, A., Hadler, H., Ntageretzis, K., Emde, K., and Brückner, H., 2015. Holocene palaeotsunami imprints in the stratigraphical record and the coastal geomorphology of the Gialova Lagoon near Pylos (southwestern Peloponnese, Greece). Zeitschrift Für Geomorphologie, Supplementary Issues 59(4), 215–252.

Zacharias, N. and Palamara, E., 2016. Glass Corrosion: Issues and Approaches for Archaeological Science, in: Gan, F., Li, Q., Henderson, J. (Eds), Recent Advances in the Scientific Research on Ancient Glass and Glaze, World Century Publishing Corp. and World Scientific Publishing Co., 233-247.

Zacharias, N., Militsi, E., Kylafi, M., Valantou, V., Kazolias, A., Kompoti, A. and Panagiotidis V.V., 2023. Sand & stones: The Pylos Geoarchaeological Program. Journal of Archaeological Science: Reports 51 (104210).

Zangger, E., Timpson, M.E., Yazvenko, S.B., Kuhnke, F., and Knauss., J., 1997. The Pylos Regional Archaeological Project, Part II: Landscape Evolution and Site Preservation. Hesperia 68 (4), 548-641.

17th INTERNATIONAL CONGRESS
of the Geological Society of Greece

BULLETIN OF THE GEOLOGICAL
SOCIETY OF GREECE, SP. PUBL.

EXTENDED ABSTRACT 122

The influence of DSMs spatial resolution on rockfall simulation.

Kakavas M.[1], Kyriou A.[1], Nikolakopoulos K.[1], Koukouvelas I. [1]
(1) University of Patras, Department of Geology, Patra, Greece, kakava.maria@upatras.gr

Abstract

Rockfalls are dynamic geological events characterized by the sudden detachment and descent of rock fragments from steep slopes. These events vary greatly in scale, velocity, and trajectory, influenced by factors such as slope geology, topography, and environmental conditions. This study examines rockfall hazards in Platiana, Greece, using simulation tools— RocFall 4.0, QProto, and HY-STONE. By applying Digital Surface Models (DSMs) with spatial resolutions ranging from centimeters to meters, the study demonstrates that higher-resolution DSMs more accurately simulate rockfall trajectories, velocities, and energy distributions. Coarse-resolution DSMs, however, tend to overestimate rockfall runout and simplify topography. The findings highlight the importance of selecting high-resolution DSMs for reliable hazard assessments.

Introduction

Rockfalls are natural phenomena where rock fragments abruptly detach and freefall from steep slopes, posing significant natural hazards in mountainous and hilly areas (Dorren, 2003; Wu et al., 2025). These phenomena exhibit considerable scale variability, velocity, and trajectory, influenced by factors such as the slope's geological composition, topography, and other environmental conditions (Hungr et al., 1999; Guzzetti et al., 2002; Borella et al., 2019). The unpredictable nature of rockfalls makes their risk assessment and mitigation a challenging task, especially in regions with steep and unstable terrains (Fell et al., 2008). To predict and manage rockfall hazards effectively, researchers employ advanced modelling techniques that integrate terrain analysis and remote sensing data, helping to estimate potential impact zones and identify areas at risk of rockfall events (Jaboyedoff et al., 2005). Digital Elevation Models (DEMs) are essential tools in rockfall hazard assessment, as they provide topographical data critical for simulating rockfall behaviour. DEMs allow the extraction of slope parameters that influence rockfall dynamics, including slope angle, roughness, and vegetation cover. The resolution of these models plays a pivotal role in the accuracy of rockfall simulations. Lower-resolution DEMs tend to oversimplify the terrain's features, leading to inaccurate predictions of rockfall trajectories and energy distribution (Keijsers et al., 2011). Alternatively, higher-resolution DEMs capture fine terrain details, improving the precision of simulations and offering more reliable hazard assessments (Pradhan et al., 2017; Kakavas et al., 2021; Kakavas et al., 2024). Consequently, rockfall simulation software incorporates DEMs of varying spatial resolutions to meet different analytical needs with finer-resolution models, typically producing more detailed and accurate results (Acosta et al., 2002; Baillifard et al., 2003; Kakavas et al., 2023). The scope of this study is to examine the influence of DEM resolution on rockfall simulations in Platiana, Greece, via RocFall 4.0, QProto, and HY-STONE software. The aim is to highlight the importance of DEM resolution in improving hazard predictions.

Study Area

Platiana is a village located in the Ilia prefecture of Peloponnese, Greece (Figure 1). The surrounding area is primarily composed of Upper Cretaceous limestones, as indicated by the engineering geological map of Greece, and is part of the Pindos geotectonic unit according to the Hellenic Survey of Geology & Mineral Exploration (HSGME) (Figure 2). This region is a segment of the broader Pindos Unit that has been thrust westward. Near the settlement, there are significant outcrops of limestone with varying thicknesses from thin to medium layers. According to Vagenas (2020), these limestone layers are locally intercalated with chert layers. Platiana experienced the devastating wildfires of 2007 and has been declared reforesting land over the past years. Following the natural reforestation, the vegetation levels have been fully recovered. However, from 2008 to 2018, the mountain slopes adjacent to Platiana were completely barren (Figure 1). Similar to other cases, the lack of vegetation exposed the slopes to corrosion factors that compromised their structural integrity and triggered the release of internal stresses. As a result, rocks of various sizes became detached from the main rock body and sliding, toppling or falling and proceeding downslope. Notably, on December 4, 2018, after heavy rainfall, a massive boulder approximately 10m³ in volume slid down the slope. Fortunately, it came to a stop in a churchyard, causing no casualties. During its down-ward course, the boulder penetrated two gabion retaining wall that served to protect the Platiana village (Figure 1). It is important to mention that, the rockfall simulations using pre-2018 DEMs (ALOS AW3D30, ASTER GDEM, SRTM30, SRTM90, and TanDEM_X), which capture the barren mountain slopes, demonstrated higher kinetic velocities, whereas those based on post-2018 DSMs (UAV, Greek Cadastral, and Ministry of Agriculture), reflecting restored vegetation, yielded lower kinetic energies.

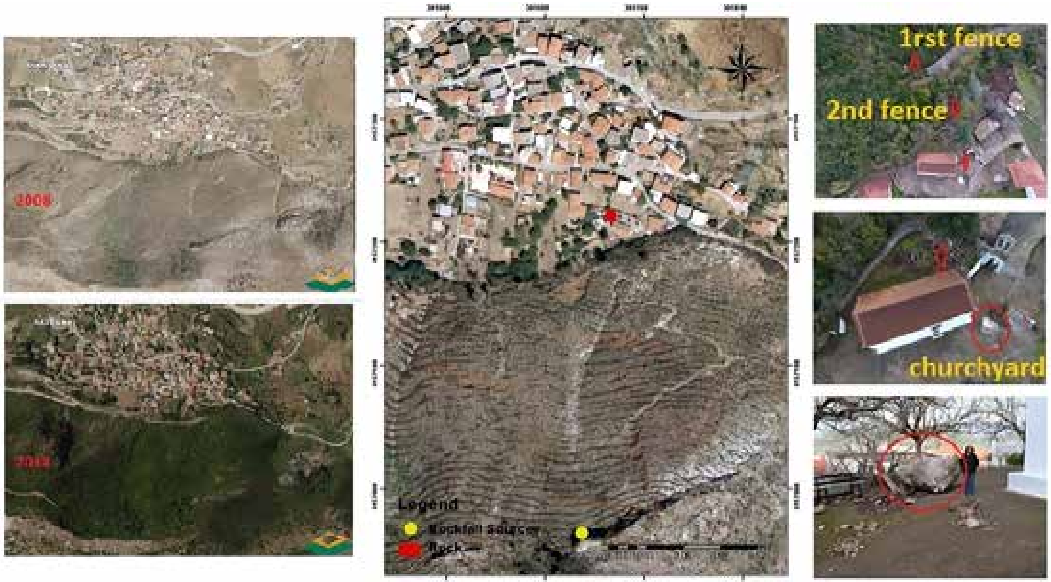

Figure 1. The images on the left (from Greek Cadastral, 2008) and below (2018) illustrate the natural reforestation of the slope adjacent to the Platiana village. The central map indicates both the rockfall source (yellow circle) and the boulder's final point (red circle). On the right, photographs show the aftermath of the rockfall event, including fence damage and the boulder in the churchyard.

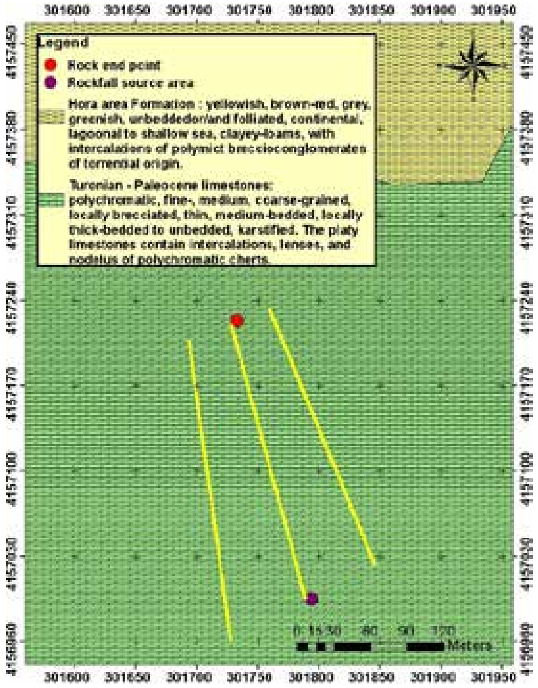

Figure 2. Geological map of the study area according to the Hellenic Survey of Geology & Mineral Exploration (HSGME)

Processing Tools

For this study, three rockfall simulation software were used. The first is RocFall 4.0 from Rocscience, which is a two-dimensional rockfall modeling tool for steep slopes. The detection of rockfall susceptibility is achieved through a lumped mass statistical analysis. This software comprises the collision theory and Newton's laws of motion, so as to simulate the path of the rolling rock mass/boulder (Rocscience, 2002). RocFall software calculates four parameters for the entire slope, including the final position of the rock, bounce height and velocity, as well as energies. The second software is QProto, which is an open-source geographic software and consists a plugin in the QGIS environment

(Castelli et al., 2021). GRASS GIS 7 is the base of this plugin as it optimizes for performance and large geospatial data analysis by offering powerful raster, vector, and geospatial processing engines in a single integrated software suite. It comes with a temporal framework for advanced time series processing and a Python API for rapid geospatial programming (Toma et al., 2021). The third software is HY-STONE which is a software developed for 3D numerical modeling of rockfall processes, including the simulation of the motion of non-interacting blocks, utilizing a high-resolution 3D description of slope geometry for accurate multiscale stochastic modeling (Crosta et al., 2004; Frattini et al., 2008; Agliardi et al., 2009). It is capable of modeling free fall, impact, and rolling of blocks, with energy loss simulations at impacts or by rolling based on a hybrid (cinematic and dynamic) approach.

Rockfall Simulation

For examining Platiana's rockfall phenomenon, slope profiles were selected and extracted from eight different resolution DSMs (Figure 3), aiming at simulations via RocFall, Qproto and HY-STONE software: one 5 cm spatial resolution DSM created by UAV data, one 5 m DSM from the Greek Cadastral, one 20 m DSM from the Ministry of Agriculture, three 30 m resolution DEMs (ALOS AW3D30 DEM, ASTER GDEM and SRTM30 DEM) and two 90 m cell size DEMs (SRTM90 DEM and TanDEM_X). The two barriers, drystone fences, were taken into account in software settings, as well as geological and material characteristics of the slope profiles. In situ surveys and literature data were accomplished (Figure 1) (Depountis et al., 2010; Sabatakakis et al., 2015; Vagenas, 2020).

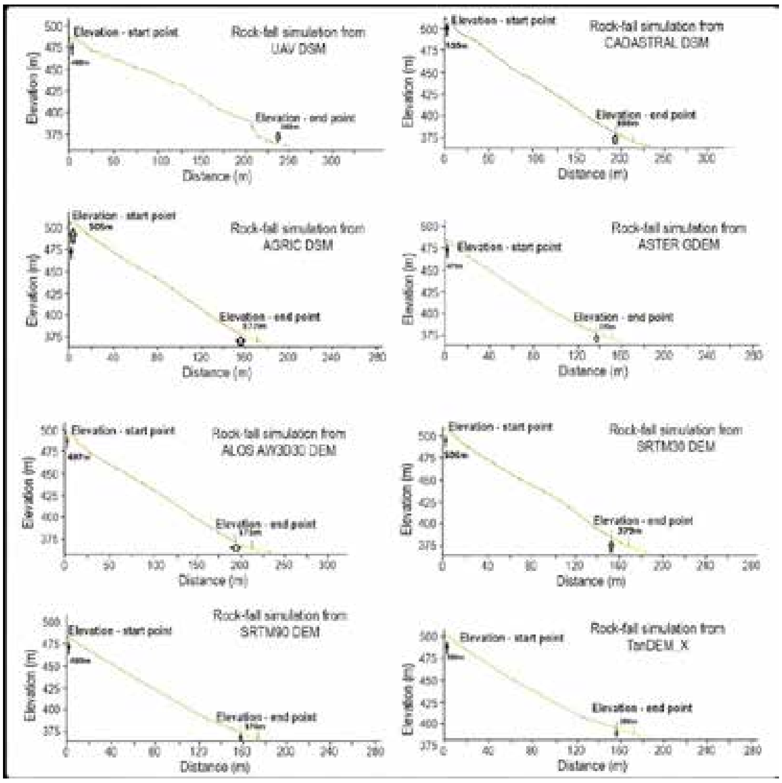

Figure 3. Two-dimensional rockfall simulations via RocFall software for the 2nd slope profile.

According to the figures above, only the UAV DSM created a detailed slope profile, with steep slopes and smooth areas. The other DSMs tended to flatten the topography. The rock in the UAV DSM slope profile jumped the first barrier/fence and broke the second barrier/fence. This result, in comparison with the field observations, is reliable, as the rock stopped a few meters before the end of the slope, in the churchyard (Figure 1). In the DSM from the Greek Cadastral, DSM from the Ministry of Agriculture, ALOS AW3D30 DEM, ASTER GDEM, SRTM30 DEM, SRTM90 DEM and TanDEM_X slope profiles, the rock rolled and stopped in the first barrier/fence. This is in contrast to the real trajectory. Therefore, only the UAV DSM simulated a trajectory close to the real.

- **<u>RocFall results</u>**

The total kinetic energy distribution was computed via RocFall software in the middle of the slope profile, at x = 117.3 m, and is presented below (Figure 4). The geological and material characterizes of the rockfall were taken into account. More specifically, the coefficient of normal restitution (Rt) has a mean value of 0.39 and a standard deviation of 0.04, while the coefficient of tangential restitution (Rn) has a mean of 0.80 with the same standard deviation. The friction angle (Phi) averages 15° (standard deviation 2°), and the mean horizontal velocity reaches 11 m/s (standard deviation 1.1 m/s).

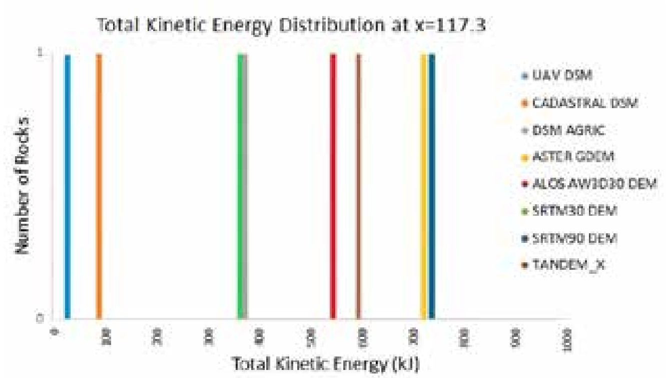

Figure 4. Total kinetic energy distribution at x = 117.3 m for the slope profile via RocFall

Figure 4 illustrates how total kinetic energy—measured at x = 117.3 m along the slope—varies for a single rockfall simulation when using different elevation models in RocFall. Each colored bar corresponds to a specific DSM/DEM, with higher bars positioned farther along the x-axis indicating larger kinetic energies. The UAV DSM and Greek Cadastral DSM (blue and orange bars), which have finer spatial resolutions, yield the lowest kinetic energies (roughly 20–90 kJ). By contrast, the Ministry of Agriculture DSM and SRTM30 DEM (green and grey bars) display moderate energy levels (about 360–380 kJ). The coarsest models, ALOS AW3D30 DEM, ASTER GDEM, SRTM90 DEM, and TanDEM_X (red, yellow, dark-blue, and brown bars) produce the highest energy values (560–730 kJ), since smoothing out the terrain in lower-resolution data allows the rock to accelerate more. Overall, the DSMs with coarser spatial resolution (more than 30 m) flattened the relief; consequently, the rock recorded higher speed than in the other DSMs with high spatial resolution (less than 30 m), which created unsmooth surfaces

- **<u>QProto results</u>**

For examining Platiana rockfall phenomenon and extract maps, in terms of the total weighted kinetic energy (J), QPROTO analysis were accomplished in this section (Figure 5a-5d). The slope and material characteristics which derived from in situ surveys and literature data were defined (Depountis et al., 2010; Sabatakakis et al., 2015; Vagenas, 2020). The energy angle φp is 30°, the forest coverage is dense vegetation in limestones and the propensity index is 1.

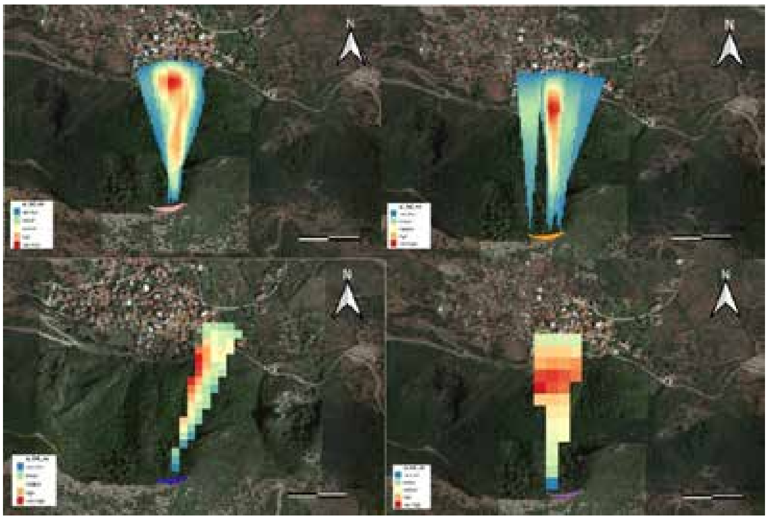

Figure 5. QPROTO results, in terms of total weighted kinetic energy (J), for the site of Platiana. a) UAV DSM, b) Greek Cadastral DEM, c) DSM from the Ministry of Agriculture d) ALOS AW3D30 DEM.

In Figure 5a, the UAV DSM (0.1 m resolution) generated 93,155 source points (pink polygon), necessitating resampling to 5×5 m for faster processing. The QPROTO map shows high to very high total weighted kinetic energies in the slope's center, tapering to very low at the edges, with the northern sector exhibiting the highest values. In Figure 5b, the Greek Cadastral DSM (5 m resolution) yielded just 36 source points (orange polygon), capturing very low to medium energies over two-thirds of the area and higher levels near the slope's end, especially in the north—consistent with in situ observations that place the rock's stopping point in the churchyard, where energies peaked. Although the Greek Cadastral DSM aligns with the UAV DSM, it positions the cone a few meters farther and reveals an exposed block area on the cone's left side. The Ministry of Agriculture DSM (20 m resolution, Figure 5c) produced only two source points (blue region). This analysis shows very low energies in the south, low to medium in the east-north, and high to very high in the west, yet contradicts field data by displaying high values prematurely. Finally, Figure 5d presents the ALOS AW3D30 DEM (30 m resolution) with three source points, indicating low to medium energies over most of the cone, very high in its middle, and an endpoint that stops short of the actual stopping point, rendering this analysis more conservative.

- **<u>HY-STONE results</u>**

For the rockfall analysis, six DEMs were used, covering a resolution range from 5 m to 90 m. The coefficients of restitution E_N and E_T, and the rolling friction coefficient A_T, were back-calibrated on the higher-resolution DEM based on the rockfall event (Table 1). The masonry stone walls were simulated with low values of E_N and E_T and high values of A_T, similarly to buildings. Given that HY-STONE operates on a stochastic model, simulations were performed with 1000 rocks to provide a more accurate representation of rockfall dynamics. The following data presents the maximum translational kinetic energies for the Platiana rockfall, expressed in kJ (Figure 6).

Table 1. Coefficients of restitution and rolling friction in Platiana rockfall, calibrated on the Greek Cadastral DEM

Description	E_N	E_T	A_T
Houses	0.20	0.20	1.00
Road- asphalt	0.55	0.70	0.25
Debris well vegetated	0.35	0.60	0.42
Debris without vegetation	0.40	0.65	0.35
Stone wall	0.20	0.20	1.00

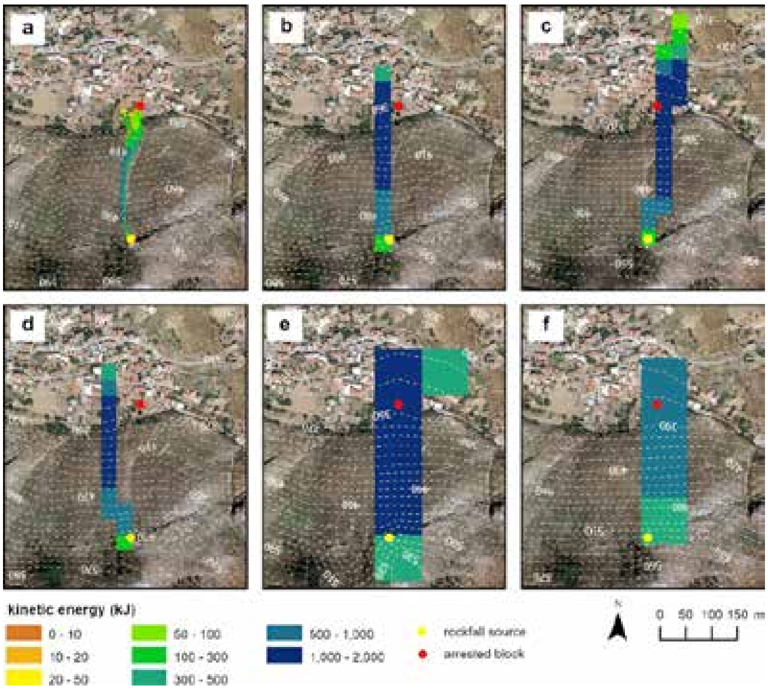

Figure 6. HY-STONE results, in terms of in terms of the maximum translation kinetic energy for the site of Platiana. a) Greek Cadastral DEM, b) ALOS AW3D30 DEM, c) ASTER GDEM, d) SRTM30 DEM, e) SRTM90 DEM and f)TanDEM_X.

In Figure 6, the Greek Cadastral DEM (a) shows high to very high kinetic energies (0–1,500 kJ) near the rockfall source and centrally, then decreasing to very low at the slope's end; the ALOS AW3D30 DEM (b) starts with low energies near the source, rises to high in mid-path, and declines with medium energies at the end; the ASTER GDEM and SRTM30 DEMs (c, d) depict multiple paths with low energies (0–1 kJ) at the source, high energies (100–1,500 kJ) in the middle, and medium levels (0.1–100 kJ) in residential areas—extending beyond the actual endpoint; the SRTM90 DEM (e) generates two paths showing very high energies (500–1,500 kJ) at the endpoint and low energies (0.2–1 kJ) near the source; and TanDEM_X (f) presents a single trajectory transitioning from medium to high, then very high, and finally back to medium and low energies, likewise extending past the real endpoint.

Conclusions

The findings of this study highlight the importance of DSM resolution in rockfall simulations. The area of interest has been extensively observed since the occurrence of the rockfall events. Therefore, a plethora of in situ measurements and observations have been recorded and many geo-data sets have been collected. These data significantly contribute towards the extraction of a reliable 2D rockfall simulation, with relatively small discrepancies from the observations of the real event.

1. DSMs from UAV data with sub-decimeter spatial resolution proved to be the most accurate for a rockfall simulation.
2. The UAV offers a significantly different pathway among different rock paths, whereas the other DSMs have a simplified path of the fallen blocks.
3. The DSMs can be classified into three categories according to their accuracy in rock-fall simulation. In particular:
(i) High accuracy, which corresponds to DSMs with spatial resolution less than 5 m, such as UAV DSM and DSM from the Greek Cadastral. The processing of these DSMs in RocFall software extracted results similar to in situ observations.
(ii) Medium accuracy which corresponds to DSMs with spatial resolutions ranging from 20 m to 30 m, such as DSM derived from the Ministry of Agriculture, ALOS AW3D30 DEM, ASTER GDEM and SRTM30 DEM. Against all these DSMs, only DSM of the Ministry of Agriculture and ALOS AW3D30 DEM offered rockfall illustration relatively close to the real event.
(iii) Low accuracy, which corresponds to DSMs with spatial resolution of 90 m, such as SRTM90 DEM and TanDEM_X, and led to rockfall conclusions that abstain from the reality.
4. The existence of vegetation plays an important role in the simulation of the rockfalls and a recent and very accurate DSM from UAV can represent the real height of the vegetation in contrast to the free available DSMs, such as SRTM 30DEM or ASTER DEM that were created few years ago.
5. The coarse resolution of SRTM 90DEM and TanDEM_X may lead to the inaccurate slope profiles and to the erroneous calculations of the rock kinetic energy. Previous rockfall simulation studies based on SRTM90 or TanDEM_X DSMs should be re-evaluated.

Acknowledgements

The authors would like to thank Prof. Paolo Frattini from the University of Bicocca, Milan, for providing access to the HY-STONE software and for his valuable contributions.

References

Acosta, E., Agliardi, F., Crosta, G.B., Rıos Aragues, S., 2002. Regional Rockfall Hazard Assessment in the Benasque Valley (Central Pyrenees) Using a 3D Numerical Approach. In Proceedings of the 4th EGS Plinius Conference—Mediterranean Storms, Mallorca, Spain, p. 555–563.

Agliardi, F., Crosta, G.B., Frattini, P., 2009. Integrating rockfall risk assessment and countermeasure design by 3D modelling techniques. Nat. Hazards Earth Syst. Sci. 9, 1059–1073.

Baillifard, F., Jaboyedoff, M., Sartori, M., 2003. Rockfall hazard mapping along a mountainous road in Switzerland using a GIS-based parameter rating approach. Nat. Hazards Earth Syst. Sci. 3, 435–442.

Borella, J., Quigley, M., Krauss, Z., Lincoln, K., Attanayake, J., Stamp, L., .. Gravley, D., 2019. Geologic and geomorphic controls on rockfall hazard: how well do past rockfalls predict future distributions?. Natural Hazards and Earth System Sciences, 19(10), 2249-2280.

Castelli, M., Torsello, G., Vallero, G., 2021. Preliminary Modeling of Rockfall Runout: Definition of the Input Parameters for the QGIS Plugin QPROTO, Geosciences 11, 88.

Crosta, G.B., Agliardi, F., 2004. Parametric evaluation of 3D dispersion of rockfall trajectories. Nat. Hazards Earth Syst. Sci. 4, 583–598.

Depountis, N., Lainas, S., Pyrgakis, D., Sabatakakis, N., Koukis, G., 2010. Engineering geological and geotechnical investigation of landslide events in wildfire affected areas of Ilia Prefecture,Western Greece. Bull. Geol. Soc. 43, 1138–1148.

Dorren, L., 2003. A review of rockfall mechanics and modelling approaches. Progress in Physical Geography 27(1), 69–87.

Fell, R., Corominas, J., Bonnard, C., Cascini, L., Leroi, E., Savage, W.Z.; 2008.Guidelines for landslide susceptibility, hazard and risk zoning for land use planning. Eng. Geol. 102, 85–98.

Frattini, P., Crosta, G., Carrara, A., Agliardi, F., 2008. Assessment of rockfall susceptibility by integrating statistical and physically-based approaches. Geomorphology 94, 419–437.

Guzzetti, F., Crosta, G., Detti, R., Agliardi, F., 2002. STONE: A computer program for the three-dimensional simulation of rockfalls. Comput. Geosci. 28, 1079–1093.

https://grass.osgeo.org/grass78/manuals/r.viewshed.html (accessed on 14 January 2021).

Hungr, O., Evans, S.G., Hazzard, J., 1999. Magnitude and frequency of rockfalls and rock slides along the main transportation corridors of southwestern British Columbia. Canadian Geotechnical Journal 36(2), 224-238.

Jaboyedoff, M., Derron, M.-H., Blikra, L.H., 2005. Preliminary assessment of rockslide and rockfall hazards using a DEM (Oppstadhornet, Norway). Natural Hazards and Earth System Sciences 5, 285-292.

Kakavas, M., Frattini, P., Previati, A., Nikolakopoulos, K., 2024. Evaluating the Impact of DEM Spatial Resolution on 3D Rockfall Simulation in GIS Environment. Geosciences, 14(8), 200.

Kakavas, M., Nikolakopoulos, K., 2021. Digital Elevation Models of Rockfalls and Landslides: A Review and Meta-Analysis. Geosciences 11, 256.

Kakavas, M., Nikolakopoulos, K., Kyriou, A., Koukouvelas, I., 2023. The Influence of the DEM Spatial Resolution in Rockfall Simulation and Validation with In Situ Data. Geosciences 13, 57.

Keijsers, J.G.S., Schoorl, J.M., Chang, K.-T., Chiang, S.-H., Claessens, L., Veldkamp, A., 2011. Calibration and resolution effects on model performance for predicting shallow landslide locations in Taiwan. Geomorphology 133, 168–177.

Pradhan, B., Sameen, M.I., 2017. Effects of the Spatial Resolution of Digital Elevation Models and Their Products on Landslide Susceptibility Mapping. In Laser Scanning Applications in Landslide Assessment; Springer: Berlin/Heidelberg, Germany, p. 133–150.

Rocscience., 2002 RocFall software—For risk analysis of falling rocks on steep slopes. In Rocscience User’s Guide; Rocscience: Toronto, ON, Canada.

Sabatakakis, N., Depountis, N., Vagenas, N., 2015. Evaluation of Rockfall Restitution Coefficients. Eng. Geol. Soc. Territ. 2, 2023–2026.

Toma, L, Zhuang, Y., Richard, W., Metz, M. GRASS GIS Manual. Available online

Vagenas, N., 2020. Rockfall Simulation by Analytical Methods. Correlation of Rockfall Energy Dissipation Parameters and Rock Mass Characteristics. Ph.D. Thesis, University of Patras, Greece, Department of Geology, Patras, Greece.

Wu, M., Luo, G., Hu, X., Bi, Y., Wang, Y., Ma, N., 2025. Dynamic fragmentation analysis of potential rockfall hazards at Zixia hydropower dam, Qinghai-Tibet plateau. Journal of Rock Mechanics and Geotechnical Engineering.

17th INTERNATIONAL CONGRESS
of the Geological Society of Greece

BULLETIN OF THE GEOLOGICAL SOCIETY OF GREECE, SP. PUBL.

EXTENDED ABSTRACT 123

The late Ruscinian leporid *Trischizolagus* (Leporidae, Lagomorpha) from Megalo Emvolon (Thessaloniki, Greece)

Christina N. Kalaitzi[1], Dimitris S. Kostopoulos[1]
(1) Laboratory of Geology and Palaeontology, School of Geology, Aristotle University of Thessaloniki, 54124 Thessaloniki, Greece

Introduction – Fossiliferous site

Since 2017, ongoing field campaigns at Megalo Emvolon have led to the discovery of a new fossil site, Megalo Emvolon-4 (MVL), which has yielded, inter alia, an abundance of lagomorph fossils. This paper introduces the newly discovered leporid collection (Leporidae, Mammalia) at MVL, featuring exceptionally well-preserved cranial, postcranial, and dental fossil remains. All specimens are attributed to *Trischizolagus dumitrescuae*, the most prevalent and widespread species of the genus during the Early Pliocene (Ruscinian) in Europe. Originally discovered in Romania, *Trischizolagus dumitrescuae* has since been identified at more than fifteen fossil sites across Eurasia (Averianov and Tesakov, 1997; Čermák and Wagner, 2013; Čermák *et al.,* 2021; and others).

The sediments in the Megalo Emvolon area are part of the Gonia Formation (Fm) and are indicative of a fluvio-lacustrine depositional environment with frequent river discharges and shallow lakes (Syrides, 1990). Alternating lenses and intercalated beds of clays, silts, marls, sands, sandstones, massive marly limestones, and gravels constitute the sedimentary sequence in the Megalo Emvolon area. Small pockets or spots, ranging from 0.5 to 3 meters in length, typically concentrate fossils at the site, scattered across various stratigraphic levels. Koufos *et al.* (1991) identified three fossil horizons within the Megalo-Emvolon section, with MVL either correlated with the basal or middle fossiliferous level (MEV, MEM) or situated in between both levels. The Megalo Emvolon fauna is dated to the Late Ruscinian, MN 15 (Koufos *et al*., 1991; Koufos, 2006) (about 4.2–3.2 Ma, according to http://paleobiodb.org).

The MVL *T. dumitrescuae*

Overall, the leporid material of this study is in excellent condition, with only a few incomplete specimens or fragments. The MVL material comprises 383 specimens, out of which 26 are cranial, 212 are dental (146 upper and 66 lower), and 145 are postcranial (11 bone groups), all in outstanding condition (Fig 1). Significantly, this study presents the first discovery of well-preserved skulls of *T. dumitrescuae* at Megalo Emvolon, providing unprecedented insights into its cranial morphology. The identification of *T. dumitrescuae* is solely based on the morphology of p3 and is strongly supported by comparisons with Romanian samples among other localities, alongside a detailed analysis of several morphometrical traits. The p3 exhibits the typical tetralobed trigonid form, a well-developed mesoflexid and hypoflexid, and a 1:2 size ratio between the length of the trigonid and the talonid. Moreover, the so-called "*Alilepus* pattern" is the predominant morphotype across all MVL material. Regarding the cranial anatomy, *T. dumitrescuae* has a large and acute cranium that is highly fenestrated, especially in the premaxillary, maxillary, and frontal regions, and exhibits a set of supraorbital processes that are not so well developed. Regarding the postcranial material, the forelimb features a scapula with a broad neck and a narrow coracoid process positioned close to the glenoid cavity. The humerus is characterized by a prominent deltoid crest. In the hindlimb, the femur's proximal trochanters are closely spaced, while the pelvis displays a robust ilium and a wide ischial tuberosity. Additionally, the calcaneus has an elongated body.

Conclusions

The material from MVL significantly expands upon earlier records from the site (Koufos and Koliadimou, 1993), providing valuable new insights into the previously unknown cranial morphology of *T. dumitrescuae*, its intraspecific dental variability, and locomotive tendencies, while also refining the genus and species diagnostic characteristics, correcting earlier misconceptions, and establishing intraspecific variation in comparison to other European records. The description of the cranium of *T. dumitrescuae* reveals a unique combination of *Lepus*- and *Oryctolagus*-like features that differentiate it from both the Eurasian *Alilepus* and the African *Serengetilagus*. The dental shape and size of MVL are consistent with those of dental remains from Megalo Emvolon-1 (Koliadimou and Koufos, 1993), as well as those of *T. dumitrescuae* from the type locality in Măluşteni, Romania. Lastly, preliminary ecomorphological analysis based on limb and skull morphology of *T. dumitrescuae* in MVL reflects adaptations for swift movement, high jumping, and capability for digging.

Figure 1. Craniodental and postcranial material of *T. dumitrescuae* in MVL.

Acknowledgements

The authors express their sincere gratitude to Dr. Lars von den Hoek Ostende and Pepijn Kamminga, MSc, of the Naturalis Biodiversity Center, for providing recent leporid specimens essential to the comparative study. Special thanks are also extended to Dr. Georgios Konidaris and Stylianos Koutalis, MSc, from the Department of Geosciences, Palaeoanthropology section, at Eberhard Karls Universität Tübingen, for their assistance with 3D scanning. Finally, we deeply appreciate Dr. Stanislav Čermák for generously sharing raw data on the *Trischizolagus* p3.

References

Averianov, A.O., Tesakov, A.S., 1997. Evolutionary trends in Mio-Pliocene Leporinae, based on *Trischizolagus* (Mammalia, Lagomorpha). Paläontologische Zeitschrift 71, 145-153.

Čermák, S., Wagner, J., 2013. The Pliocene record of *Trischizolagus* and *Pliopentalagus* (Leporidae, Lagomorpha, Mammalia) in Central Europe, with comments on taxonomy and evolutionary history of Leporinae. Neues Jahrbuch für Geologie und Paläontologie 268, 97-111.

Čermák, S., Angelone, C., Moncunill-Solé, B., 2021. *Prolagus* Pomel, 1853 (Lagomorpha, Mammalia) in the framework of the Pliocene faunal rearrangements in central Europe. Comptes Rendus Palevol 28, 597-617.

Koufos, G.D., 2006. The Neogene mammal localities of Greece: faunas, chronology and biostratigraphy. Hellenic Journal of Geosciences 41, 183-214.

Koufos, G.D., Syrides, G., Koliadimou, K., 1991. A Pliocene primate from Macedonia. Journal of Human Evolution 21, 283-294.

Koufos, G.D., Koliadimou, K., 1993. Two lagomorphs from the Pliocene of Macedonia (Greece). Bulletin of the Geological Society of Greece 28, 117-129.

Syrides, G., 1990. Lithostratigraphic, biostratigraphic and palaeogeographic study of the Neogene – Quaternary sedimentary deposits of Chalkidiki Peninsula, Macedonia, Greece. Ph.D. Thesis, Aristotle University of Thessaloniki, Thessaloniki, 243 p.

17th INTERNATIONAL CONGRESS of the Geological Society of Greece

BULLETIN OF THE GEOLOGICAL SOCIETY OF GREECE, SP. PUBL.

EXTENDED ABSTRACT 124

Multiscale Geo-visualization Dashboard of Persistent Scatterer Interferometry SAR Data, Lesvos Island, Greece

Panagiotis Kalaitzis[1], Michael Foumelis[2], Antonios Mouratidis[2] and Nikolaos Soulakellis[1]

(1) Department of Geography, University of the Aegean, Mytilene, Greece, p.kalaitzis@geo.aegean.gr

(2) Department of Physical and Environmental Geography, Aristotle University of Thessaloniki, Thessaloniki, Greece

Research Highlights

This study emphasizes the importance of effective visualization for Persistent Scatterer Interferometry (PSI) data, particularly in capturing the dynamic and spatiotemporal aspects of ground displacement. A novel multiscale generalization algorithm was developed to optimize PSI dataset visualization across eight predefined cartographic scales, ensuring suitability in each cartographic scale. An interactive dashboard was designed to properly visualize PSI data of different geographic, cartographic, spatial, and temporal scales, combined with auxiliary geospatial data, addressing the need for intuitive cartographic tools. The results highlight the importance of visualizing and studying PSI data through interactive dashboards, applying the classic principles of cartography. This approach underscores their role as innovative tools for understanding and monitoring the dynamic behavior of surface motion.

Introduction / Background

The rapid increase in the availability of earth observation (EO) data has introduced a critical demand for precise, user-friendly, and interactive dashboards that facilitate the thorough analysis of these vast and complex datasets (Gehlot & Hanssen, 2008). Despite significant advancements, the interpretation of EO data remains a challenging endeavor due to their spatial and temporal intricacies. Advances in geospatial data visualization have provided efficient, low-cost methodologies for analyzing and interpreting geospatial information (Kraak & Ormeling, 2020). Among these, Persistent Scatterer Interferometry (PSI) has emerged as a highly effective technique for monitoring ground deformation and instability phenomena. Utilizing spaceborne synthetic-aperture radar (SAR) imagery, PSI achieves millimeter-level precision in detecting surface motion over extensive spatial domains, serving as a key tool in geosciences, urban planning, and environmental disciplines (Crosetto *et al*., 2016).

PSI data provide valuable insights into a broad spectrum of dynamic processes, including land subsidence, landslides, volcanic activity, and infrastructure stability. However, the technique is inherently dependent on persistent scatterers (PS), which exhibit consistent radar reflectivity over time. The spatial density of PS can be limited in non-urban environments where suitable targets are sparse. To overcome this limitation, distributed scatterers (DS)—targets with consistent scattering behavior within radar resolution cells—are integrated with PS measurements, significantly enhancing spatial coverage. The combined PS/DS solution enables more detailed analyses by increasing point density, particularly in densely vegetated or sparsely built-up areas (Foumelis *et al*., 2022).

Recently, algorithms for performing multi-temporal interferometric analysis have been seamlessly integrated into cloud platforms, providing users with operational and automated services. This integration significantly reduces the need for extensive data storage, computational resources, and specialized expertise in executing complex processing chains. An example of such a service is the surface motion mapping (SNAPPING) service integrated on the Geohazards Exploitation Platform (GEP). SNAPPING is a PSI chain designed specifically for the Copernicus Sentinel-1 mission, capable of generating average motion and corresponding displacement time-series at various spatial resolutions.

However, effective visualization of PSI data remains a challenge, particularly at multiple scales and resolutions. The spatial and temporal complexity of PSI data necessitates the development of innovative visualization methods to support comprehensive analysis. Generalization techniques, such as point aggregation and elimination, are employed to adapt datasets to predefined cartographic scales while mitigating challenges posed by overlapping points in high-density areas (Kalaitzis *et al*., 2023; Poncoş *et al*., 2022).

Existing platforms, such as the European Ground Motion Service and national services in Germany, Norway and the Netherlands, demonstrate the utility of PSI web applications in monitoring ground motion. The dashboard employs a cohesive, interactive design centered around a web map that serves as a primary visualization element. Complementing this, key performance indicators (KPIs) provide high-level insights, while dynamic graphs depict trends and relationships in the data. Accompanying these are structured **lists** that offer detailed tabular information.

All components are interconnected: any selection or interaction within one-such as clicking on a map region, a data point in a graph, or a list item-immediately updates the other components, ensuring a synchronized and contextualized user experience. This architecture enables seamless data exploration and decision-making (Bach *et al*., 2022).

Interactive dashboards offer dynamic tools for visualizing and exploring PSI datasets. Providing tools such as data filtering, time-series graphs creation and comparison with auxiliary geospatial data, dashboards enable both expert and novice users to interact with and interpret ground deformation data effectively. By combining original and generalized datasets in areas with varying densities, dashboards help manage cartographic challenges and offer insights into intricate geospatial information.

This study introduces a novel approach to address the challenges of visualizing and exploring PSI datasets of different spatial resolutions, in predefined cartographic scales. This approach is based on the development of a standalone dashboard, providing interactive cartographic tools designed to optimize the visualization and exploration of PSI datasets. The dashboard represents a low-cost solution that can be tailored with any generic PSI dataset, in order to offer users invaluable insights into such intricate geospatial information.

Methods

The methodology of this study is represented by the flowchart in Figure 1, consisting of three main steps.

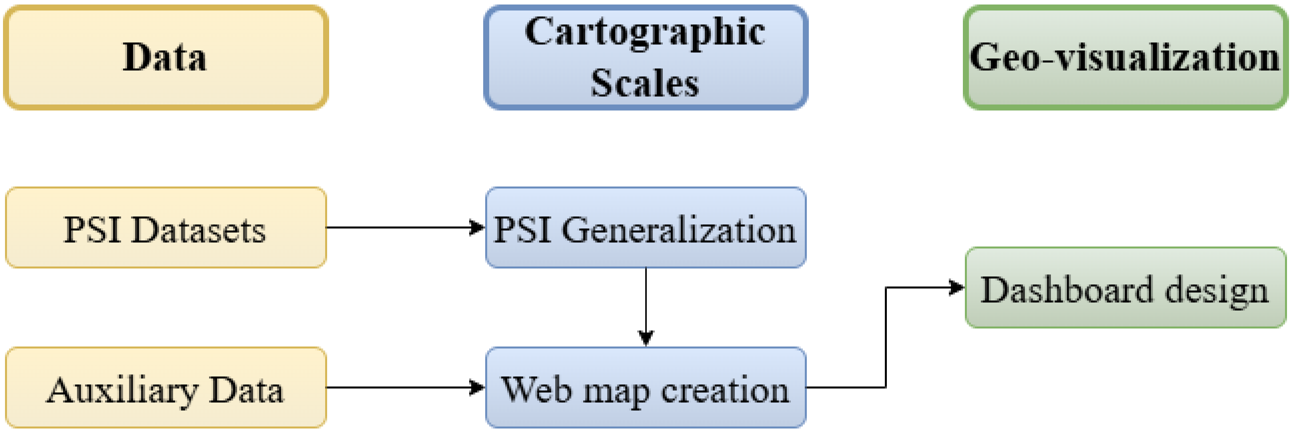

Figure 1: Overall workflow chart of the methodology followed for the integration of the research

1. Data: Describing all the PSI datasets generated and the auxiliary data used for the needs of the current study, as well as for visualization.

PSI Data

The processing of Sentinel-1 SAR data is performed using the SNAPPING service on GEP, where PSI services are available at different spatial resolutions. For this study, two resolution datasets (PSI Med and PSI Full) were utilized. SNAPPING offers three distinct services: the SNAPPING IFG service, which generates interferometric stacks, and the SNAPPING PSI Med (i) and SNAPPING PSI Full (ii) services, which conduct PSI analyses at medium and full resolutions, respectively. Additionally, SNAPPING provides a PSI time-series analysis service for both resolutions (Foumelis et al., 2022).

PSI processing focused on PS/DS (iii) scatterers was carried out using the infrastructure of Aristotle University of Thessaloniki (AUTh), utilizing the SNAPPING IFG outputs, including differential interferograms and auxiliary data, previously generated on GEP. To ensure measurement consistency, common processing parameters were applied to all solutions, with adjustments made for deviations caused by different references.

According to specific criteria, the detected Persistent Scatterer (PS) targets from the SNAPPING PSI Med dataset were initially merged within a 100-meter search radius, reducing the number of targets in areas with high point density. For SNAPPING PSI Full, no merging of neighbouring PS targets was performed, preserving the original sensor resolution. Compared to PS-InSAR, DS-InSAR results significantly enhance the spatial distribution density of point targets, particularly in regions with lower coherence (Foumelis *et al*., 2022).

PSI Med and Full resolution datasets consist of 45,749 and 283,419 PSs respectively, geolocated in the broader area of Lesvos Island, for the period between 2015–2020. PS/DS dataset consists of 11,169 points for the period between 2019-2021 and located in the broader area of Bali Alonia Park.

Auxiliary data

PSI data are integrated with auxiliary datasets to meet visualization requirements and enable enhanced utilization. The auxiliary datasets include: A geology layer, digitized from the freely available geological map of Greece (1:500,000), provided by the Hellenic Geological and Mining Research Authority (E.A.G.M.E) and ESA Land Cover 2020 dataset, with a spatial resolution of 10 meters.

2. Cartographic scales: Based on previous studies (Kalaitzis *et al*., 2023; Poncoş *et al*., 2022), the necessity for PSI interpretation aligned with pre-specified scales becomes evident. By combining the coverage area of each PSI dataset with various geographic scales (e.g., regional scale, local scale), eight predefined cartographic scales are derived:

- 1:1,000,000
- 1:500,000
- 1:200,000
- 1:100,000
- 1:50,000
- 1:20,000
- 1:10,000
- 1:5,000

An algorithm for generalizing PSI datasets was developed, in order to avoid point overlapping especially on smaller cartographic scales (Kalaitzis *et al*., 2024). More extensively, based on the visual acuity of the human eye in each predefined cartographic scale, eight grids with corresponding cell sizes were created, as presented in Table 1.

Table1: Predefined cartographic scales used for visualization, followed by the PSI dataset visualized in each case. For generalization needs, a grid was created for each cartographic scale, with the corresponding cell size. For each cartographic scale, a dataset (either generalized or not) is generated with the corresponding number of points and point density.

Cartographic Scale	Cell Size (m)	PSI Dataset	No. of Points	Point Density (points/km^2)
1:1,000,000	250	PSI Med	14,348	15
1:500,000	125	PSI Med	31,189	66
1:200,000	50	PSI Med	45,749	99
1:100,000	25	PSI Full	158,030	376
1:50,000	12,5	PSI Full	231,166	507
1:20,000	5	PSI Full	283,419	580
1:10,000	2,5	PS/DS	11,169	9422
1:5,000	1,25	PS/DS	11,169	9422

After applying a generalization algorithm to all available PSI datasets, it is derived that each original PSI dataset is best visualized at a specific cartographic scale, determined by the point density of the dataset. In every other cartographic scale, generalized datasets are used for visualization.

After this procedure, all PSI datasets were joined with auxiliary data and uploaded on a server provided by ArcGIS Enterprise™ platform. Through this platform a web map, consisting of all available data, was created.

3. Geo-visualization: Based on the web map created, an interactive dashboard was created consisting of the basic viewer of the application (web map), combined with several cartographic tools, providing crucial information about each points' attributes (mean v
4. elocity, velocity uncertainty, temporal coherence, cumulative deformation, time-series, geology and land use).

Results

An interactive dashboard developed, contributing in proper visualization and exploration of different resolution PSI datasets in multiple cartographic scales. The main component of this platform, is the web map, providing visualization of mean velocities of PSI datasets and exploration through the study area. Navigation along the study area, is also enhanced by predefined bookmarks, zooming in specific areas of Lesvos Island. A base map list is also available, allowing users to customize it according to their preferences. The map is combined with four different indicators about mean velocity, temporal coherence, velocity uncertainty and cumulative deformation. Time-series graph, presenting ground deformation of points through time, is also available. The time-series graph tool allows users to zoom in on shorter time periods within the graph using a scrollbar. The indicators and the time-series graph display the mean values of the attributes they represent. Lists of geology and land use of points, are also provided as tools. Each one of the tools is linked with the map, so every adjustment by the users (selection, pan, zoom) affects both the map and the tools. Selection of single or multiple points from the map, also updates indicators, time-series graph and lists. Dashboard is accessible by the link: Multiscale Geo-visualization Dashboard for PSI Measurements, Lesvos A preview of the dashboard is presented in Figure 2.

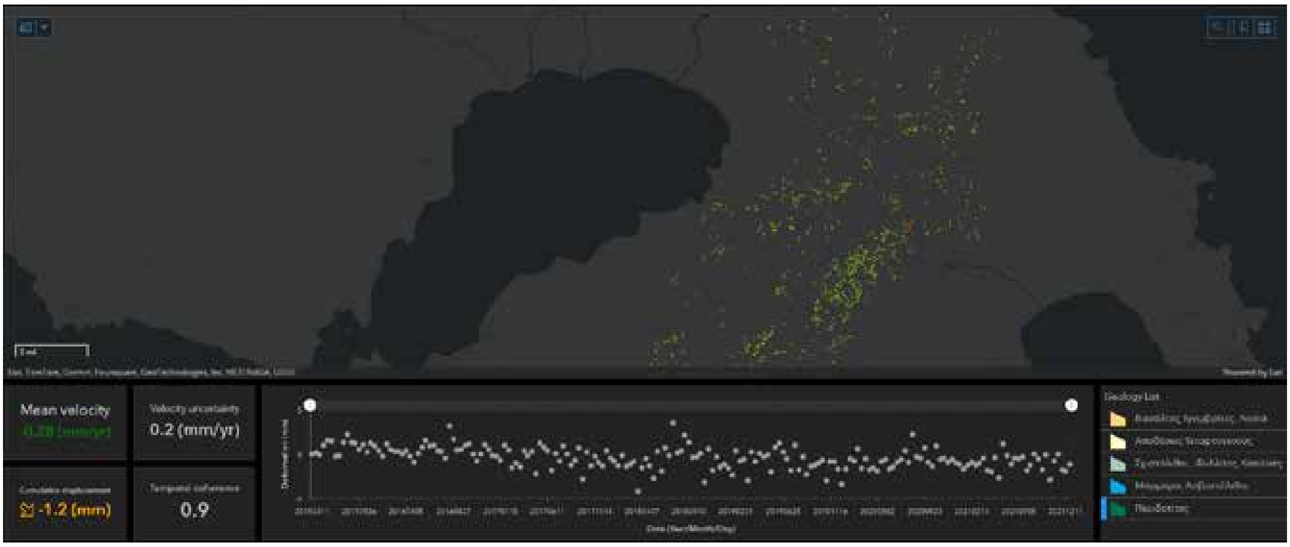

Mean velocity

Velocity uncertainty
0.2 (mm/yr)

Cumulative displacement
-1.2 (mm)

Temporal coherence
0.9

Figure2: A preview of the dashboard, visualizing mean velocities of PSI med resolution dataset, in scale 1:200.000. Only points referring to peridotites are filtered and displayed; cartographic tools are adjusted accordingly. Mean velocity of filtered points is -0.28mm/yr with a velocity uncertainty of 0.2mm/yr, cumulative deformation is -1.2mm and temporal coherence is 0.9.

Limitations mainly refer in the availability of cartographic tools, which may not cover all user needs for advanced data analysis or visualization. Customization options for the tools are restricted, making it challenging to tailor the dashboard to specific workflows or preferences. While functional, the dashboard's tools are constrained by its simplified design, prioritizing ease of use over extensive configurability. Another limitation arises concerning the application of generalization algorithm on PSI datasets. More specifically, during the generalization process, the number of points in each generalized dataset is reduced compared to the original. In the cartographic scales where generalized datasets are used, information regarding individual ground displacement values per date is absent. Consequently, time-series analysis is not feasible at these cartographic scales. To address this limitation, time-series graphs are exclusively generated for the original datasets at their corresponding cartographic scales.

Conclusions

The utilization of the multiscale geo-visualization dashboard facilitates the effective exploration of various PSI datasets, enabling easier extraction of ground motion information and valuable insights into the prevailing conditions. The integration and seamless interaction between the web map and the cartographic components result in an accessible and fully operational tool for interactive data visualization applicable to any generic PSI dataset and individual case studies.

Generalized PSI datasets enable accurate and effective visualization of measurements across multiple cartographic scales, facilitating qualitative data interpretation. Each original PSI dataset is optimally visualized at a specific cartographic scale, dictated by the dataset's point density. Visualizing original datasets at their corresponding optimal cartographic scales not only ensures precise depiction of ground displacement but also enables comprehensive qualitative and quantitative spatiotemporal analyses, such as time-series graphs generation.

By visualizing mean velocities of different resolution PSI datasets, via the multiscale geo-visualization dashboard, reveals that Lesvos Island is not characterized by significant ground deformation. Negative velocity rates between -5 mm/year and -8 mm/year, indicative of land subsidence, are observed in the eastern part of the island near Lampou Mili village. Conversely, positive velocity rates indicating uplift, reaching up to 2 mm/year, are concentrated in the northern region, between Mythimna and Efthalou.

References

Bach, B., Freeman, E., Abdul-Rahman, A., Turkay, C., Khan, S., Fan, Y., & Chen, M., 2022. Dashboard Design Patterns. IEEE

Transactions on Visualization and Computer Graphics 29(1), 1–11. https://doi.org/10.1109/TVCG.2022.3209448

Crosetto, M., Monserrat, O., Cuevas-González, M., Devanthéry, N., & Crippa, B., 2016. Persistent Scatterer Interferometry: A review. ISPRS Journal of Photogrammetry and Remote Sensing 115, 78–89. https://doi.org/10.1016/j.isprsjprs.2015.10.011

Foumelis, M., Delgado Blasco, J. M., Brito, F., Pacini, F., Papageorgiou, E., Pishehvar, P., & Bally, P., 2022. SNAPPING Services on the Geohazards Exploitation Platform for Copernicus Sentinel-1 Surface Motion Mapping. Remote Sensing 14(23), 6075. https://doi.org/10.3390/rs14236075

Gehlot, S., & Hanssen, R. F., 2008. Monitoring and Interpretation of Urban Land Subsidence Using Radar Interferometric Time Series and Multi-Source GIS Database, in: Nayak, S., & Zlatanova, S. (Eds.), Remote Sensing and GIS Technologies for Monitoring and Prediction of Disasters, 137–148. https://doi.org/10.1007/978-3-540-79259-8_8

Kalaitzis, P., Foumelis, M., Mouratidis, A., Kavroudakis, D., & Soulakellis, N., 2024. Multiscale Visualization of Surface Motion Point Measurements Associated with Persistent Scatterer Interferometry. ISPRS International Journal of Geo-Information 13(7). https://doi.org/10.3390/ijgi13070236

Kalaitzis, P., Foumelis, M., Vasilakos, C., Mouratidis, A., & Soulakellis, N., 2023. Interactive Web Mapping Applications for 2D and 3D Geo-Visualization of Persistent Scatterer Interferometry SAR Data. ISPRS International Journal of Geo-Information 12(2), 54. https://doi.org/10.3390/ijgi12020054

Kraak, M.-J., & Ormeling, F., 2020. Cartography: visualization of geospatial data. CRC Press.

Poncoş, V., Stanciu, I., Teleagă, D., Maţenco, L., Bozsó, I., Szakács, A., Birtas, D., Toma, Ş.-A., Stănică, A., & Rădulescu, V., 2022. An Integrated Platform for Ground-Motion Mapping, Local to Regional Scale; Examples from SE Europe. Remote Sensing 14(4), 1046. https://doi.org/10.3390/rs14041046

17th INTERNATIONAL CONGRESS
of the Geological Society of Greece

BULLETIN OF THE GEOLOGICAL SOCIETY OF GREECE, SP. PUBL.

EXTENDED ABSTRACT 125

Methodology of cave mapping: comparison of surveys

Kalogeropoulos I.[1], Lazaridis G.[2,*], Tsekoura A.[1]
(1) Hellenic Speleological Society, branch of northern Greece
*(2) Faculty of Sciences, Aristotle University of Thessaloniki (AUTH), 54124 Thessaloniki, Greece, *geolaz@geo.auth.gr*

Research Highlights

The aim of the present article is to investigate the factors that affect the cave mapping. This investigation is based on comparisons of topographical diagrams of a given space made by different surveys of the same stations. A classroom of a known topography has been used for that purpose. The used traverses are the circumference survey, splay shots, zig-zagging survey and radial survey (after Dasher 1994). The comparisons concern the shape, the area and the direction of the cave map as well as the time that is needed for the survey and the affect of errors in certain station to the general topography of a map. The results are summarized and the significance of reference in the used methodology in any cave surveying is concluded. Among the different traverses the radial one and the splay shots are considered as the most accurate.

Introduction to Cave Mapping

Cave mapping is a crucial aspect of speleology. Due to the complex nature of caves, the perception of distances often does not align with reality. A well-drawn map allows speleologists to assess the cave's size, identify hazardous areas, anticipate challenges during exploration, and determine the necessary equipment. Furthermore, the systematic study of caves requires detailed and reliable mapping in a suitable format and scale, addressing various geoscience disciplines such as geology, speleology, and paleontology (Pagounis et al., 2004; Doggouris et al., 1986). Cave mapping is complicated by numerous factors, the two most prominent being the non-ideal conditions explorers face due to the challenging environment (Doggouris et al., 1986), which makes the mapping process arduous, and the cave's inherent complexity. This often requires documenting points located at vastly different elevations, necessitating a comprehensive representation of a three-dimensional space.

The first stage of cave mapping involves collecting data to create the map, which includes measurements taken by a mapping team. Ideally, this team consists of 3-4 members to optimize time, particularly in large caves, though a two-person team often exhibits better coordination (Judson, 1974). The team leader determines the locations of the measurement stations, records data in a logbook, sketches the cave, and typically designs the map, as they are most familiar with the notes. The other team members operate the instruments and relay measurements to the leader (Savvaidis et al., 2007).

The mapping process begins by establishing a station (which may or may not have pre-defined coordinates relative to a reference system). Subsequent stations are positioned to accurately depict the cave's shape. For each new station, the distance from the previous one, the azimuth, and the elevation difference (or slope) are measured and recorded. With these data, the stations can be drawn to scale and oriented on paper. This process is repeated as needed for all required stations.

The measurements collected form a path within the cave, known as a traverse, which can be either open or closed. In a closed traverse, the start and end points coincide, while in an open traverse, they do not. Closed traverses provide greater accuracy in mapping, as they allow the mapper to detect potential errors (Dasher, 1994). There are four types of traverses: central, radial, circular, and zig-zag, each suited to different cave shapes and sizes.

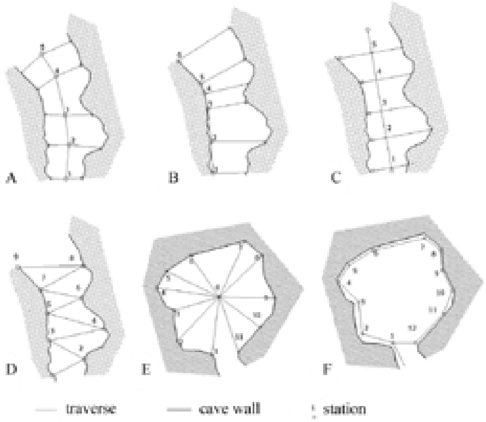

Figure 1. Illustrates various types of traverses: (a) central traverse, (b) central traverse with the main line along the wall, (c) central traverse with vertical measurements from the main line, (d) zig-zag traverse, (e) radial traverse, and (f) circular traverse.

- In a central traverse, a central line of stations is established down the middle of the cave passage, and the distance to the cave walls is measured from each station on both sides (Judson, 1974). Lateral measurements always include azimuth readings (Fig. 1a). When the cave's morphology permits, the central line can run along one wall, with measurements taken only toward that wall (Dasher, 1994; Fig. 1b). In some cases, a straight central line is used, and wall distances are measured perpendicular to this line without needing azimuth readings (Fig. 1c; Savvaidis et al., 2007).

- In a zig-zag traverse, measurements alternate between the left and right sides of a narrow passage, creating a zig-zag path (Fig. 1d). This method provides more detail about each cave wall. Some explorers believe this technique distorts the cave's length, but it offers more comprehensive information for the final map (Dasher, 1994).
- In a radial traverse, measurements are taken from a central station (usually in a chamber) toward the boundaries of the area being mapped. The subsequent stations are radially arranged around the central station. This method is ideal for chambers that are roughly circular, allowing a clear line of sight from all stations to the center (Fig. 1e).
- In a circular traverse, measurements follow the perimeter of the mapped area. In this case, the traverse's shape matches that of the mapped space (Fig. 1f). This method is commonly used in circular chambers, where completing the traverse by taking measurements from the last station back to the first helps identify potential errors during map creation (Dasher, 1994).

Mapping Instruments

The primary instruments used in cave mapping are tape measures and laser meters for distance measurement, compasses for azimuth readings, and clinometers for slope measurements (Tarsoly, 2006).

Tape measures are the standard tool for direct distance measurement. They are made from various materials (metal, plastic, linen, or plastic) and typically come in lengths of 20, 25, 30, and 50 meters. Their accuracy is approximately 2-3 cm per 100 meters under standard tension (marked on the tape) and at 20°C. Proper care should be taken when rewinding the tape into its case, as mud and dirt in caves can jam the tape, rendering it unusable (Savvaidis et al., 2007).

Laser meters, which use electromagnetic waves to measure distance, are particularly useful in large caves. Many laser meters can also measure slope (Doggouris et al., 1986).

For angle measurements, a magnetic compass is used to measure the azimuth, or the angle between the target and magnetic north, which differs from true north. Compasses can be divided in several ways, with the most common being a 0–360° system providing a clockwise azimuth relative to north. Other systems include quadrant-based systems, military mils (6400 divisions), and grads (400 divisions) (Dasher, 1994). More precise angle measurements can be made using theodolites or total stations, though their size can make them cumbersome in caves. 3D scanners, which capture real-time three-dimensional coordinates to generate a 3D model, are another tool used in cave mapping (Pagounis et al., 2004).

A clinometer measures ground slope to calculate elevation differences. Simple clinometers consist of a protractor and a plumb line and can sometimes be integrated with a compass. Geometrical leveling is another method for measuring elevations, though it is difficult to apply in steep environments (Doggouris et al., 1986).

Error Correction and Map Drawing

After data collection, the next step is to correct for measurement errors (Tarsoly, 2006). Errors during mapping can distort the final result, deviating from reality. These errors fall into several categories:

- **Random errors**, such as deviations from a straight line, horizontal position, or recording inaccuracies (Savvaidis et al., 2007).
- **Systematic errors** caused by instrument imperfections, differences from the standard, or incorrect tension applied to the tape measure. Tape sag due to weight is another common source of error. Calibrating the instruments outside the cave to account for these errors is a recommended procedure (Savvaidis et al., 2007).
- **Blunders**, the most critical type of error, arise from human factors such as inexperience or extreme fatigue, making them unpredictable.

The final stage of mapping is creating the map based on the corrected measurements. It is crucial that the cave map is aligned with the country's triangulation network (or other reference systems) (Tarsoly, 2006).

Different mapping techniques can yield slightly varied results for the same cave. This study examines the case of mapping a specific space while keeping parameters like stations, team composition, and instruments constant but varying the traverse technique.

Mapping of a Room with Different Survey Routes

To compare different mapping techniques, a room and its antechamber from the Department of Geology at Aristotle University of Thessaloniki (AUTH) were selected for mapping. This choice was made because the shape of the space was already known, and a topographic plan existed, allowing for a comparison of each route's results with the topographic model (Fig. 2).

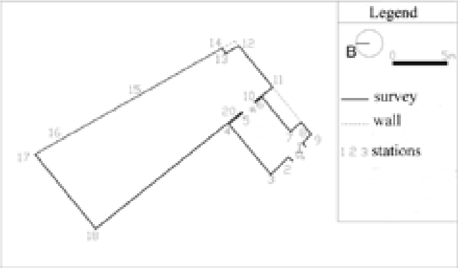

Figure 2. Topographic plan of the chamber mapped in this study, showing the locations and numbering of the stations used.

Instruments Used and Stations

The instruments used included a laser meter, a measuring tape, and a Suunto compass with a clinometer. A total of 21 stations were defined, remaining the same for each survey route to ensure accurate comparison of results, even in specific points. Additionally, on the eastern side, stations 15 and 16 were marked along with stations 14 and 17 to examine the deformation caused by redundant stations.

It was noted that the length of each measurement should be as large as possible to limit the number of stations, as suggested by Judson (1974).

Different Mapping Routes

The mapping was repeated, keeping the same instruments and team composition, but changing the route. The routes used were:

1. Radial route: Measurements were taken from three central stations (0, 21, 19).
2. Circular and zigzag routes: Mapping started from station 1, located at the entrance of the antechamber.
3. Central route: Measurements were taken perpendicularly from two central lines (19-21 and 21-22) toward the walls.

After collecting the data, four different maps of the same area were produced without any error correction (Fig. 3).

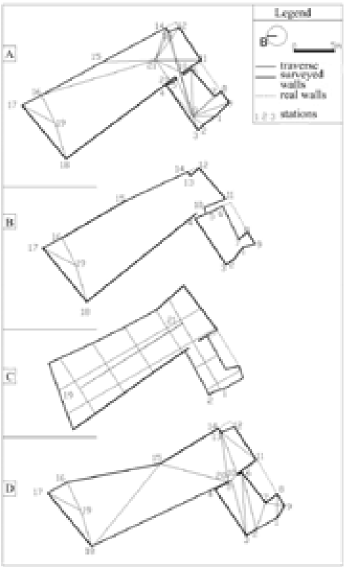

Figure 3. Topographic diagrams in "speleological style" of the chamber with different traverses: a) radial traverse, b) circular traverse, c) central traverse, d) zigzag traverse.

Discussion and conlusions

Radial Route Map (Fig. 3a, Table 1): This map closely aligns with the topographic plan of the room. The measured area matches the actual size (171 m²). Points 15, 16, and 17 are on the same straight line, with only minor deformations in some spots, such as the turn of the antechamber, which do not affect the overall shape of the room.

Circular Route Map (Fig. 3b, Table 1): This map shows deformation compared to the room's topographic plan, affecting the calculated area, which is smaller than the actual size by 7 m². Significant deformations were observed at the corners, which influence the overall shape. However, the advantage of the circular route is that there is a direct relationship between the measurement and the area represented.

Central Route Map (Fig. 3c, Table 1): This map presents minor deformations and a good overall correlation with the topographic plan. The measured area deviates slightly from the actual size (by 3 m²), with stations 15, 16, and 17 aligning correctly. The corners are also accurate. The central route, especially when measurements are taken at right angles, yields very good results but is time-consuming (Savvaidis et al., 2007).

Zigzag Route Map (Fig. 3d, Table 1): This map exhibits significant deformation compared to the actual shape. A notable discrepancy was found in the length of the room, which is a known issue with this route (Dasher, 1994). This also affects the area, which is calculated larger than the actual size by 15 m². Additionally, a slight shift in the map's orientation relative to the north was observed. Although the zigzag route requires less time for measurements compared to other routes, a single error can greatly distort the overall shape of the map and, with it, many important data points such as area and length.

Table 1. Summary description of the results of each traverse and evaluation regarding the main characteristics of cave mapping.

Type of Traverse	**Radial**	**Circular**	**Central**	**Zigzag**	**Type of Traverse**
Deformation	Minimal	Considerable	Minimal	Considerable	Deformation
Area Accuracy	Very good	Shows deviation	Relatively good	Shows significant deviation	Area Accuracy
Retention of Straight Lines	Yes	Yes	Yes	No	Retention of Straight Lines
Effect of an Error on Subsequent Measurements	Small to minimal	Significant	Small to minimal	Very large	Effect of an Error on Subsequent Measurements
Mapping Speed	Fast	Fast	Time-consuming process*	Fast	Mapping Speed
Deviation from Actual Orientation	No	No	No	Slight angle	Deviation from Actual Orientation

Dermitzakis & Dikaioulia (1981) emphasize the importance of a unified methodology in cave mapping. This study highlights the significance of:

a) the chosen survey route (Table 1),
b) the number of stations, and
c) the location of those stations in the mapping process.

As a result, maps produced using different methodologies are not directly comparable. Although references to the specific mapping methodology used are rarely found in the literature, it is deemed essential that each map be accompanied by these details for clarity and accuracy.

Acknowledgements

This paper was originally presented in Greek at the 4th Pancretan Speleological Conference in 2008, held in Zoniana, Crete, Greece. It is resubmitted with the approval of the organizing committee, represented by biologist Kaloust Paragamian, head of the Hellenic Institute of Speleological Research.

References

Dasher, G.R., 1994. ON STATION - A complete handbook for surveying and mapping caves. National Speleological Society, pp. 1-242, USA.

Dermitzakis, M.D., Georgiadou-Dikaioulia, E., 1981. Methods for calculating and measuring cave development parameters. Bulletin of the Hellenic Speleological Society, 18: 391-410.

Doggouris, S.N., Makris, G.N., Balodimos, D.D., 1986. Cave surveys. Proceedings of the Conference on Modern Methods of Surveying and Documenting Monuments and Archaeological Sites, pp. 188-221.

Judson, D., 1974. Cave survey for expeditions, The Geographical Journal, 140(2): 292-300.

Pagounis, V., Kalykakis, S., Biza, P., Papadopoulos, CH., 2004. The use of 3D scanning as a methodology for cave mapping: Application to the St. George Cave in Kilkis. Proceedings of the 10th International Conference, Bulletin of the Hellenic Geological Society, 36: 1244-1251.

Savvaidis, P., Yfantis, I., Lakakis, K., 2007. Topography and thematic cartography. Lecture Notes - Department of Architecture, Aristotle University of Thessaloniki.

Tarsoly, P., 2006. Cave Information System. Shaping the shape. XXIII FIG Congress, GIS Applications - Special Issues, pp. 1-9, Munich.

17th INTERNATIONAL CONGRESS
of the Geological Society of Greece

BULLETIN OF THE GEOLOGICAL SOCIETY OF GREECE, SP. PUBL.

EXTENDED ABSTRACT 126

Geoeducational and Geotourism values of geological resources as novel path for Geosciences Education

Kalpogiannaki M.[1], Rogkala A.[2], Giannakopoulou P.P.[2], Koutsovitis P.[2], Lampropoulou, P.[2] Petrounias P.[2], Papoulis D. [2], Koukouzas N.C.[3], Pomonis P.[1]

(1) Section of Mineralogy and Petrology, Department of Geology and Geoenvironment, National and Kapodistrian University of Athens, Panepistimioupolis Zografou, 157 84 Athens, Greece, maria.kalpogiannaki@gmail.com (2) Department of Geology, University of Patras, Patras, Greece, (3) Chemical Process and Energy Resources Institute, Centre for Research and Technology Hellas (CERTH), Greece

Introduction

The modern trends of nowadays force us to adapt more and more to them in order to achieve the European as well as the international goals of smooth and sustainable development. Specifically, the evolution of data in Greece reveals that we are increasingly moving towards a new model of overtourism, where, in addition to the increase of revenue from an economic perspective, we must also identify any other ways to use these visitors from the geosciences viewpoint. This will indirectly help us to create a more conscientious audience capable of receiving any additional information regarding environmental protection in a more fruitful manner.

The only way to balance the strong relationship between human and nature is the sustainable development as it will solve problems between the increasing demands for resources and the environment. Living in a world where the climate change is increasingly apparent, the risk of depletion of mineral resources as well as the environmental pollution is becoming our daily routine, it is imperative as geo-scientists to reconsider our views and our actions in order to promote a more sustainable development model for a more sustainable society. Nowadays, the general public awareness of daily environmental challenges and sustainable development is low. Young people are by nature receptive to learn, while at the same time, they are also the key drivers of change in a society. In order to play a such role, they need to become environmentally aware. In this way, they could devise action programs to solve problems as they considered as active citizens and also exploited their relationship with all social media. Environmental education and geo-education, "which is promoted as the new educational trend that will make learning more comprehensive, more effective, more conscious and based on the research-scientific method of collecting, processing, presenting and utilizing information" will contribute to addressing this necessity. Thus, the purpose of knowledge of the environment is not the domination of man over nature but, in the context of the total environment, the relation of competition and domination are transformed into relations of complicity, cooperation and creation, where man must lead and follow the nature (Zouros *et al.*, 2004). In fact, at the 1977 International Conference in Tbilisi, Georgia, participants agreed that environmental education should be regarded as a separate scientific field of crucial significance. It is worth mentioning that UNESCO never gave up on the concept and initiative of environmental education. Following the above philosophy, UNESCO started to demarcate some areas with important geocultural monuments and designate them as UNESCO geoparks after strict geotope parameter controls (Iliopoulos *et al.*, 2024).

Geoturism has created techniques for geoeducation that enable geo-interpretation and the attainment of cognitive objectives by the audience, i.e., a broad education in geology, in order to promote awareness of geoheritage values, mainly in geoparks and geosites (and in Greece, in legal forms of protection – reserves of geoheritage and documentation sites or monuments of geoheritage).

This study aims to investigate the perception and the cognitive level of Tourists in Kefalonia Island (Greece) as one of the famous Geoparks in Europe. To achieve the main objective of improving the knowledge about geosites, mineral raw materials, and geological heritage, a targeted public outreach took place based in a hotel in Argostoli (Kefalonia) within one of designated UNESCO Geoparks focusing on teaching and rapid learning about the basic principles of geoeducation, when at the same time is giving emphasis in the importance of sustainable environmental practices about the mineral raw materials by increasing geoethical awareness and education. Through this type of study, it is possible to identify immediately and interactively the cognitive gaps for a better and sustainable society.

Geological setting of studied area

Kefalonia Island, one of the biggest Ionian Islands, is mainly separated through alpine formations (Paxoi and Ionian geotectonic units) and Plio–Quaternary sediments (Underhill 1989, Lekkas *et al.*, 2001). The Paxoi unit composed of Triassic–Middle Miocene carbonates and clay-clastic sequence of flysch from the Middle Miocene–Early Pliocene, including alternations of marls, clays and mudstones, while the Ionia unit composed of Triassic evaporitic series and Jurassic–Cretaceous limestones and slates (Lekkas *et al.*, 2001). Pliocene–Calabrian and Middle-Upper Pleistocene–Holocene series make up the Plio–Quaternary sediments, which characterized through the presence of a marine sequence, yellowish marls with siltstones, sandstones, sands and coarse calcarenites. Pliocene–Calabrian series prevail in the Lixouri area, where the marine sequence is observed as an uplifted coastal zone with 2 to 10 km width range. Such formations have a thickness variation between 200 and 500 m and are developed transgressively over Paxoi unit (Figure 1) (Lekkas *et al.*, 2001).

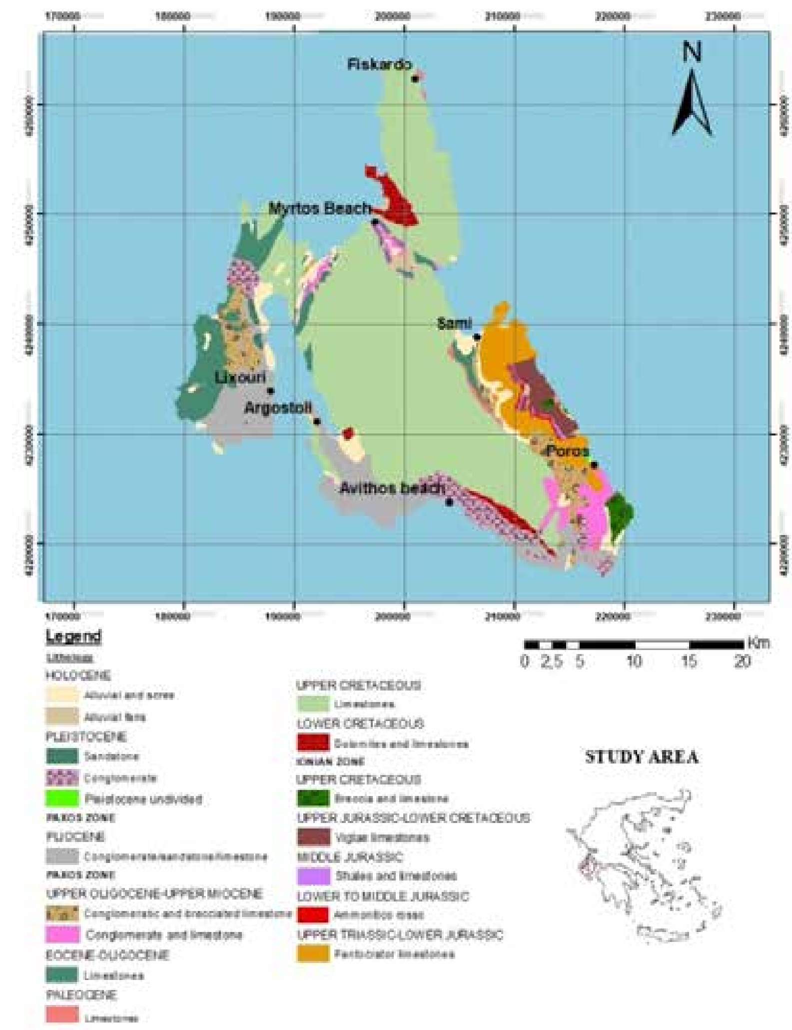

Figure 1. Geological map of Kefalonia (after IGME) (Lampropoulou *et al.*, 2023).

Analytical methods

In order to investigate how informed the European citizens about Geosites, geology, petrology and raw materials issues are, as well as whether they agree with the necessity of geoeducation to the general public, a number of questions accompanied by a geological map were given to a variety of European citizens. For this reason, a random sample of visitors was selected from May 25 to June 25, 2024, which is a peak period, and 300 European citizens coming from various European countries were selected in order to obtain a representative statistical sample. The questions were given in visitors of a hotel located in Kefalonia Island, which constitutes one of the most famous European tourist destinations and now has air connection with almost all European countries. Moreover, this hotel was chosen as it contains a geological stand which has a display case of rocks of various types and provides explanatory information about each one as well as at the reception the employees are geology graduates. The island of Kefalonia was strategically chosen, as in 2021, it was included in the UNESCO Geoparks, as a result of which it attracts many European citizens who visit the island to discover the natural beauty of the geopark. All the answers were statistically analyzed in order to draw important conclusions.

Questionnaire

In order to investigate how informed European citizens are about geoparks and more specifically about the Kefalonia-Ithaca Geopark, a series of questions were given in a preliminary survey stage to 300 European citizens/visitors in order to obtain a representative statistical sample. The design of the questionnaire was based on determining the elements necessary for the research and then the questions were screened and the most representative ones were selected, following all European standards. The questionnaires were distributed/given to the partner hotel from 25 May to 25 June of 2024 and at this point the questionnaires were purely diagnostic in nature and statistically analyzed in order to draw significant conclusions. In the context of this study, we present a part of the overall questionnaire that was given to the guests of the hotel as well as the wider research that was conducted.

Below, the questions used in the questionnaire are listed:

1. What is your academic backround?
2. Have you visited another Geopark or Geo-invastigation in the current/last year? (yes, no)
3. Do you have any special interests about geosciences as a subject at school?
4. Have you ever encountered the term geotourism? (yes, no)
5. What do you think about the mineral raw materials in our life, are they very important? (yes, no)
6. Do you think geoheritage sites (specific rocks, caves as Melisani Lake) can be an important tourist attraction? (yes, no)
7. Does the school, universities, or public teams, organize field trips or lessons in your country/ region to the geoheritage sites? (yes, no)

At this point, representative Geologist in collaboration with the hotel's reception service informed and educated the tourists about the concept of Geopark and the geology of Kefalonia island, while they also guided them how to navigate in the geopark so they could better understand the geological history of the area. Actually, through this way, we pursued to achieve the reconnection of human society, at all levels, with the planet known as home. However, extremely important was to make them understand and also to accept that our planet and its 4,600 million of years history have shaped every aspect of our lives and our societies. As a result, the aim was to strengthen the feeling of respect of the environment and the preservation of this natural heritage.

The way to achieve what was mentioned above was to organize short trips through the georoutes map of the geopark (Figure 2). Along with the selected and suggested geo-routes for exploration, all the necessary instructions and information relative to what they were going to visit was given to the guests. The aim of this step was the tourists to see in depth the geological history reflected in each geosite and to become a part of the history and geological processes.

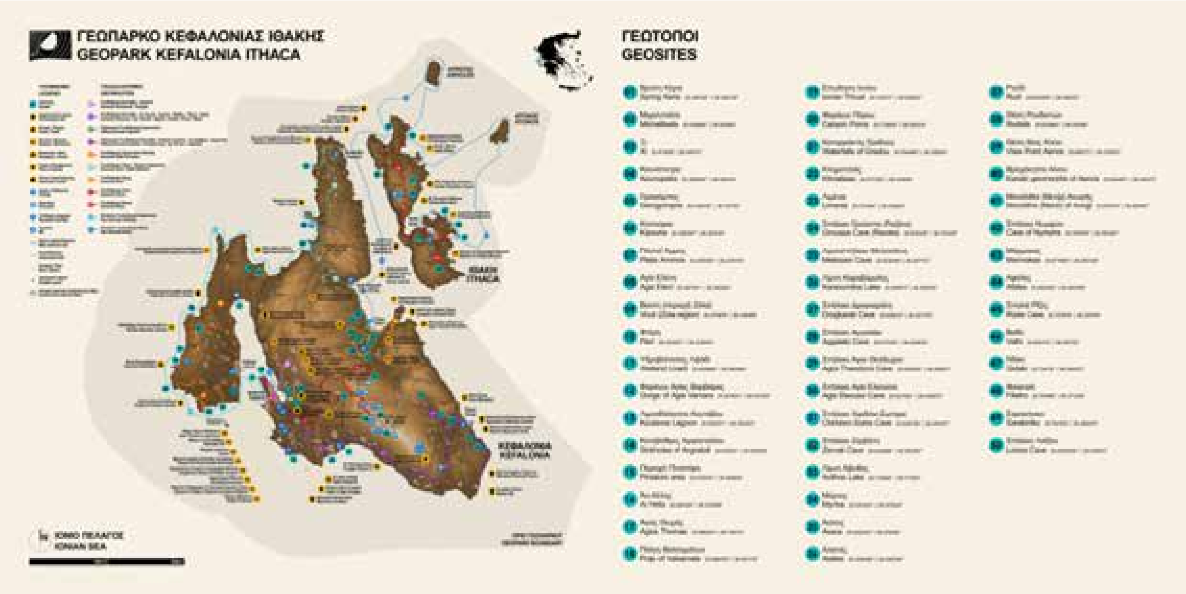

Figure 2. Map of the Geopark of Kefalonia Ithaka

Statistical analysis

Statistical interpretation of the results (tourist's answers) was performed with SPSS statistical analysis in order to investigate the interdependence of the questions. The methodological approach of the process of the present study has been directed to the area of the quantitative research approach to collect and analyse the research data. The study focuses on the quantification of collected data and on the interpretation of the results.

Results and Discussion

A total of 300 questionnaires were filled out. The age of those which were filled out the questionnaires was from 18 to 75 years old, while the 55% of the respondents were men. Based on the questionnaire survey conducted in collaboration with a geo-friendly hotel in Kefalonia, on a representative sample of 300 people in low-stress conditions for respondents and in a beautiful and natural environment, important points that should be considered in any future research or in a pilot work were identified, while at the same time, concerning the issue of geoeducation in general public. More specifically, the following results indicate that even a large amount of the respondents had heard about the geotourism, they have been trained in a substantial and in-depth way on the subject.

While the majority of respondents has finished high school and they have subsequent activities or studies, as shown by the answers of the first question, it does not seem that they have been substantially educated on geoeducation issues and natural resources protection (questions 5 & 7). Particularly important seem to be the results of questions 2, 3 and 4. Even the general public has visited a geopark or a geotope in the past, the 91% may not be able to understand the concept of a geotope as a geological unit of increased and timeless value.

On the other hand, the answers of question 3, 4 and 6 reveal the potential interest that the general public seems to have in geoeducation as long as they are aware of it and have been guided on this knowledge, which makes geosciences education from the young people possible to be a key focus. Finally, the results of questions 5 and 7 clearly indicate that there is a clear gap in the education (answers of question 7) regarding the use and the importance of mineral raw materials due to the absence of a strategic and common public awareness of geoeducation in all countries. Electrical and electronic devices such as mobile phones, computers, TV are made by a large amount of mineral raw materials (i.e. minerals, metals).

Table 1. Statistical results of the respondents.

1 Question	Primary school 15%	Secondary school 65%	Master degree 18%	PhD 2%
2 Question	YES 9%	NO 91%		
3 Question	YES 74%	NO 26%		
4 Question	YES 90%	NO 10%		
5 Question	YES 56%	NO 44%		
6 Question	YES 93%	NO 7%		
7 Question	YES 23%	NO 77%		

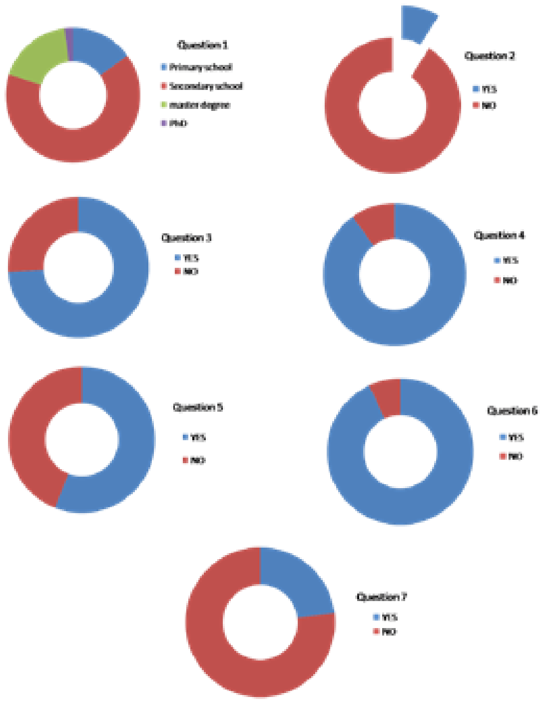

Figure 3. Excel pie charts showing the answers from the questionnaires (answers to questions 1 to 7).

Conclusions

The conclusions of this study seem to be double. The first one is related to the poor knowledge about the mineral raw materials, geo-investigations and Geoparks, while the second is related to the social acceptance of Geoeducation.

The main conclusions of the study are summarized below:

- Geosites play significant role in geoeducation even they have not always been used properly often due to lack of knowledge.
- Schools play a crucial role in the development of geoeducation and geotourism, as cognitive needs are formed.
- The majority of the respondents consider that geotourism constitutes an important tourist activity.
- It should be mentioned that there should be an organized project in all European countries in order to communicate the scientific knowledge to a wider European audience, with having as an ultimate goal the consolidation of sustainable development in Europe.

References

Zouros, N. The European Geoparks Network. Episodes 2004, 27, 165–171.

Underhill, J.R., 1989. Late Cenozoic deformation of the Hellenide foreland, western Greece. GSA Bull. 101, 613–634.

Lekkas, E., Danamos, G., Mavrikas, G., 2001. Geological Structure and Evolution of Kefallonia and Ithaki islands. Bulletin of Geological Society of Greece 34, 11–17.

Iliopoulos, G., Golfinopoulos, V., Kalampalika, A., Karanika, K., Kolendrianou, M., Papadopoulou, P., Tsacos, S., Tzortzi, M., Valavani, D., Zoumpouli, E., Bourli, N., Zelilidis, A., 2024. From the Ground to the Public: Old and New Fossil Discoveries from Kefalonia–Ithaca UNESCO Global Geopark and Their Value in Research, Education, and Local Palaeontological Heritage. Sustainability 16(6), 2521.

Lampropoulou, P., Petrounias, P., Rogkala, A., Giannakopoulou, P.P., Gianni, E., Mantzoukas, S., Lagogiannis, I., Koukouzas, N., Hatziantoniou, S., Papoulis, D., 2023. Microstructural and Microbiological Properties of Peloids and Clay Materials from Lixouri (Kefalonia Island, Greece) Used in Pelotherapy. Applied Sciences 13(9), 5772.

17th INTERNATIONAL CONGRESS of the Geological Society of Greece

BULLETIN OF THE GEOLOGICAL SOCIETY OF GREECE, SP. PUBL.

EXTENDED ABSTRACT 127

The pseudokarst at the Kaki Thalassa Bay reveals unknown ancient mining activities (Lavreotiki UNESCO Global Geopark)

Kampolis I.[1,3], Voudouris P.[2], Moraiti E.[1]

(1) Lavreotiki UNESCO Global Geopark, Lavrion, Greece, kampolisigeo@gmail.com (2) National and Kapodistrian University of Athens, Zografou, Greece (3) National Technical University of Athens, Zografou, Greece

Research Highlights

Pseudokarst features at the small islet of Kaki Thalassa, reveal previously unknown ancient mining activities.

The Lavreotiki UNESCO Global Geopark comprises one of the nine Greek UNESCO Geoparks, promoting the significant geological heritage of Greece. It is the only geopark located close to Athens, the capital city of Greece and bears a long and rich mining history. Lavreotiki Geopark occupies the southeastern part of the Attica Prefecture and its spatial extent coincides with the region of the Lavreotiki Municipality. Although, mining heritage represents the core of the Lavreotiki Geopark, other geological features such as coastal, geomorphological landforms enclose high scientific and educational value, revealing unknown aspects of this deep-in-time heritage.

The Lavrion mining district covers an area of >100 km^2 and has been exploited nearly continuously for silver (Ag) and lead (Pb) from 4000 BC until the late Roman times (Conophagos, 1980; Rosenthal *et al*., 2012). It is also considered that Lavrion was a source of copper (Cu) for a large part of the latter period (Gale *et al*., 2009; Kayafa, 2020). Monumental sites and structures such as the Industrial District, as well as the Thorikos theater at the flanks of the Velatouri hill, reveal the inseparable connection of the ancient local people with their peculiar local geology. This type of geology provided the appropriate resources to the Athenian Democratic Polis to be transformed during the Classical period and fund the trireme fleet, which determined the naval battle at Salamis against the Persians.

Apart from this mining wealth, the Lavreotiki Geopark includes a 73-km long coastline, hosting a rich geodiversity and biodiversity. With the aim of assessing the impact of the future sea level rise on the coastal landforms, which can also be potential future geosites, the geopark's personnel undertook an extended project between 2022-2024 for surveying and mapping the geological/geomorphological sites on the coastline. During these activities at the Kaki Thalassa Bay (Keratea, Lavrion), a small rocky islet was surveyed (Fig. 1). This islet consisting of Pounta marble, is located 128 m from the closest coast and hosts two strange pool-like structures at its eastern side (Fig. 2).

These morphological structures were considered to be the result of natural processes and were often referred as natural pools. On the contrary, detailed geomorphological mapping with the application of drone-assisted technology and S-f-M (Structure-from-Motion) technique in combination to geological observations, resulted in anthropogenic pseudokarst features in the sense of Veress (2022).

The assessment of the origin of these pools was implemented with the use of sophisticated, low-cost, non-destructive photogrammetrical technique, employing two-dimensional (2D) aerial mapping and geological-geomorphological field-based observations. The same technology has been applied in other locations of the geopark (Kampolis *et al*., 2024) as well as in other sites of interest (Kampolis *et al*., 2021) with valuable results.

Figure 1. The small islet close to the northern coast of the Kaki Thalassa Bay.

Figure 2. Aerial photo of the two pool-like structures at the islet. The red dashed line represents the fault crossing the western part of the islet.

The followed methodology was arranged in two separate phases. The first phase included the aerial 2D mapping and the photogrammetry of the small islet and the second one comprised the in-situ geological and geomorphological observations, as well as the extraction of samples for subsequent analysis.

During the first phase of the project, a *DJI Mavic Air 2* drone was employed for the 2D mapping of the islet, after setting up its flight mission within the *Copterus* app, running on an "*iphone 13 mini*" mobile phone. The drone's flight was programmed at an altitude of 30 m with a 75% frontal and lateral overlap, yielding a total (real) flight duration of 13 min. The collected aerial photos were then inserted in *Agisoft Photoscan Pro* software and following the photogrammetrical work-flow without ground control points, the three-dimensional (3D) reconstruction of the small islet was generated (Fig. 3). The Agisoft work-flow includes certain stages of multi-image processing: A) photos alignment, B) point cloud building, C) mesh reconstruction and D) Digital Elevation Model (DEM) generation (Semaan and Salama, 2019). For the in-depth exploitation of the islet's 3D reconstruction, the exported mesh file from Agisoft was input in *CloudCompare* software and converted into a point cloud for further geometric measurements. The latter enables various measurements such as inclinations, azimuths, lengths, areas and geometrical features of plane surfaces (dip and dip direction) on certain features.

The second phase consisted of the mineralogical observations on mineral assemblies found on the perimetry of these pool-like structures. Also, geomorphological observations on the morphology of the pools took place in-situ. The depths of their bottom were measured with a SUUNTO D3 digital depth gauge (accuracy ±0.1 m).

The generated 3D model of the small islet in combination to the field-based geomorphological measurements, provided the ability to assess the formation origin of the pools, present at the eastern side of it. According to the geomorphology of the coastal part of the islet and the bathymetry of the pools' bottom, it is unlikely for the pools to be the result of natural erosional processes. This can be supported by the bathymetry of the connection passage between the open sea and the easter pool (Fig. 4). The depth at this point reaches only 0.3 m and thus prevents the wave activity and its subsequent erosive force to enter the eastern and western pool and form them, as the erosive force is consumed on the shallow coastal part. Additionally, the eastern pool reaches a depth of 2.5 m, which cannot be justified by natural processes (i.e. waves, karstification).

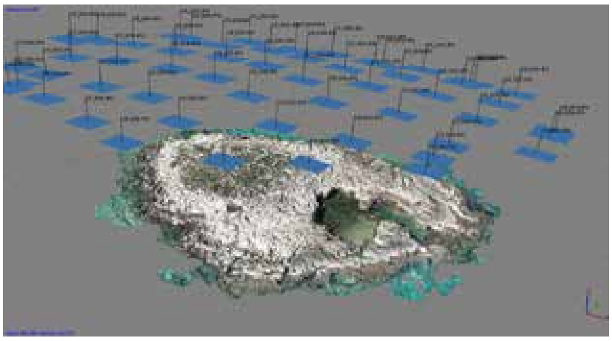

Figure 3. The 3D model of the small islet and the acquired aerial photos during the flight mission of the 2D mapping.

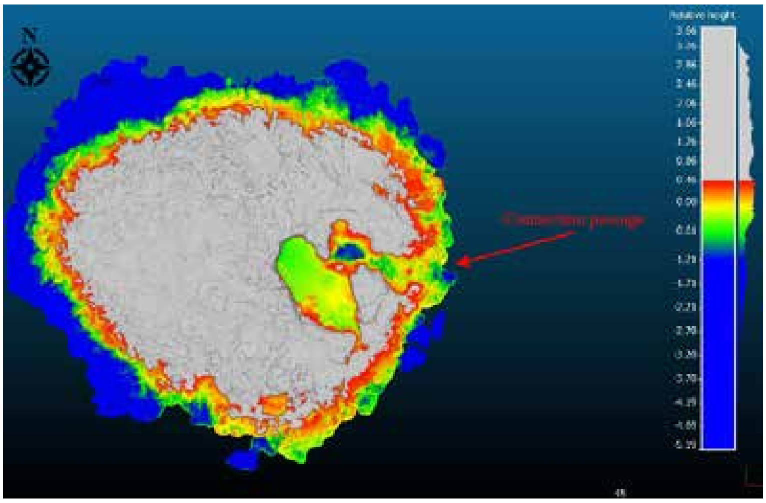

Figure 4. The bathymetry of the coastal part of the islet, generated in the CloudCompare software. The colored scale on the right provides the depth.

Moreover, the presence of a tectonic structure trending NW-SE (15°/204° – Dip/DipDir) and crossing the western part of the islet (Fig. 2) may be an extension structure related to the Miocene low-angle detachment fault developed during the top-to-SSW crustal extension, resulting in the Western Cycladic Detachment System (Loisl *et al.,* 2014), and locally referred as the South Attic Detachment (SAD) (Ross *et al*., 2021). This fault seems to play a role on the presence of sulfide mineralization (now oxidized to iron oxides), recorded on the periphery of the pools and along its surface (Fig. 5). The oxidized mineralization occurs above the SAD, where it replaces, and also cements brecciated fragments of the Punta marble. Ross *et al.* (2021) mentioned that normal faults rooted within the SAD are linked to its movement and have hydrothermally affected the Pounta marble. Consequently, it is possible that this NW-SE fault has designated the oxidized sulfide mineralization on the Pounta marble of the islet, which also attracted the interest of the ancient people. The latter must have started exploiting this mineralization, leaving open depressions that were later inundated by the sea level rise since the antiquity. Ancient miners extracted the mineralized layer, and this is probably the reason for the flat, shallow bottom of the western pool. The pool was excavated for the extraction of the mineralization, whereas natural processes like karstification would have resulted in a more uneven bottom. Therefore, these depressions originated by the anthropogenic activity on the carbonate rock of the islet, can be falsely interpreted as karst landforms and thus, represent the so-called anthropogenic pseudokarst. The nature of the latter revealed these previously unidentified ancient mining works.

Figure 5. The oxidized sulfide mineralization on the eastern side of the eastern pool.

Acknowledgements

Warm thanks are addressed to DANETAL S.A. for the support on the research activities of the Lavreotiki UNESCO Global Geopark.

References

Conophagos, C. E., 1980. Le Laurium antique et la technique grecque de la production de l'argent, Ekdotiki Athinon.

Gale, N. H., Kayafa, M., Stos-Gale, Z. A., 2009. Further evidence for Bronze Age production of copper from ores in the Lavrion ore district, Attica, Greece, in: A. Giumlia-Mair et al. (Eds.), Proceedings of the Second International Conference: Archaeometallurgy in Europe, 158–176.

Kampolis, I., Iossifidis, Th., Moraiti, E., 2024. The 3D reconstruction of an ancient quay at the Thorikos Bay (Lavreotiki UNESCO Global Geopark). International Conference "Widening the Big Blue Horizon" Innovative Technologies & Sustainable Strategies for the Protection and Management of Underwater Cultural Heritage, Volos, Greece, p. 50.

Kampolis, I., Dimakopoulou, A., Vakalas, I., Loukidis, N., Dimitriadis, Kl., 2021. Geotechnical study of the ancient Phyle Fort. Directorate of Restoration of Ancient Monuments, Ministry of Culture.

Kayafa, M., 2020. The metal resources of Laurion during the Early Bronze Age: A synthesis of the archaeological and archaeometric data, in: Papadimitriou, N., Wright, J., Fachard, S., Polychronakou- Sgouritsa, N., Andrikou E. (Eds.), Athens and Attica in prehistory, 193-201.

Loisl, J., Linder, K., Huet, B., Graseman, B., Rice, N.H.N., Soukis, K., Schneider, D., 2014. The Western Cycladic Detachment System on Makronisos, Greece, EGU General Assembly, Vol. 16, EGU2014-11587.

Rosenthal, P., Morin, D., Herbach, R., Photiades, A., Delpech, S., Jacquemot, D., Fadin, L., 2012. Mining technologies at deep level in antiquity: The Laurion mines (Attica, Greece). Second Mining in European History Conference of the FZ HiMAT, Innsbruck, Austria, pp. 89–95.

Ross, J., Voudouris, P., Melfos, V., Vaxevanopoulos, M., Soukis, K., Merigot, K., 2021. The Lavrion silver district: reassessing its ancient mining history, Geoarchaeology, 36, 4, 617-642.

Semaan, L., Salama, M.S., 2019. Underwater Photogrammetric Recording at the Site of Anfeh, Lebanon, in: McCarthy, J., Benjamin, J., Winton, T., van Duivenvoorde, W. (Eds), 3D Recording and Interpretation for Maritime Archaeology, 67-87.

Veress, M., 2022. The Effect of Mining Activities on the Paleokarstic Features, Recent Karstic Features, and Karst Water of the Bakony Region (Hungary). Mining, 2, 757–768.

17th INTERNATIONAL CONGRESS
of the Geological Society of Greece

BULLETIN OF THE GEOLOGICAL
SOCIETY OF GREECE, SP. PUBL.

EXTENDED ABSTRACT 128

Preliminary results of black sands in Corfu Island (Ionian Sea, Greece)

Kanellopoulos C.[1*], Aggelatou, V.[1], Papatrechas C.[1]

[1] Hellenic Survey of Geology and Mineral Exploration (HSGME), 1 Spirou Loui str., Olympic Villa, 13677, Acharnae, Attiki, Greece; ckanellopoulos@gmail.com , vaggelatou@eagme.gr , chpapatrechas@eagme.gr

The grains of beach sand results from the weathering and transportation of geological formations. From a mineralogical perspective, beach sand typically consists of the durable remnants of weathering, providing insights into the original rock formation, while the transport process may involve a combination of factors such as river, wind, and sea transportation.

Typically, near the coastline, an accumulation of heavy minerals is found in certain limited places, such as the swash zone of wave run-up. These accumulations are typically distinguished by their dark color (black sands). The accumulation sites could change rapidly over time due to varying factors that influence transportation routes, such as changes in wind or sea current patterns.

In some cases, black sands are enriched with economically significant minerals, forming placer deposits in coastal regions through gravitational segregation. Their minerals exhibit weathering resistance and, in numerous cases, are enriched with elements characterized as critical in adequate concentration and quantity that they can be extracted.

The mineral phases commonly found in black sands include quartz and other tectosilicates, phyllosilicates such as micas, chlorite, and serpentine, orthosilicates such as zircon, olivine group, and garnet group minerals, as well as spinels, titanite, rutile, and minerals from the epidote group, such as allanite.

In Greece, in recent years, numerous studies have been conducted on black sands, especially in the Northern Aegean Sea, i.e., Eastern Macedonia coastline, such as the Kavala region (Papadakis, 1975; Perissoratis et al., 1988; Pergamalis et al., 2001a, 2001b; Aggelatou et al., 2018; Papadopoulos et al., 2015, 2016, 2019; Tzifas et al., 2019; Stouraiti et al., 2020; Peristeridou et al., 2022) and in few cases in volcanic islands in Aegean Sea, such as Nisyros (Tzifas et al., 2017). Significant geochemical anomalies specifically in La and Zr, were detected along the Eastern Macedonia coastline, prompting further exploration and study to ascertain the source geological formation.

No occurrences of black sand have been reported in the Ionian Sea until now. For the first time, regions of black sand accumulation have been discovered on Corfu Island (Fig. 1). The deposits were located in the swash zone of wave run-up. Mineralogical (optical microscopy, XRD and SEM-EDS) and geochemical analyses (XRF, ICP-MS) were performed at the laboratories of the Hellenic Survey of Geology and Mineral Exploration (HSGME). Preliminary mineralogical and geochemical analyses revealed that the black sand mostly consists of chromium-rich mineral phases, iron-titanium oxides, and shows elevated concentrations of chromium, iron, and titanium, among other elements. The comprehensive investigation and characterization of areas displaying these characteristics, together with the identification of the parent geological formation, is of significant importance.

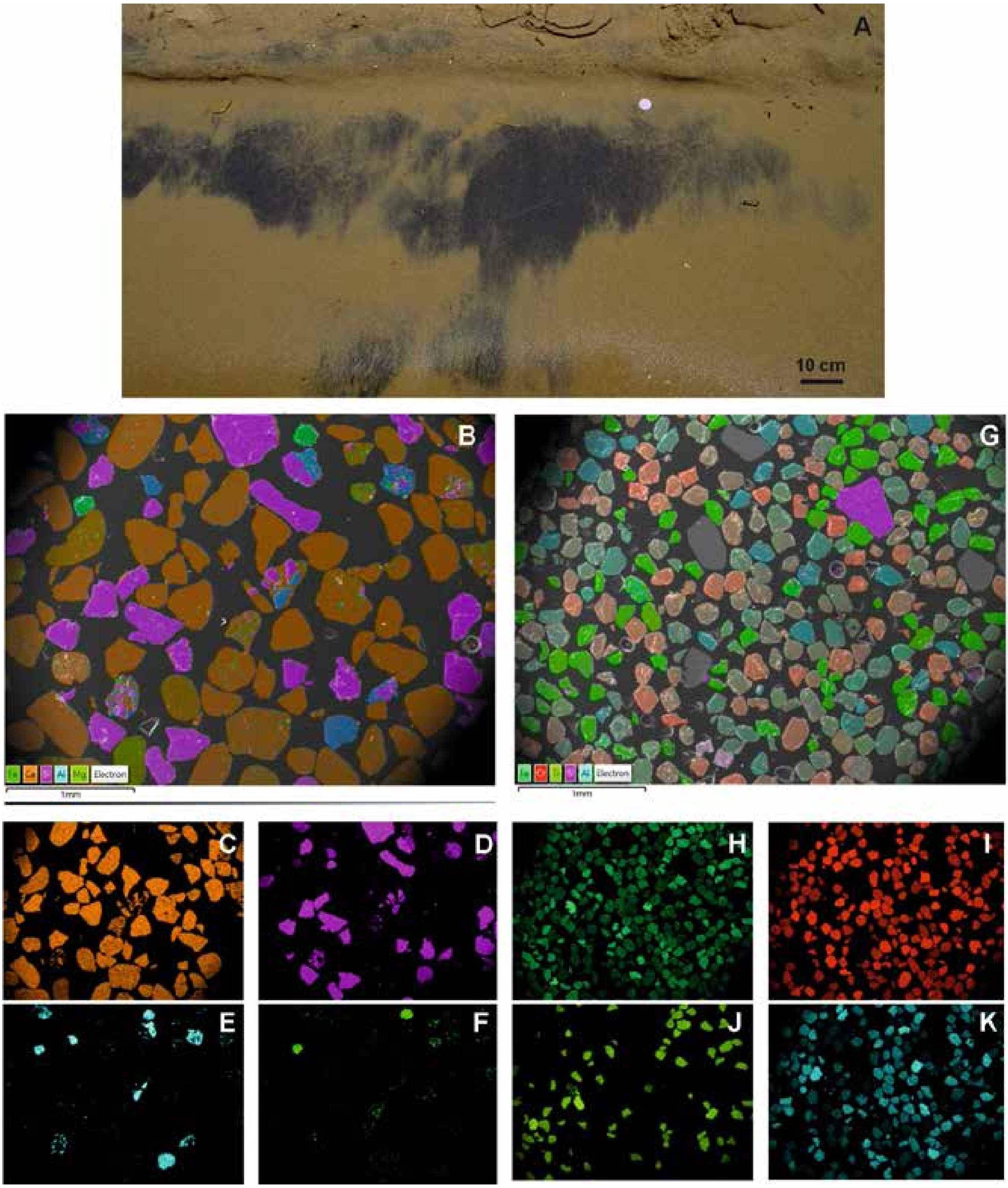

Figure 1. (A) The swash zone of wave run-up with black sand accumulation from Corfu Island. (B) Combined false color back-scattered electron image (BSEI) presenting the mapping of Fe, Ca, Si, Al, and Mg from a typical beach sand sample in the area. (C-F) False color BSEI results of the mapping, displaying only the distribution of Ca, Si, Al, and Fe. (G) Combined false color back-scattered electron image (BSEI) presenting the mapping of Fe, Cr, Ti, Si, and Al from the beneficiated black sand sample. (H-K) False color BSEI results of the mapping display only the distribution of Fe, Cr, Ti, and Al.

References

Aggelatou, V., Papamanoli, S., Stouraiti, C., Papavasileiou, K., 2018. REE distributions in the black sands of Kavala coastal zone, northern Greece: Mineralogical and geochemical characterization of beneficiation products. In Proceedings of the 1st International Electronic Conference on Mineral Science, virtual, 16–31 July 2018, Volume 1.

Papadakis, A. 1975. The black sands of Loutra Eleftheron near Kavala, Greece. Sci. Ann. Fac. Phys. Math. Univ. Thessaloniki, 15, 331–390.

Papadopoulos, A., Koroneos, A., Christofides, G., Papadopoulou, L., 2016. Geochemistry of Beach Sands from Kavala, Northern Greece. Ital. J. Geosci. , 135, 526–539.

Papadopoulos, A., Koroneos, A., Christofides, G., Stoulos, S., 2015. Natural Radioactivity Distribution and Gamma Radiation Exposure of Beach Sands Close to Kavala Pluton, Greece. Open Geosci., 7, 407–422.

Papadopoulos, A., Tzifas, I.T., Tsikos, H., 2019. The Potential for REE and Associated Critical Metals in Coastal Sand (Placer) Deposits of Greece: A Review. Minerals, 9, 469.

Pergamalis, F., Karageorgiou, D.E., Koukoulis, A., 2001a. The location of Ti, REE, Th, U, Au deposits in the seafront zones of Nea Peramos-Loutra Eleftheron area, Kavala (N. Greece) using radiation. Bull. Geol. Soc. Greece, 34, 1023–1029.

Pergamalis, F., Karageorgiou, D.E., Koukoulis, A., Katsikis, I., 2001b. Mineralogical and chemical composition of sand ore deposits in the seashore zone N. Peramos-L. Eleftheron (N. Greece). Bull. Geol. Soc. Greece, 34, 845–850.

Perissoratis, C., Moorby, S.A., Angelopoulos, I., Cronan, D.S., Papavasiliou, C., Konispoliatis, N., Sakellariadou, F., Mitropoulos, D. 1988. Mineral Concentrations in the Recent Sediments Off Eastern Macedonia, Northern Greece: Geological and Geochemical Considerations. In Mineral Deposits within the European Community, Springer: Berlin/Heidelberg, Germany.

Peristeridou, E., Melfos, V., Papadopoulou, L., Kantiranis, N., Voudouris, P., 2022. Mineralogy and Mineral Chemistry of the REE-Rich Black Sands in Beaches of the Kavala District, Northern Greece. Geosciences, 12, 277.

Stouraiti, C., Angelatou, V., Petushok, S., Soukis, K., Eliopoulos, D., 2020. Effect of Mineralogy on the Beneficiation of REE from Heavy Mineral Sands: The Case of Nea Peramos, Kavala, Northern Greece. Minerals, 10, 387.

Tzifas, I.T., Misaelides, P., Godelitsas, A., Gamaletsos, P.N., Nomikou, P., Karydas, A.G., Kantarelou, V., Papadopoulos, A., 2017. Geochemistry of coastal sands of Eastern Mediterranean: The case of Nisyros volcanic materials. Geochemistry, 77(3), 487-501.

Tzifas, I.T., Papadopoulos, A., Misaelides, P., Godelitsas, A., Göttlicher, J., Tsikos, H., Gamaletsos, P.N., Luvizotto, G., Karydas, A.G., Petrelli, M., et al. 2019. New Insights into Mineralogy and Geochemistry of Allanite-Bearing Mediterranean Coastal Sands from Northern Greece. Chem. Der. Erde., 79, 247–267.

17th INTERNATIONAL CONGRESS of the Geological Society of Greece

BULLETIN OF THE GEOLOGICAL SOCIETY OF GREECE, SP. PUBL.

EXTENDED ABSTRACT 129

Preliminary results on Agios Efstratios island (NE Aegean Sea, Greece) geology

Kanellopoulos C.[1*], Galanakis D.[1], Moforis L.[2], Sboras S.[3], Chalkiadaki O.[1], Xirokostas N.[1], Vougioukalakis G.[1]

[1] Hellenic Survey of Geology and Mineral Exploration (HSGME), 1 Spirou Loui str., Olympic Villa, 13677, Acharnae, Attiki, Greece; ckanellopoulos@gmail.com, dgalanakis@eagme.gr, ochalkiadaki@eagme.gr, nxirokostas@eagme.gr, gvougioukalakis@eagme.gr

[2] Faculty of Geology and Geoenvironment, Department of Historical Geology-Paleontology, Panepistimioupolis, Zografou, Athens; leonidasmoforis@gmail.com

[3] Institute of Geodynamics, National Observatory of Athens, Lofos Nymphon, Thesio, 11810 Athens, Greece; sboras@noa.gr

Agios Efstratios Island is a small, isolated island located in the northeastern Aegean Sea. The island is situated approximately 30 km southwest of Limnos Island and approximately 80 km northwest of Lesbos Island. It covers an area of approximately 43,000 km² and is distinguished by its rocky geomorphology. Despite its closeness to the volcanic islands of Lesvos and Limnos, as well as its location near the North Aegean Trough, geological data regarding it is limited (i.e., Fytikas et al., 1980, IGME, 1983, Pavlidis and Tranos, 1991).

In light of these conditions and the limited geological understanding of the region, the Hellenic Survey of Geology and Mineral Exploration (HSGME) organized a field expedition. The objectives of the expedition were to achieve a more thorough comprehension of the geology of Agios Efstratios through the creation of a new geological map (Fig. 1), identifying and mapping new geological formations, and an assessment of the island's volcanic formations.

Seven distinct geological formations were recognized and sampled on Agios Efstratios island. No Alpine basement formation has been identified on the island; However, many volcano-tectonic data and structures have been documented. The two primary formations are volcanoclastic-pyroclastic formations of significant thickness (several tens of meters) of Oligocene to Lower Miocene age, covering most of the island. The volcanoclastic formations consist mostly of epiclastics (debri flows, lahars, hypercocentrated flood flows) and in a less extension of tuffs and tuffites, primarily of intermediate to acid composition. These formations typically have well-defined stratified layers (Fig. 1). Irregular, scattered, and ungraded fragments of volcanic rocks, mostly boulders of lavas, are incorporated into the tuffs, alongside ejecta and bombs predominantly of high-K calc-alkaline tracyandesitic to andesitic-dacitic composition (Fig. 2), based on new geochemical analysis. The southern volcaniclastic-pyroclastic formation developed from nonvisible nowadays volcanic center(s) south of Agios Efstratios, whereas the northern volcanoclastic formation also formed from nonvisible nowadays volcanic center(s) north-east of Agios Efstratios. According to Fytikas et al. (1980), these deposits belong to the late Oligocene-early Miocene (17 Ma, 22 Ma), similar to the age of Lemnos Island volcanic products. Volcanic vents and block and ash flows were detected on the island's southeastern coast. Intense fault-related hydrothermal alteration has been reported on the island, leading to the development of bentonites and zeolites (Pe-Piper and Piper, 2002).

The other five geological formations of the island occur mainly in the northern and northeastern parts; there are small occurrences of the recent Holocene alluvial deposits, coastal deposits, talus cones and scree, Upper Miocene marine limestones, and Oligocene clastic formations (Fig. 1).

The recent Holocene alluvial deposit reaches a thickness of up to 20 m and is predominantly composed of sandy, clay, and pebble materials; in the NE part of the island, there appears to be a fluvial deposit of dunes. The Oligocene sediments consist of clays, mudstones, sandstones, and conglomerates (Fig. 3). The IGME (1983) mentions that lignite intercalations occur in the deeper sections of the Oligocene sediments. The Miocene limestone consists of bedded to massive calcite-marly organogenic limestones from a shallow water environment (Fig. 4), with dip 10-15° to the E-SE, including pieces of lamellibranchs, gastropods, algae, ostracods, and foraminifera (Milliolidae, Rotaliidae). The formation unconformably overlays the pyroclastic formation (IGME, 1983).

The geological formations of the island demonstrate substantial evidence of neotectonic movements from the post-middle Miocene to the present (Pavlidis and Tranos, 1991). Mercier et al. (1989) suggest that the neotectonic regime of the island is extensional and can be categorized into two separate periods. The minimal primary stress ($\sigma 3$) during the Pliocene-early Pleistocene epoch was oriented NE-SW, whereas the $\sigma 3$ axis from the middle Pleistocene to the present phase trends N-S.

The current geodynamic regime activates NE-SW direction strike-slip dextral faults, which displace older neotectonic structures and geological formations. The last activation occurred in 20th February 1968 after a strong 6.8 earthquake when the seismic strike-slip fault cut the island in half with a NE-SW direction (Fig. 1).

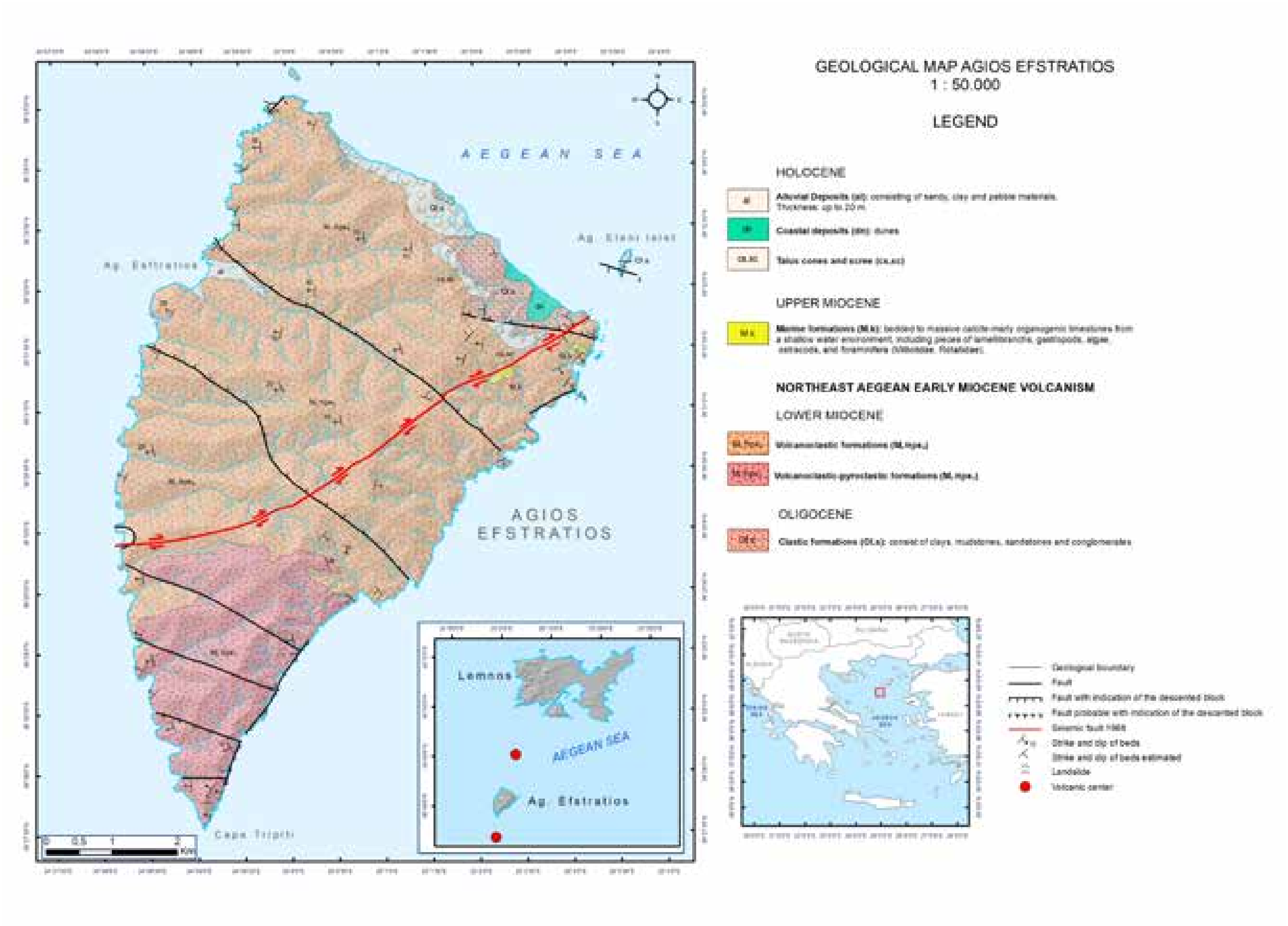

Figure 1. Geological map of Agios Efstratios island.

Figure 1. Well-developed thick stratified layers of pyroclastic formations (several tens of meters).

Figure 2. Characteristic example of a fragment of volcanic rock embedded in the tuffs (see red arrow).

Figure 3. Oligocene sediments.

Figure 4. Miocene limestone formation.

References

Fytikas, M., Giullani, O., Innocenti, F., Manetti, P., Mazzuoli, R., Peccerillo, A. & Villari, L. 1980. Neogene Volcanism of the Northern and Central Aegean Region. Annls g~ol. Pays Hell. 30, 106-129.

IGME, 1983. Geological map of Greece, Agios Efstratios sheet (scale 1: 50,000). IGME, Athnes, by Latsoudas, Ch., Tsaila-Monopolis, St. & Chorianopoulou, P.

Mercier, J. L., Simeakis, K., Sorel, D. & Vergely, P. 1989. Extensional tectonic regimes in the Aegean basins during the Cenozoic. Bas/n Res. 2, 49-71.

Pavlidis S.B., Tranos, M.D., 1991. Structural characteristics of two strong earthquakes in the North Aegean: Ierissos (1932) and Agios Efstratios (1968). Journal of Structural Geology, Vol. 13, No. 2, pp. 205-214

Pe-Piper, G. and Piper, D., 2002. The igneous rocks of Greece, the anatomy of an orogeny. Gebruder Borntraeger, Berlin.

17th INTERNATIONAL CONGRESS
of the Geological Society of Greece

BULLETIN OF THE GEOLOGICAL SOCIETY OF GREECE, SP. PUBL.

EXTENDED ABSTRACT 130

Pagasitikos volcanism (Lichades-Kamena Vourla-Achillio-Mikrothives-Porfyrio-Psathoura): Preliminary results on a Quaternary tectonically related volcanism.

Kanellopoulos C.[1], Galanakis D.[1], Sboras S.[2], Iordanidou, K.[2], Moforis L.[1,3], Xirokostas N.[1], Chalkiadaki O.[1], Vougioukalakis G.[1]

[1] Hellenic Survey of Geology and Mineral Exploration (HSGME), 1 Spirou Loui str., Olympic Villa, 13677, Acharnae, Attiki, Greece; ckanellopoulos@gmail.com , dgalanakis@eagme.gr , kiordanidou@eagme.gr , nxirokostas@eagme.gr , ochalkiadaki@eagme.gr , gvougioukalakis@eagme.gr

[2] Institute of Geodynamics, National Observatory of Athens, Lofos Nymphon, Thesio, 11810 Athens, Greece; sboras@noa.gr

[3] Faculty of Geology and Geoenvironment, Department of Historical Geology-Paleontology, Panepistimioupolis, Zografou, Athens, Greece; leonidasmoforis@gmail.com

In the greater Pagasitikos Gulf, Oreoi Strait, northern Euboea Gulfand NW Aegean Sea regions, a series of volcanic centers, namely Lichades, Kamena Vourla, Achillio, Mikrothives, and Porfyrio, occur at the western extremity of the southwestern segment of the North Anatolian Fault, (e.g. Ktenas, 1927; Georgalas, 1938; 1940; Georgiades, 1958; Marinos, 1958; Pe & Panagos, 1976, Innocenti *et al.*, 1979, Clapsopoulos, 1991, Pe-Piper and Piper, 2002, Fig. 1). Despite their early identification and studies (e.g., Ktenas, 1927, Georgalas, 1938, 1940), their proximity to important tectonic structures, and their correlation with other geological features, i.e. presence of hot springs/geothermal fields (Kanellopoulos *et al.*, 2017a, 2017b, 2018), there are no further systematic geological studies conducted for these occurrences.

The Lichades island complex consists of a series of trachyandesite volcanic islands (Georgalas, 1938; Georgiades, 1958), with a characteristic dome on the island of Strongili. The geochronological dating for the lava flows of the Lichades islands indicate an age of 0.5 Ma (K-Ar, Fytikas *et al.*, 1976).

Adjacent to Lichades is the trachyandesitic lava outcrop of Kamena Vourla (formerly known as Agios Ioannis), located on the mainland (Georgalas, 1938; Georgiades, 1958, Kanellopoulos *et al.*, 2019). The geochronological data for Kamena Vourla indicate an age of 1.7 Ma (K-Ar, Bellon *et al.*, 1979).

At Achilleon, occur a trachyandesite dome, located near Tymbanos Hill (Marinos, 1958). The geochronological data at Kamena Vourla indicate an age of 2.68-3.4 Ma (K-Ar, Innocenti *et al.*, 1979; Pe-Piper and Piper, 1979).

At Porphyrion near Volos, a trachyandesite lava flow is present (formerly known as Kadir Agas in earlier literature) (Georgiades, 1958). Geochronological data indicate an age of 1.2-1.6 Ma (K-Ar, Innocenti *et al.*, 1979; Pe-Piper and Piper, 1979).

At Microthibes, a plateau of trachyandesite lavas, with a total volume of around 0.2 km^3, is present (Ktenas, 1927). Geochronological data indicates an age of 1.5 Ma (K-Ar, Innocenti *et al.*, 1979).

At Psathoura island in the NW Aegean Sea, basaltic trachyandesite lavas compose the island (Koutsovitis *et al.*, 2015; Ntaflos *et al.*, 2017). Geochronological data indicate an age of 0.7 Ma (K-Ar, Fytikas *et al.*, 1984).

In the past, multiple theories have been proposed regarding these volcanic centers; among which is that are related to the western extension of the South Aegean active volcanic arc (Pe and Panagos, 1976; Pe-Piper and Piper, 1989), and they are associated with a deep source likely linked to the continuation of the North Anatolia fault, and unrelated to the plate subduction context (Fytikas *et al.*, 1985). Innocenti *et al.* (2010) utilized Sr–Nd–Pb isotopic data to associate this volcanic center with the extensive volcanic belt that formed north of the Pelagonian–Attic–Cycladic–Menderes massifs, which spans a considerable region from NW Greece–Macedonia to the Aegean–western Anatolia, covering a duration of 35 Ma.

Kanellopoulos *et al.* (2017a, 2017b, 2018) proposed that the volcanic center of Lichades and its associated magmatic chamber serve as the thermal source and contribute a fraction of deep magmatic fluid to the geothermal fluid of the Euboea-Sperchios system, in conjunction with seawater and minimal meteoric water input. Northern Euboea (or Evia) and the adjacent region of the mainland in eastern Central Greece (Sperchios area) are acknowledged as possessing one of the highest geothermal gradients in Greece, following the active volcanic arc of the southern Aegean (Fytikas and Kolios, 1979).

New data derived from geochemical and mineralogical analyses, tectonic measurements, and field observations confirmed the strong geochemical correlation between these volcanic centres and simultaneously elucidated their connection to the region's dynamic tectonic setting.

Based on geological, seismological, and geodetic data (e.g. Galanakis, 1997; Galanakis *et al.*, 1998; Chousianitis *et al.*, 2024 and references therein), the study area undergoes a roughly N-S oriented extension. As a result, E-W- to ESE-WNW-striking normal faults dominate in the area. However, the shear that prevails in the North Aegean Sea, as the western continuation of the North Anatolian Fault, seems to affect the eastern part of the Pagasitikos Gulf and North Euboea, forming a locally transtensional regime. Neotectonic investigations in central Greece suggest that the current extensional stress field dates back to Middle

Pleistocene, following a NE-SW trending extensional phase which was active from Pliocene to Early Pleistocene (e.g., Caputo & Pavlides, 1993). The faulting due to the current stress field has significantly affected the topographic relief by forming horst-graben systems of various scales.

The volcanic centers are located along neotectonic structures (Fig. 1). The Porphyrio and Microthebes centers are related to the Nea Anchialos fault zone, an active structure responsible for the July 9, 1980, double earthquake (two strong earthquakes of M_W 6.5 and M_W 6.1, 24 mins apart). The Achillio center is located next to the Oreoi Strait, in a small fault system that is affected by the narrow graben that forms this NE-SW trending channel. The Kamena Vourla center outcrops along an area of dense faulting where the western prolongation of the Atalanti and the eastern tip of the Kamena Vourla faults occur. The Lichades center is situated on the western prolongation of the Gialtra – Agios Georgios fault, which shapes the southern coastline of the westmost part of Euboea. It is obvious that all volcanic occurrences coincide and are associated to the active tectonic of this region.

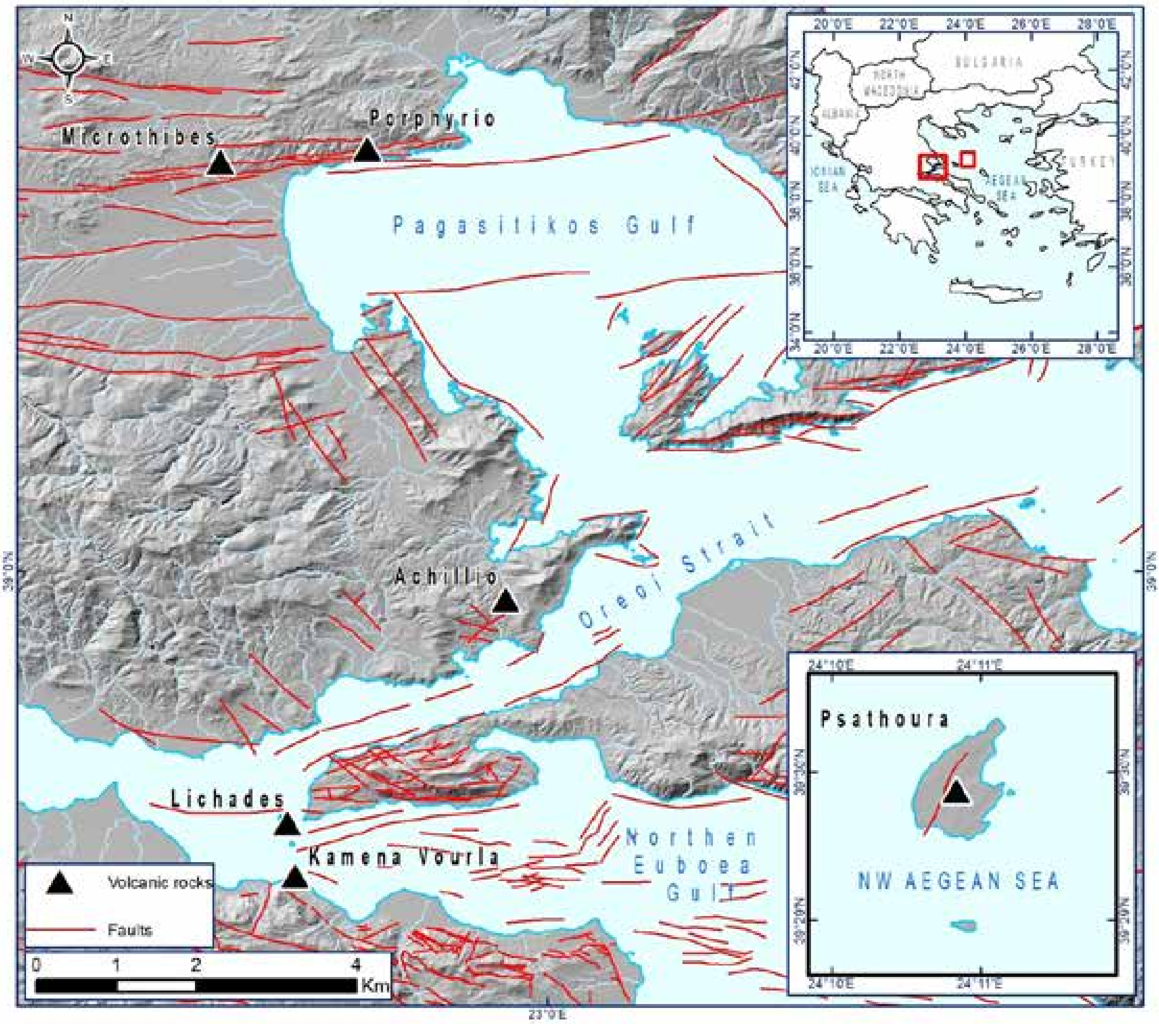

Figure 1. Geological map of the area of interest.

References

Bellon, H., Jarrige, J.J., Sorel, D., 1979. Les activites magmatiques egeennes de l'Oligocene a nos jours et leurs cadres geodynamiques. Donnees nouvelles et synthese. Rev. Géol. Dynam. Géog. Phys. 21, 41–55

Caputo, R., & Pavlides, S. (1993). Late Cainozoic geodynamic evolution of Thessaly and surroundings (central-northern Greece). Tectonophysics, 223(3-4), 339-362.

Clapsopoulos, I., 1991. Petrology, geochemistry and origin of Pliocene - Pleistocene potassium-rich volcanic rocks from Greece. PhD thesis, University of Manchester (UK), 252pp.

Chousianitis, K., Sboras, S., Mouslopoulou, V., Chouliaras, G., & Hristopulos, D. T. (2024). The upper crustal deformation field of Greece inferred from GPS data and its correlation with earthquake occurrence. Journal of Geophysical Research: Solid Earth, 129(4), e2023JB028004.

Ntaflos, T., Wegner, W., Hauzenberger, C., Vatougios, K., Kitipis, C., 2017. Geochemical evolution of the monogenetic volcanic islet Psathoura in the NE Aegean region, Greece. EGU, vol. 19, EGU2017-13601-2.

Fytikas, M., Giuliani, O., Innocenti, F., Marinelli, G., Mazzuoli, R., 1976. Geochronological data on recent magmatism of the Aegean Sea. Tectonophysics, 31, T29-T34.

Fytikas, M. and Kolios, N., 1979. Preliminary heat flow map of Greece. In: Cermak, V., Rybach, L. (Eds.), Terrestrial Heat Flow in Europe. Springer-Verlag, 197-205.

Fytikas, M., Innocenti, F., Manetti, P., Mazzuoli, R., Peccerillo, A., and Villari, L., 1985. Tertiary to Quaternary evolution of volcanism in the Aegean region, The Geological Evolution of the Eastern Mediterranean, Special Publ. Geol. Soc., 17, 687–699.

Galanakis D., 1997. Neotectonic structure and stratigraphy Neogene and Quaternary sediments of Almyros-Pagasitikos basin, Pilio, Oreoi-Trikeri chanel and Maliakos gulf. Ph.D.Thesis.Aristot. Univer.Thessaloniki, Unpub., (in Greek), 260p.

Galanakis D., Pavlides S., Mountrakis D., 1998. Recent Brittle Tectonic in Almyros -Pagasitikos, Maliakos, N. Euboia & Pilio. Bull. Geol. Society of Greece, XXXII/1, 263-273.

Georgalas, G.C., 1938. Le volcan des îles Likhades et de Hagios Ioannis (Kammena Vourla). Praktika Academia Athinion, 13, 86–98.

Georgalas, G.C, 1940. Über den chemismus der laven der vulkane von Lichadonissia, Wromolimni und Hagios Ioannis (Kamena Wourla). Praktika Academia Athinon 1940, 15, 116–131.

Georgiades, A.N., 1958. Sur une nouveau centre volcanique Pleistocène sur la route de Volo à Almyrosen Théssalie. Praktika Academia Athinion 33, 257–269.

Innocenti, F., Manetti, P., Peccerillo, A., Poli, G., 1979. Inner arc volcanism in NW Aegean arc: geochemical and geochronological data. - N.Jb. Miner., Mh. 1979: 145-158.

Innocenti, F., Agostini, S., Doglioni, C., Manetti, P., Tonarini, S., 2010. Geodynamic evolution of the Aegean: constraints from the Plio-Pleistocene volcanism of the Volos–Evia area. J. Geol. Soc., London, 167, 475–489.

Kanellopoulos, C., Mitropoulos, P., Valsami-Jones, E., Voudouris, P., 2017a. A new terrestrial active mineralizing hydrothermal system associated with ore-bearing travertines in Greece (northern Euboea Island and Sperchios area). Journal of Geochemical Exploration 179, 9-24, DOI: https://doi.org/10.1016/j.gexplo.2017.05.003

Kanellopoulos C., Stouraiti C., Xenakis M., Vakalopoulos P., Vougioukalakis G., 2017b. The geothermal system of northwestern Euboea Island and eastern Sperchios areas, Greece: Geological characteristics and suggested direct use applications. 11th International Hydrogeological Congress of Greece, vol. 2, 263-273.

Kanellopoulos, C., Mitropoulos, P., Argyraki, A., 2018. Radiological and hydrochemical study of thermal and fresh groundwater samples of northern Euboea and Sperchios areas, Greece: Insights into groundwater natural radioactivity and geology. Environmental Monitoring and Assessment Journal 190:265, DOI: https://doi.org/10.1007/s10661-018-6643-1.

Kanellopoulos, C., Vougioukalakis, G., Mavrogonatos, C., Megremi, I., & Iliopoulos, I., 2019. Mineralogical, Petrological and Geochemical Study of the Agios Ioannis Volcanic Rocks, Kamena Vourla Area, Greece. Bulletin of the Geological Society of Greece, 55(1), 274-289. doi:http://dx.doi.org/10.12681/bgsg.21128

Koutsovitis, P., Vougioukalakis, G., Economou, G., Xirokostas, N., Tarenidis, D., Ioakim, C., Karageorgis, A., 2015. Petrogenetic implications from Pleistocene volcanic rocks of Psathoura

Island, Greece: Mineral chemistry and geochemical data. EGU, Vol. 17, EGU2015-13365-7.

Ktenas, C.A., 1927. Le volcan de Thebes (Persouphli) en Thessalie [in Greek]. - Praktika Akad.Athinon 2: 35-44.

Kranis, H., 1999. Neotectonic activity of Fault Zones in central-eastern mainland Greece (Lokris). Ph.D. Thesis, University of Athens, Greece (in Greek).

Marinos, G., 1958. The Achilleon volcano in eastern Greece. [in Greek]. Bull. Geol. Soc. Greece 3: 64-72

Pe, G. and Panagos, A., 1976. Comparative geochemistry of the Northern Eubeoecos 26 lavas. Bulletin of the Geological Society of Greece, 9, 95–133 (in Greek).

Pe-Piper, G. & Piper, D.J.W (1979): Plio-Pleistocene age of high-potassium volcanism in the northwestern part of the Hellenic arc. Tschermaks Miner. Petrograph. Mitt. 26: 163-165.

Pe-Piper, G. and Piper, D., 1989. Spatial and temporal variation in Late Cenozoic back-arc volcanic rocks, Aegean Sea region. Tectonophysics, 169 (1–3), 113-134.

Pe-Piper, G. and Piper, D., 2002. The igneous rocks of Greece, the anatomy of an orogeny. Gebruder Borntraeger, Berlin.

17th INTERNATIONAL CONGRESS of the Geological Society of Greece

BULLETIN OF THE GEOLOGICAL SOCIETY OF GREECE, SP. PUBL.

EXTENDED ABSTRACT 131

Investigating crustal deformation of Zakynthos Island using Satellite Interferometry (InSAR): pre- and post- seismic analysis of the October 25, 2018 earthquake.

Kantareli K.[1], Sakkas V.[1].

(1) Geophysics Laboratory, Department of Geology and Geoenvironment, National and Kapodistrian University of Athens, Greece, ntinakanta@gmail.com

Introduction

This study focuses on the analysis of crustal deformation the period before and after the strong M_w6.8, 2018 Zakynthos earthquake, utilizing Interferometric Synthetic Aperture Radar (InSAR) data detecting ground surface changes over a period of six years. The earthquake took place southwest of Zakynthos Island on October 25, 2018, with an estimated magnitude of M_w6.8 (Papadimitriou et al., 2021). The earthquake was one of the most significant events in recent years in the broad region, producing noticeable ground displacement (~40 mm in the southern part of Zakynthos), reflecting the dynamic tectonic processes on the south Ionian Islands. Analysing pre- and post- seismic InSAR datasets, patterns of ground motion were identified and quantified aiming to assess the deformation processes before and after the earthquake based on the estimated velocity changes and its spatial distribution across Zakynthos.

Geology and Seismicity

Zakynthos island, located in the southern Ionian Sea, is part of the External Hellenides, a geotectonic domain shaped by the convergence of the African and European plates (Papanikolaou, 2021). The island's tectonic framework is influenced by its position along the Hellenic Subduction Zone, the active boundary of the subduction of the eastern Mediterranean oceanic lithosphere under the Aegean microplate. The island consists of series of stacked tectonostratigraphic units that were accreted during the alpine orogenic system. A significant part of the island in its western part is mainly structured by the Paxoi Unit and represents the primary tectonostratigraphic feature. In the eastern part, the Paxoi Unit is overthrusted by the Ionian unit, a structural feature that emphasizes the tectonic complexity of the region (Figure 1).

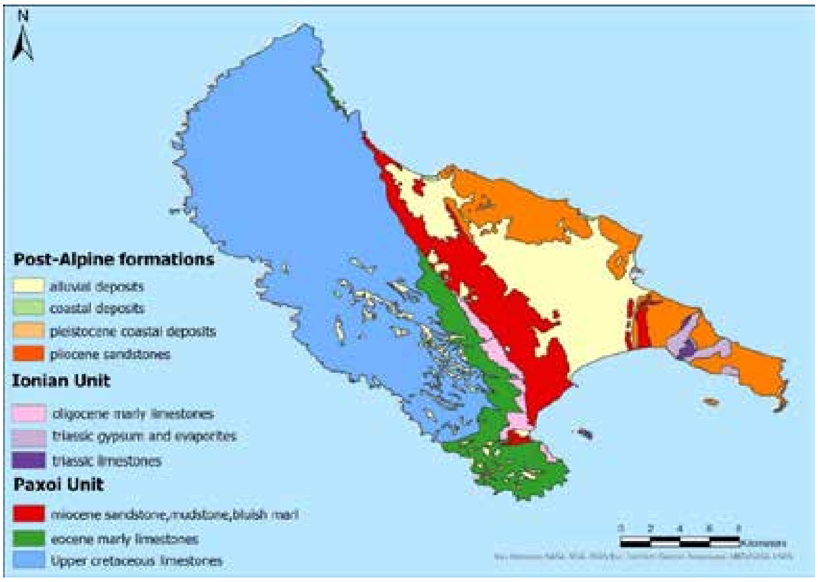

Figure 1:Geological map of Zakynthos Island (IGME, Geological Map of Greece, 1983)

The Paxoi Unit consists of a well-developed carbonate sequence that spans from the Upper Cretaceous to the Oligocene (Papanikolaou, 2021). This sequence is characterized by thick fossiliferous limestones and marly limestones, and above these carbonate rocks lie Miocene deposits, made up of marls, sandstones, and mudstones. This stratigraphic succession captures the evolving depositional setting which was influenced by the tectonic changes over millions of years. The Ionian unit comprises a Triassic sequence of limestones, evaporites and breccias, which represent different geological episodes, consisting of restricted marine deposition and subsequent tectonic disruption (Papanikolaou 2021). Overlying both units are post-Alpine Quaternary deposits, which consist of alluvial and coastal sediments, deposited during the Pleistocene and Holocene. The presence of the two distinctive geological units, Paxoi and Ionian, that dominate the eastern and western part of the island, respectively, may infer different kinematic behaviour. However, the absence of a clear tectonic feature (i.e. fault) in between these two units is questioning this assumption. Using the InSAR technique the latter will be studied aiming to examine this hypothesis.

The earthquakes that occur in the Ionian Sea are mainly generated along the Cephalonia-Lefkada transform fault zone (CLTFZ), which plays a significant role in the kinematic field of the region (Sakkas et al., 2022). This zone divides the Ionian margin into two areas, the North Ionian islands, which move north-northwestward at rates slower than 5mm/year relative to Eurasia, and the South Ionian islands that move southwestward with velocities of 6-30mm/year (Sakkas et al., 2022). The intense seismicity on the southern Ionian Sea is attributed to the proximity of this area to the CLTFZ and the Hellenic Trench (Figure 2). Zakynthos in particular, experiences intense seismic activity frequently, as it lies at the northwesternmost edge of the Hellenic arc, near the boundary where the eastern Mediterranean lithosphere subducts beneath the Aegean microplate. This complicated geotectonic setting highlights its significance in understanding regional deformation processes.

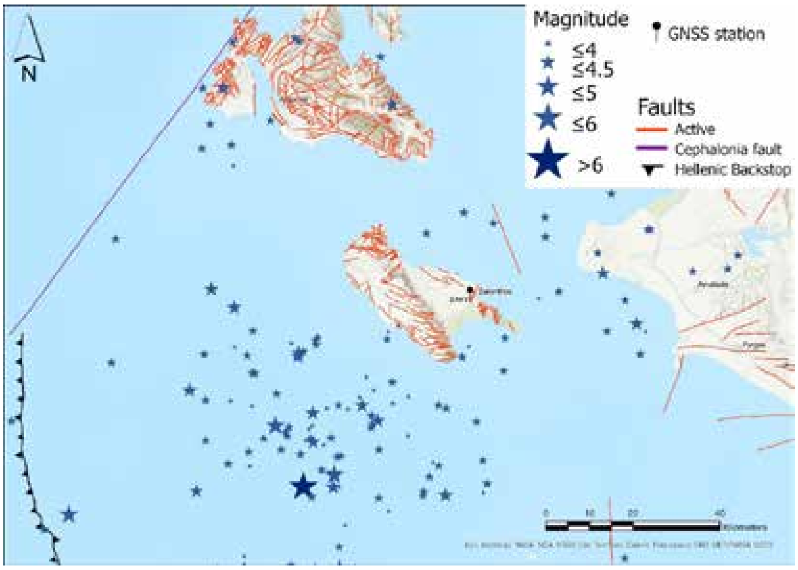

Figure 2: Seismicity of the broad area of Zakynthos Island (2015-2021) with M≥4.0 based on the catalogue of Seismological laboratory of NKUA (Fault lines from Ganas, et al., 2024)

Radar Interferometry

Interferometric Synthetic Aperture Radar (InSAR) is an advanced geodetic technique used for precise measurements of surface deformations and topographic variations on the Earth's surface. Utilizing radar signals transmitted and received by satellites, InSAR exploits the phase differences between radar acquisitions taken at different times or from slightly varied perspectives to derive changes in ground displacement. SAR satellites collect data during ascending (asc; from south to north) and descending (desc; from north to south), with the radar sensor looking to the right of the orbit trajectory. The two viewing geometries result in different line-of-sight (LOS) observations of the ground surface and refer to the displacements along the direction in which the satellite's radar beam travels, which is inclined relative to the vertical and horizontal axes. Since ground deformation occurs in multiple directions, LOS data from both ascending and descending passes are combined, to resolve the ground motion into its vertical (Vup) and horizontal eastward (Veast) components.

The decomposition of the LOS displacements into vertical and horizontal components requires knowledge of both the incidence angle (θ) and the track/azimuth angle (α) of the satellite's orbit geometry, as they define the orientation of the radar signal and the satellite's path relative to the Earth's surface (Figure 3). The incidence angle is the angle between the radar beam and the vertical axis at the point in reference, on the Earth's surface. SAR sensors typically have an incidence angle of 20-45 degrees depending on the satellite's orbit. The track angle is the angle between the satellite's orbital path and the true north. Combining the LOS displacements of ascending and descending orbital geometries (Ulos asc and Ulos desc) the vertical and horizontal components of the displacement vector are extracted based on the following expression (Fuhrmann, 2019):

$$\begin{pmatrix} U_E \\ U_U \end{pmatrix} = \begin{pmatrix} -sin\theta_{asc}\, cosa_{asc} & cos\theta_{asc} \\ -sin\theta_{desc}\, cos\alpha_{desc} & cos\theta_{desc} \end{pmatrix}^{-1} \begin{pmatrix} U_{asc} \\ U_{desc} \end{pmatrix} \quad (1)$$

Where U_U is vertical component, U_E the east component, Uasc and Udesc are the velocities in LOS direction, and θ and α are the incidence and track angles as descripted above.

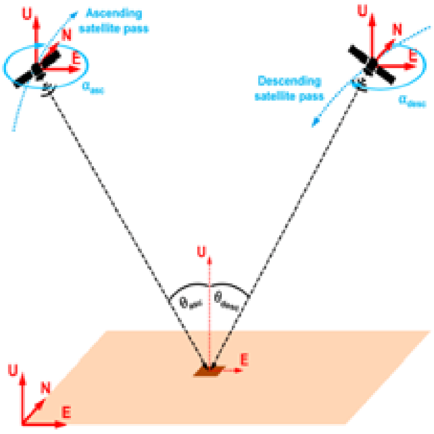

Figure 3:Schematic view of the interferometric aperture radar (InSAR) geometry for line of sight (LOS) measurements on ascending and descending satellite passes (after Fuhrmann T. 2019)

Data processing and analysis

In this study, the data utilized were derived from the European Ground Motion Service (EGMS, https://egms.land.copernicus.eu/). This service provides processed results in LOS direction, called "*Basic Product*". In this study the used results are covering the period 2015-2021 in the Island of Zakynthos. The *Basic Product* provides for each measurement point time series of displacement in the satellite LOS geometry, the estimated LOS velocity and the acceleration value for the whole-time span of the product (in this case 2015-2021). Additionally, the service offers annotated geo-localization and quality measures per measurement point. The dataset is generated from the interferometric analysis of Sentinel-1 radar images and is visualized as a vector map of measurement points color coded, both as *Ascending* and *Descending* data. The ascending measurement points were approximately 600000 and the descending approximately 380000, where each has a mean velocity and acceleration value, estimated on the time-series residuals (measured in mm/yr), and incidence and track angle values (degrees).

To estimate the velocity field before and after the October 25, 2018, a MATLAB code was used to calculate the mean velocity of each data point before and after the main shock occurrence, utilizing the time series of each one. The velocity for each period was realized applying linear least squares fitting process, using the MATLAB curve fitting tool. This toolbox utilizes the least squares method to fit a polynomial to a set of data, through minimizing the sum of the squared residuals between the observed and the predicted values of the line. The final dataset that was used, included approximately 500000 measurement points on ascending and 300000 points in descending orbit.

Data calibration

The raw time series of each measurement point provided from the EGMS dataset were divided to pre- and post-seismic periods, to enable independent analysis of each phase. These categorized data were then absolute calibrated using the velocity vector of a permanent GNSS station on Zakynthos Island (station ZAKY) with well-established ground displacement components for both these periods. Table 1 presents the velocity components of the ZAKY station, for the pre- and post- seismic period. Indicative of the calibration procedure are Figures 4 that present the calibrated velocity maps for the Ascending data set. The GNSS velocity vector was projected on the LOS direction of the two orbital geometries based on the average (due to the relatively small spatial extent of the Island) incidence and track angles for each geometry, using the expression (Hansen 2001).

$$LOS = U_U cos\theta - sin\theta \left[U_N \cos\left(a - \tfrac{3\pi}{2}\right) + U_E\, sin\left(a - \tfrac{3\pi}{2}\right)\right] \quad (2)$$

Where U_N is the real north component, rest of the annotations are presented above.

Table 1: Velocity components of ZAKY GNSS site and its LOS projection

	Pre-seismic period (mm/yr)	Post-seismic period (mm/yr)
Vup	-0.33	0.03
Veast	12.81	11.51
Vnorth	-2.50	-1.89
Vlos Ascending	-3.45	-2.62
Vlos Descending	-0.13	-0.09

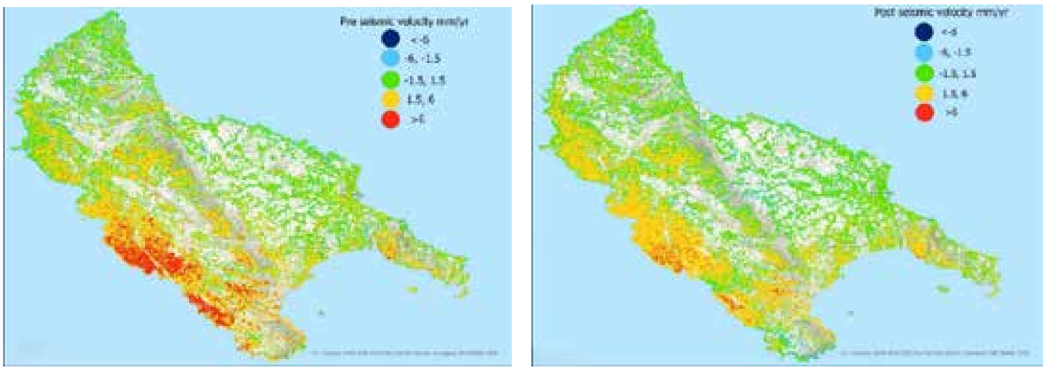

Figures 4: Ascending absolute calibrated pre- seismic (left) and post-seismic (right) velocity maps as calculated in the LOS direction.

The overall image of the crustal velocity field before and after the M_w6.8 event shows a similar pattern but of slightly different amplitudes mainly in the SW part of Zakynthos. The pre-seismic motion on the southwest part of the Island seems more intense compared to the post–seismic one, which shows smaller velocity range. As, as it is revealed by the approximately 70000 more points that have calibrated velocity value above 6mm/yr in the pre-seismic period compared to the post-seismic one.

Ortho map generation

The calibrated LOS velocity vector was then decomposed into its east-west and vertical component using the expression (1). Both incidence and track angles were measured in degrees, but in the velocity calculations were converted into radians. The used angles for both acquisition geometries are summarized in Table 2. Since the two acquisition geometries cannot have common data points, additional processing steps were adopted aiming to combine the ascending and descending data sets. As to generate the ortho maps, first a *kriging* interpolation technique was applied, to estimate values at unsampled locations based on the spatial correlation of measurement points, ensuring that the dataset is spatially continuous. This process resulted in a dataset of approximately 68000 points for the ascending and descending dataset individually. Then a *contour* tool was used, to create contour lines that visualize the variations within the dataset, and a *grid to point* conversion tool, to convert the raster data of points (grid cells) into vector point data and create a grid over the area of Zakynthos. Finally using the *extract by mask* tool, with the shoreline of the Island as a mask, the grid was refined as to include only the island and not the broad area that was automatically calculated during previous steps (Esri. *Anatomy of a Tool Reference Page*. ArcGIS Pro Documentation). With the *extract by mask* tool the dataset was reduced to 60000 points per orbital geometry, equally divided for the pre- and post- periods.

Table 2: Summary of the angles that were used in the estimation of the vertical and east-westward velocities.

Orbital geometry	Incidence angle (degrees)	Track angle (degrees)
Ascending	44.88	-9.22
Descending	38.72	190.18

The final east-west and vertical velocity field for the pre- and post- seismic period are presented in Figures 5 and 6, respectively. For the east-west velocity field, positive values indicate eastward motion, while negative values represent westward motion. Both components show similar pattern of ground motion before and after the earthquake, but of different amplitudes and spatial coverage. The central part of the Island is the area that shows the more intense discrepancies, while in the SW part of Zakynthos the overall surface motion retains its basic characteristics in between the two periods.

Discussion

The east-west displacement maps (Figure 5) reveal distinct patterns of deformation in between the two-time spans. In the pre-seismic period, the western and mostly the southern regions exhibit westward velocities below -5mm/yr, while the central and northern ones show relatively stable conditions, with velocities ranging between -2 to 1mm/yr. After the 2018 earthquake (post-seismic period), the Island shows a slight shift to the east, with more data points assigning velocities above 2mm/yr, this kinematic behaviour is more evident in the eastern and southeastern part. The more significant changes in velocity are shown near fault zones that may indicating possible co-seismic fault-related movements and ground deformation, as well as, across the main geological boundary (in the central part of the island) in between the Paxoi and Ionian units (Figure 1), since there are significant more data points exhibiting velocities over 2mm/yr.

The vertical displacement maps (Figure 6) have noticeable changes across the two periods. Before the earthquake, the southern-most region shows subsidence with velocities even lower than -10mm/yr, while the central-southern part remains relatively stable, without any clear pattern of subsidence or uplift (the velocities range between -2 to 2mm/yr). However, the northern part of the Island reveals an uplifted character, with areas exhibiting vertical velocities up to 10mm/yr. In the post-seismic period, the southern part of Zakynthos does not alter its motional pattern, except that the velocities of several data points are dropping quite a lot below -10mm/yr (up to -18mm/yr). The most considerable changes are observed in the rest of the Island (northern, central and SE part) where the pre-seismic uplift pattern alters to minor subsiding motion (up to -5mm/yr). In comparison to the east-west displacement maps, the vertical ones, also seem to have fault related deformation, with differential motion across them, but not so noticeable in the geological boundary between the two units.

The overall image of the two displacement components (E-W and Up), indicates major changes primarily on the northern and central-eastern part of Zakynthos. The pre seismic period is characterised by mostly stable conditions, with small westward motion and slight uplift. The post-seismic period shows change on the sign in both components. After the M_w6.8 main shock, the geological boundary seems to play a less significant role in terms of vertical displacement, since there is no clear differentiation between the two geological units. In contrast the east-west component shows a more noticeable differentiation, with the motion gaining an eastward character. The vertical component highlights a more distinctive change in between the northern and southern part of the Island, since the northern part is clearly changing its kinematic behaviour, from uplift before the earthquake to subsidence after it. Conclusively, the comparison between the pre- and post-seismic period highlights a kinematic differentiation between the northern and southern part of the Island, which does not coincide with any geological boundary or tectonic feature. This change takes place in a zone that crosscuts the Island (with east-west direction) along the centre of the island (Figure 6, lower part).

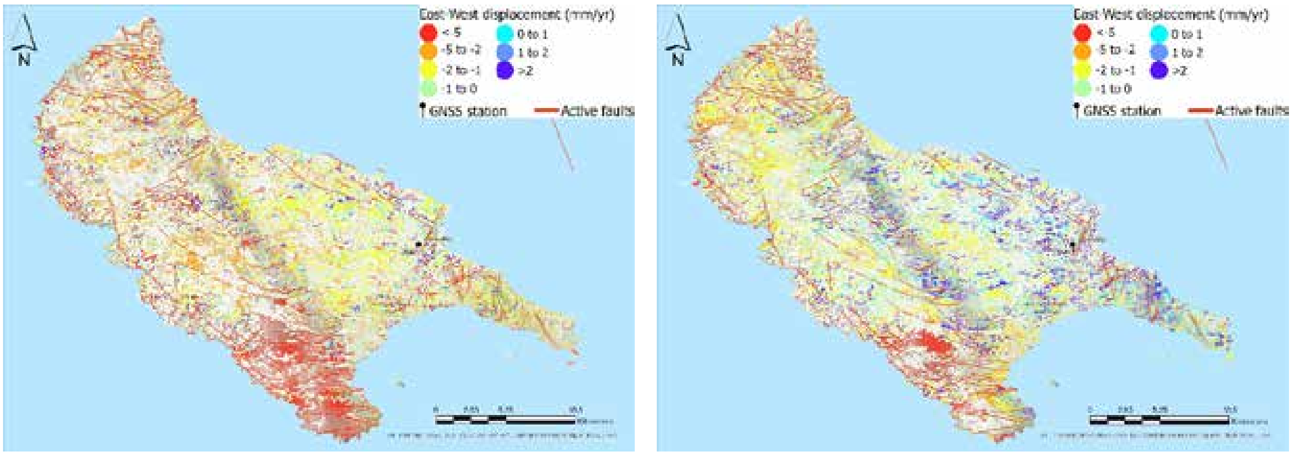

Figures 5: Pre- seismic (left) and post-seismic (right) east-west displacement in the island.

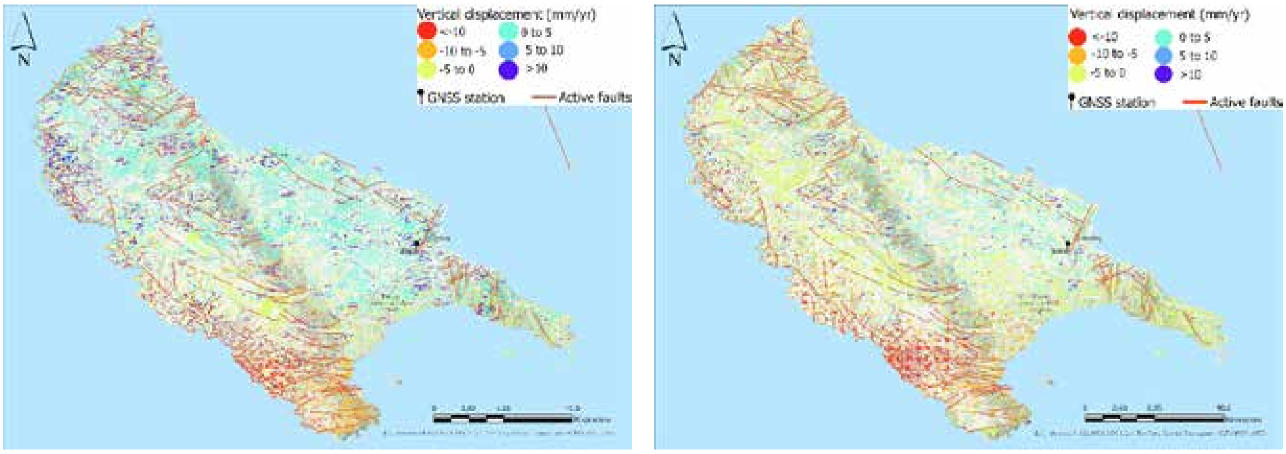

Figure 6: Pre- seismic(left) and post- seismic (right) vertical displacement in the island. The dash line indicates the approximate position of the zone that differentiates the northern and the southern kinematic behavior of Zakynthos.

Acknowledgements

The authors would like to thank Prof. A. Tzanis (Department of Geology and Geoenvironment, NKUA) for his help on the MATLAB codes used in this work. The Seismological data were obtained by the Seismological Laboratory of NKUA.

References

Esri. Anatomy of a Tool Reference Page. ArcGIS Pro Documentation https://pro.arcgis.com/en/pro-app/latest/tool-reference/introduction-anatomy/anatomy-of-a-tool-reference-page.htm

European Ground Motion Service, https://egms.land.copernicus.eu/

Fuhrmann, T., Garthwaite, M.C., 2019. Resolving three-dimensional surface motion with InSAR: Constraints from multi-geometry data fusion. Remote Sensing, 11(10), 1206. https://doi.org/10.3390/rs11101206

Ganas, A. et al. 2024. NOAFaults v6.0: New upgrades of the NOA Geospatial database of Active Faults in the broader Aegean area. https://zenodo.org/records/1316894

Hanssen, R.F., 2001. Radar interferometry: data interpretation and error analysis. Springer, Berlin.

Papadimitriou, P., Kapetanidis, V., Karakonstantis, A., Spingos, I., Pavlou, K., Kaviris, G., Kassaras, I., Sakkas, V., Voulgaris, N. 2021. The 25 October 2018 Zakynthos (Greece) earthquake: Seismic activity at the transition between a transform fault and a subduction zone. *Geophys. J. Int.*, *225*, 15–36. https://doi.org/10.1093/gji/ggaa575

Papanikolaou, D., 2021. The Geology of Greece, 1st ed. Springer International Publishing, pp. 1-345.

Sakkas V., Kapetanidis V., Kaviris G., Spingos I., Mavroulis S., Diakakis M., Alexopoulos J.D., Kazantzidou-Firtinidou D., Kassaras I., Dilalos S., Vassilakis E., Kotsi E., Tselentis G., Lekkas E., Voulgaris N. 2022. Seismological and Ground Deformation Study of the Ionian Islands (W. Greece) during 2014–2018, a Period of Intense Seismic Activity. App. Sciences 12 (5), art. no. 2331. DOI: 10.3390/app12052331.

17th INTERNATIONAL CONGRESS
of the Geological Society of Greece

BULLETIN OF THE GEOLOGICAL
SOCIETY OF GREECE, SP. PUBL.

EXTENDED ABSTRACT 132

Application of a machine-learning model for the determination of focal mechanisms in the area of the Corinth Rift Laboratory Near-Fault Observatory (CRL NFO), Central Greece

Kapetanidis V.[1], Spingos I.[1], Kaltsas, C.[1], Kaviris G.[1]

(1) National and Kapodistrian University of Athens, Section of Geophysics-Geothermy, Seismological Laboratory, Athens, Greece, vkapetan@geol.uoa.gr

Research Highlights

- First motion polarities determined using an ML model yielded results comparable with manual measurements.
- Discrepancies were mainly observed at stations in larger epicentral distances or equipped with accelerometers.

Introduction

The large quantities of available seismic waveform data have rendered their manual analysis a challenging task. The unification of seismic networks in Greece (e.g., Evangelidis et al., 2021) has improved the completeness of the routine analysis seismic catalogs. However, as the number of earthquakes is multiplied almost tenfold for every lowering of a magnitude unit, manual analysis can only go so far before the workload becomes prohibiting. Conventional automatic seismic P- and S-wave arrival-time picking methods also have downsides, depending upon the objective function used in each case. Despite providing quick solutions, the measurements of these automatic methods are usually less accurate than those performed by human analysts, and they need to be manually revised for their quality to be improved. However, in recent years, the rise of Machine-Learning (ML) models has revolutionized the automatic processing of seismological data. ML models, such as PhaseNet (Zhu & Beroza, 2019) and EQTransformer (Mousavi et al., 2020), are now used for the automatic analysis of huge datasets, greatly augmenting the number of detected events and lowering the completeness magnitude of seismic catalogs. Even more surprisingly, in terms of accuracy, these ML methods provide results that are on par with manually analyzed data (e.g., Mousavi et al., 2020) and can even recognize P- and S-wave arrivals in noisy signals without filter application (e.g., Zhu & Beroza, 2019).

An even more challenging task is the automatic identification of P-wave First Motion Polarities (FMPs). For earthquakes of moderate or higher magnitude (e.g., M^{3}3.6), the focal mechanisms can usually be determined through moment tensor inversion, by fitting synthetic to the observed waveforms. FMPs, on the other hand, are useful for determining focal mechanisms for weak events (M£3.5), particularly when the network density is adequate near the epicentral area. The distribution of FMPs depends on the radiation pattern of seismic energy at the source. In the double-couple model, FMPs are distributed in four quadrants, characterized by the alternating sign of the first motion recorded at the vertical component of the seismic stations. These first pulses can be impulsive or emergent, depending on the angle of emergence of the seismic ray at the focus, relative to the radiation pattern of the faulting, which defines the focal mechanism; i.e., the strike, dip, and rake of the rupture. Rays originating near the P or T principal axes of the moment tensor are expected to produce impulsive negative or positive first motions, respectively. On the other hand, rays originating near the nodal planes or the null axis are likely to produce emergent first motions, which cannot be easily distinguished (small, nearly zero amplitude). Furthermore, the Signal-to-Noise Ratio (SNR) of weak-magnitude events can be too low for even a P-wave arrival to be picked. The application of filters to lower the noise level and improve SNR can distort the first pulse and lead to an erroneous FMP measurement. Even when a P-wave arrival-time can be roughly assessed, the analyst must decide whether to characterize the polarity of the first motion or skip it to avoid an error. Other measurements that can help constraining the focal mechanisms of weak events include the S-to-P amplitude ratio and the S-wave polarization direction (e.g., Kapetanidis et al., 2015).

As the characterization of the FMP is a pattern recognition task, it has also been the subject of studies employing methods based on artificial intelligence. Such ML models can recognize these patterns and classify the first pulse as being positive or negative, assess whether it is impulsive or emergent, or decide to dismiss a measurement if the polarity cannot be safely determined. Examples of such ML models include those presented by Ross et al. (2018) and Zhao et al. (2023). Both models were trained on a large dataset of seismic waveforms from Southern California, and the authors reported a precision of ~95% or more compared to the respective FMP measurements by human analysts.

Background

The Corinth Rift Laboratory is a dense local seismological network that has been established in the Western Gulf of

Corinth (WGoC; Figure 1) since the early 2000s (Chiaraluce et al., 2022). It is one of the Near-Fault Observatories (NFOs) of the European Plate Observing System (EPOS), complemented by stations of the regional Hellenic Unified Seismic Network (HUSN). WGoC is one of the most seismically active areas in Greece, due to a high extension rate, reaching ~16 mm/yr in a ~N-S direction (Avallone et al., 2004), mainly characterized by E-W-striking normal faulting. Between December 2020 and February 2021, an intense seismic swarm occurred in WGoC (Kaviris et al., 2021; Papadimitriou et al., 2022; Serpetsidaki et al., 2023). The swarm mainly evolved in three phases, each triggered by a significant earthquake: an M_w=4.6 event on 23 December 2020 near Marathias; an M_w=5.0 event on 12 January 2021 near Trizonia Island; and an M_w=5.3 event on 17 February 2021 (Zahradník et al., 2022), north of Psathopyrgos. An examination of the aftermath period up to December 2022, showed that the swarm activity diminished after March 2021, and a background seismicity level was established, with only a few spatiotemporal clusters and two significant earthquakes of M_w=4.2 and M_w=4.3, on 30 November 2021 and 29 July 2022, respectively (Kaltsas et al., 2024). In the framework of the studies of Serpetsidaki et al. (2023) and Kaltsas et al. (2024), a total of 117 focal mechanisms were calculated between December 2020 and December 2022, with 20 from the former study being assessed through moment tensor inversion, while the rest were determined using P-wave first motion polarities. Most focal mechanisms indicate normal faulting, with a smaller proportion of strike-slip or oblique-normal events also being detected.

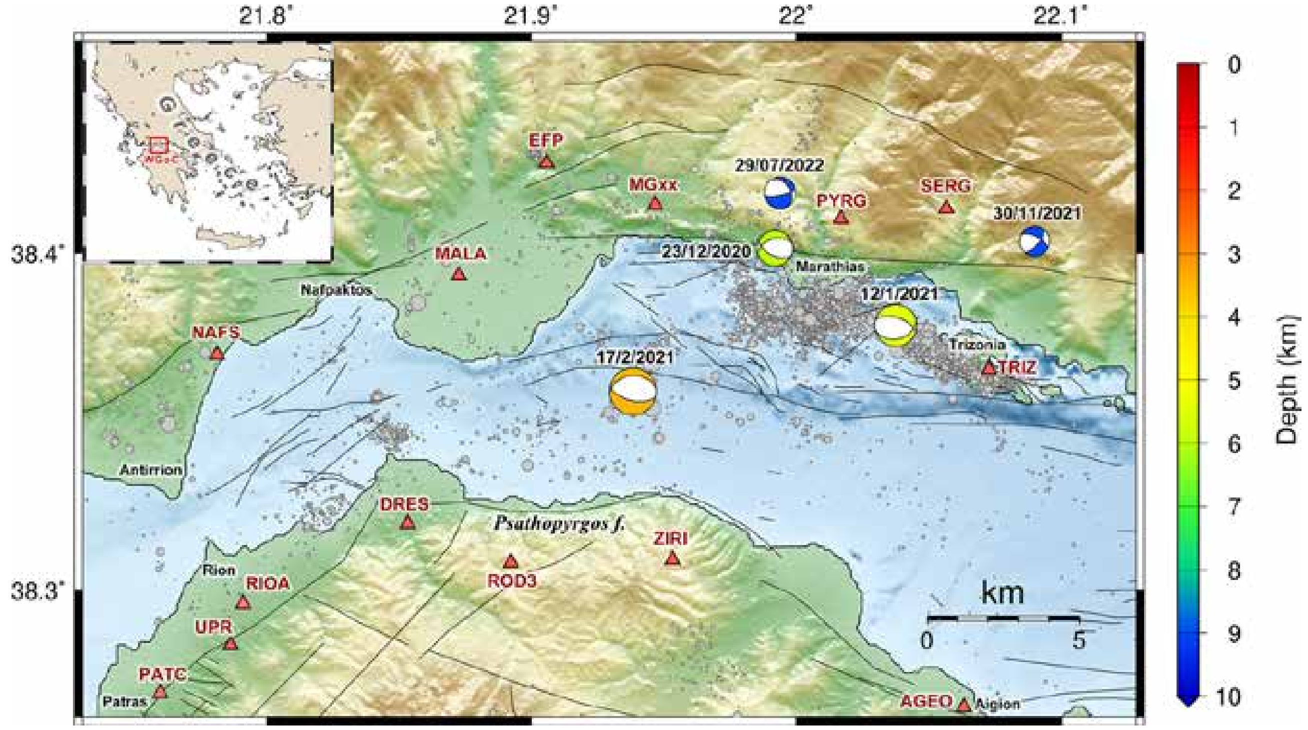

Figure 1. The Western Gulf of Corinth (WGoC) in Central Greece. Seismological and accelerometric stations of the Corinth Rift Laboratory Near-Fault Observatory (CRL-NFO) are depicted as triangles. The focal mechanisms of selected significant (M_w ³ 4.2) earthquakes of the period December 2020 – December 2022 are presented with beachball symbols. The relocated seismicity of the period December 2020 – February 2021 (gray circles) is after Serpetsidaki et al. (2023). The fault lines are from the NOAfaults database (Ganas et al., 2013).

Objectives

In this work, we apply a machine-learning model to identify the FMPs and determine the focal mechanisms of earthquakes that occurred between December 2020 and December 2022 in the western Gulf of Corinth. This will provide a perspective on the efficiency and accuracy of the applied model on the abovementioned dataset, as there are also available manually defined FMPs for a subset of the events that will be processed. The latter will be used to examine the validity of the FMPs, but also to quantify the difference in the resulting focal mechanisms derived from the herein-applied method compared to previous results of manually measured FMPs.

Data and Methods

We use a catalog of ~460 manually analyzed and relocated events from the seismic crisis in WGoC between December 2020 and February 2021 (Serpetsidaki et al., 2023), as well as 82 events from the aftermath period between March

2021 and December 2022 (Kaltsas et al., 2024); the selected events have $M^{3}2.0$. In both cases, there is a subset of events with available manually measured FMPs and calculated focal mechanisms with a grid-search method, that will be used for comparison. We acquire seismic waveform data from the EIDA nodes of Reseau Sismologique et Geodesique Francais (RESIF; https://seismology.resif.fr/eida/), for stations of the CRL network, and the National Observatory of Athens – Geodynamics Institute (NOA-GI; http://eida.gein.noa.gr/webdc3/), for stations of HUSN.

We employ the DiTing-Motion (DTM) machine-learning model (Zhao et al., 2023) to automatically identify the FMPs at local stations in the area of WGoC. For each station, the waveform recording of the vertical component is detrended, resampled to 100 sps, if necessary (e.g., for accelerometric stations, which are usually at 200 sps), and cropped to a 128-sample window of ±0.64 s around the P-arrival. We follow the workflow established by Zhao et al. (2023), also measuring the S-to-P amplitude ratio (SPR) and employing the HASH code (Hardebeck & Shearer, 2002, 2003) to determine the focal mechanisms using both FMPs and SPR. To assess the influence of the P-wave's arrival-time accuracy on FMP identifications, we also test the procedure after re-picking the P-wave in the vicinity of the previously available arrival-time with Phasenet, pre-trained with data from the INSTANCE dataset (Michelini et al., 2021). We examine DTM results in terms of FMP identification accuracy, compared to manually analyzed events, both automatically and by visually reviewing the automatic FMP characterizations (Figure 2, left). The discrepancies are also examined on a per-station level to identify any systematic issues related to particular stations. For the difference between the newly determined focal mechanisms and the previously available ones from the common subset, we calculate the Kagan angle between the two solutions and also examine the whole image of their beachball projections on the map for visible similarities or differences.

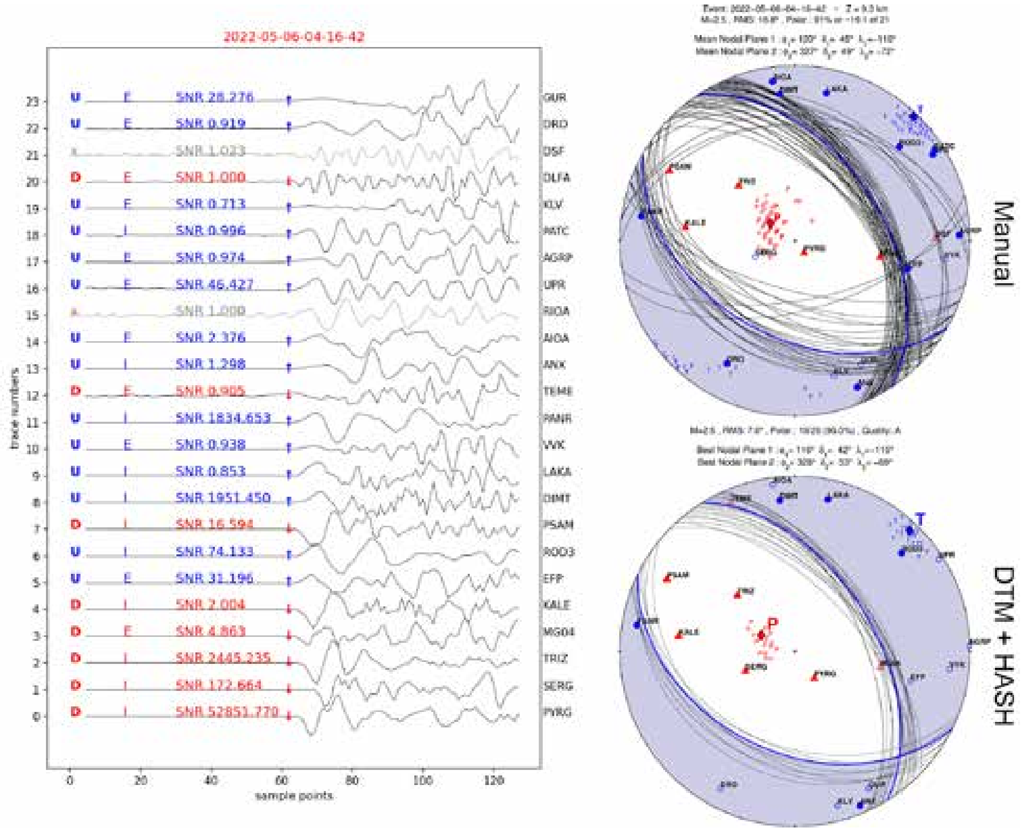

Figure 2. (Left) Example of automatic FMP identifications derived by the DiTing-Motion machine-learning model. The blue letters marked with "U" denote compression whereas the red letters marked with "D" denote dilatation. Gray lines (marked with "x") denote no measurement. "I" and "E" denote impulsive and emergent first motion, respectively. SNR is the Signal-to-Noise Ratio. (Right, Top) focal mechanism derived from manually measured FMPs and a grid-search over fault plane solutions that are consistent with the FMPs. (Right, Bottom) focal mechanism for the same event derived by HASH using the FMPs of the left panel. The RMS value refers to the angular difference between the best solution (bold blue nodal planes) and the valid individual fault planes (thin nodal planes). Blue circles denote compression and red triangles denote dilatation. Small red P and blue T symbols show the distribution of the P- and T-axes projections for valid individual solutions.

Results

The automated workflow yielded 370 focal mechanisms for the 2020-2021 WGoC seismic crisis and 65 for the aftermath period, classified by HASH with a quality grade "A". Figure 3 (left) shows a confusion matrix comparison between characterized polarities by the applied workflow and FMPs identified for the second period by Kaltsas et al. (2024), for 65 common events. The comparison shows that 82-89% of the FMPs were assessed in a similar manner both automatically and manually. Notably, however, 10-13% of FMPs were discarded by DTM. A closer examination revealed that the cases of "missed" FMPs by DTM mostly belong to either stations with accelerometric instruments, or stations at larger epicentral distances (>30 km). With the more distant stations removed from the comparison, the percentages of consistent FMP measurements rise to 87-91% and "missed" FMPs drop to 7-8% (Figure 3, right). Still, ~1% of compressional and 6% dilatational manual FMPs were characterized as being of the opposite polarity by DTM. A more detailed example is presented in Figure 4 for common events of the crisis period, where FMPs are additionally characterized as impulsive or emergent. This is a more subjective matter from the point of view of a human analyst, as an "emergent" characterization may refer to either a "gentle slope" first motion or a low-amplitude first motion, which can also be due to low SNR. DTM results show a larger percentage of agreement for impulsive FMPs than for emergent ones. A larger percentage of manually characterized "emergent" FMPs also tend to be rejected by DTM, which indicates that the classification of the ML model is generally on the more conservative side. An emergent FMP can probably be misjudged as an impulsive FMP of the same polarity, less probably as an emergent FMP of the opposite polarity, and even more rarely as an impulsive FMP of the opposite polarity.

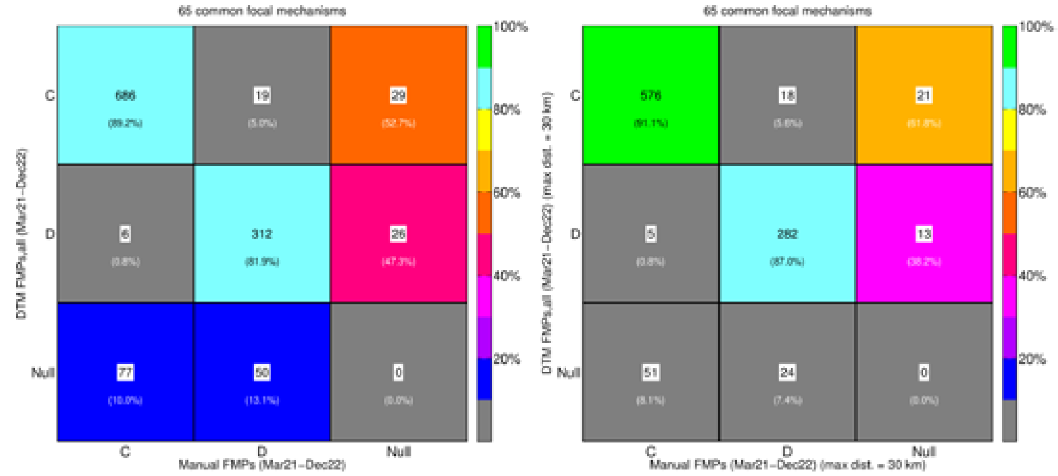

Figure 3. Confusion matrix between FMPs identified with DTM (rows) and manually (columns) for the aftermath period (March 2021 – December 2022). (Left) for all available stations, (Right) only for stations at epicentral distances < 30 km. Letters "C" and "D" denote Compression and Dilatation, respectively. The "Null" row indicates "missed" FMPs, while the "Null" column corresponds to additional automatic FMPs missing from the manual dataset.

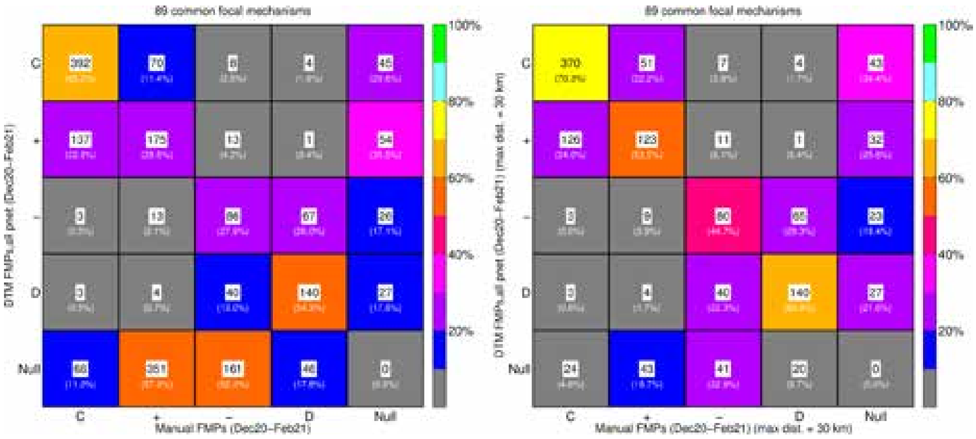

Figure 4. Same as Figure 3, but for the crisis period (December 2020 – February 2021). Symbols "+" and "-" denote emergent, whereas letters "C" and "D" denote impulsive compressional and dilatational FMPs, respectively.

A visual inspection of a subset of identified FMPs alongside the respective P-wave first pulses on the vertical component (e.g., Figure 2, left) confirmed the findings of the confusion matrices, with a generally impressive accuracy of FMP measurement in the majority of instances. There were, however, cases where the polarity of the first motion was seemingly evident to the human eye, but for some reason DTM either dismissed the measurement or misjudged the polarity. As previously noted, null measurements were mostly observed at more distant stations, where the first motion usually has a larger-period pulse than at stations near the epicenter. Erroneous DTM measurements mainly occurred in instances where the P-wave arrival-time pick was not accurate enough, which may be attributed to the applied filter during picking. We tested re-picking on the vertical component with Phasenet, retaining the P-wave pick that was found within ±1 sec of the previously available pick. When the DTM model was re-applied, some results were changed, with new FMPs added, but also with some polarities being reversed and, in some cases, previous FMP measurements being rejected. For the dataset of the 2020-2021 crisis period, the confusion matrix showed an accuracy of 89% and 80% for positive and negative polarities, respectively, taking into account stations at epicentral distances < 30 km and excluding accelerometric stations, after re-picking the P-waves with PhaseNet.

Concerning the focal mechanisms, the similarities between the solutions of the automated workflow with DTM+HASH and those with manually measured FMPs and a grid-search over all fault plane solutions that satisfy a minimum percentage of measured FMPs are quite strong (Figures 5 and 6). HASH was configured to allow for one (1) assumed erroneous FMP for each event. Most of the common solutions with quality grade A, for both the crisis and aftermath periods, exhibit a Kagan angle of less than 30°. Larger deviations can be visibly noticed as a rotation in the focal sphere, mainly affecting the strike-slip component of the focal mechanism. Although the DTM+HASH solutions usually include fewer FMPs than the manual ones, the additional measurement of the S-to-P amplitude ratio likely helps with providing a constrained solution. However, the lack of data from some local stations, particularly for small-magnitude events, can significantly reduce the available FMPs, making the derivation of a quality grade A focal mechanism more difficult. This is especially true during the crisis period (Figure 5), as several local stations experienced technical issues that were later resolved during the aftermath period. Significant differences may also occur as the manual solutions were constrained by the addition of FMP measurements at more distant HUSN stations, where the DTM approach seems to fail to measure the FMP, as also happens sometimes at accelerometric stations due to low SNR. Figure 6 shows a comparison between 57 common solutions of manual and DTM+HASH grade A solutions for the aftermath period, indicating very similar focal mechanisms in both cases, with few notable discrepancies.

Figure 5. Focal mechanisms of 31 earthquakes during the crisis period, (Left) derived from manually determined FMPs and grid-search over adequate fault plane solutions, (Right) derived with DTM+HASH. The common events presented are those for which the DTM+HASH solutions yielded a quality grade A.

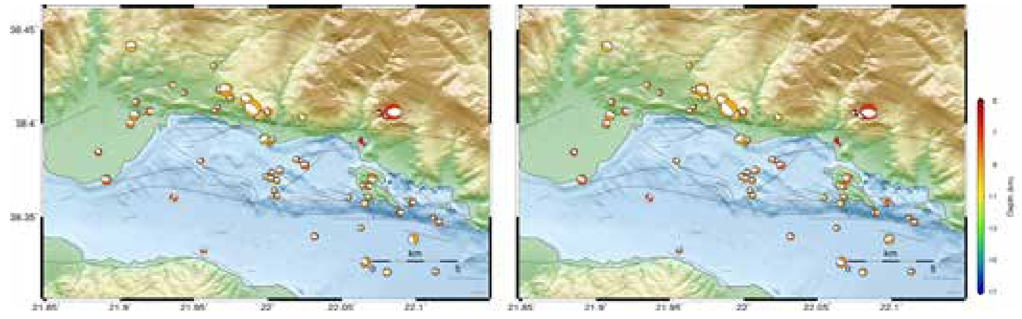

Figure 6. Same as Figure 5, but for the focal mechanisms of 57 common earthquakes during the aftermath period.

Conclusions

In this work, we showcased an application of the DiTing-Motion machine-learning model to fully automate the procedure of first motion polarity measurements in order to determine focal mechanisms of small earthquakes in the Western Gulf of Corinth, Central Greece. As with other methods that employ artificial intelligence, this is a useful tool that can automatically extract a large amount of information that was previously unavailable. We assess the accuracy of the model to identify the polarity of the first motion and examine the cases where it rejects or produces an erroneous measurement. The method requires the availability of accurate P-wave arrival picks at local velocimetric stations for best results. With enough FMP data, even allowing for 1 or 2 erroneous measurements, an accurate focal mechanism can be determined. Despite the abovementioned issues, the results are still remarkable, given that they were produced with a model that was trained with a completely different dataset at a different site. As ML models can be improved by re-training, using site-specific data, this method is promising, regarding the generation of large datasets of focal mechanisms of small earthquakes. The latter could be useful for studies of fault geometries, spatial stress patterns, and even temporal stress changes prior to impending large earthquakes.

Acknowledgements

Waveform data from the following networks were used: CL (Corinth Rift Laboratory Team And RESIF Datacenter, 2013), HA (University of Athens, 2008), HP (University of Patras, 2000), HL (National Observatory of Athens, Institute of Geodynamics, Athens, 1975), and HT (Aristotle University of Thessaloniki, 1981). Maps were drawn using the Generic Mapping Tools (GMT) software (Wessel and Smith, 1998). This research is partially funded by the “TowaRds AdvaNced multidiSciplinary Fault ObseRvatory systeMs²” (TRANSFORM²) project, which is funded by the European Union under project number 101188365 within the HORIZON-INFRA-2024-DEV-01-01 call (Special Account for Research Grants of NKUA, project code: 21465).

References

Aristotle University of Thessaloniki, 1981. Aristotle University of Thessaloniki Seismological Network. International Federation of Digital Seismograph Networks. https://doi.org/10.7914/SN/HT]

Avallone, A., Briole, P., Agatza-Balodimou, A.M., Billiris, H., Charade, O., Mitsakaki, C., Nercessian, A., Papazissi, K., Paradissis, D., Veis, G., 2004. Analysis of eleven years of deformation measured by GPS in the Corinth Rift Laboratory area. Comptes Rendus Geosci. 336, 301–311. https://doi.org/10.1016/j.crte.2003.12.007]

Corinth Rift Laboratory Team And RESIF Datacenter, 2013. CL - Corinth Rift Laboratory Seismological Network (CRLNET). RESIF - Réseau Sismologique et géodésique Français. https://doi.org/10.15778/RESIF.CL

Chiaraluce, L., Festa, G., Bernard, P., Caracausi, A., Carluccio, I., Clinton, J.F., Di Stefano, R., Elia, L., Evangelidis, C.P., Ergintav, S., Jianu, O., Kaviris, G., Marmureanu, A., Šebela, S., Sokos, E., 2022. The Near Fault Observatory community in Europe. Annals of Geophysics 65, 3, DM316. https://doi.org/10.4401/ag-8778

Evangelidis, C.P., Triantafyllis, N., Samios, M., Boukouras, K., Kontakos, K., Ktenidou, O.-J., Fountoulakis, I., Kalogeras, I., Melis, N.S., Galanis, O., Papazachos, C.B., Hatzidimitriou, P., Scordilis, E., Sokos, E., Paraskevopoulos, P., Serpetsidaki, A., Kaviris, G., Kapetanidis, V., Papadimitriou, P., Voulgaris, N., Kassaras, I., Chatzopoulos, G., Makris, I., Vallianatos, F., Kostantinidou, K., et al., 2021. Seismic Waveform Data from Greece and Cyprus: Integration, Archival, and Open Access. Seismol. Res. Lett. 92, 1672–1684. https://doi.org/10.1785/0220200408

Ganas, A., Oikonomou, I.A., Tsimi, C., 2013. NOAfaults: a digital database for active faults in Greece. Bull. Geol. Soc. Greece 47, 518. https://doi.org/10.12681/bgsg.11079

Hardebeck, J.L., 2002. A New Method for Determining First-Motion Focal Mechanisms. Bull. Seismol. Soc. Am. 92, 2264–2276. https://doi.org/10.1785/0120010200

Hardebeck, J.L., Shearer, P.M., 2003. Using S/P amplitude ratios to constrain the focal mechanisms of small earthquakes. Bull. Seismol. Soc. Am. 93, 2434–2444. https://doi.org/10.1785/0120020236

Kaltsas, C., Kaviris, G., Kranis, H., Kapetanidis, V., 2024. The aftermath of the 2020-2021 seismic crisis in the Western Gulf of Corinth (Central Greece). Proceedings of 39th General Assembly of the European Seismological Commission, ESC2024-S44-622, p. 752.

Kapetanidis, V., Deschamps, A., Papadimitriou, P., Matrullo, E., Karakonstantis, A., Bozionelos, G., Kaviris, G., Serpetsidaki, A., Lyon-Caen, H., Voulgaris, N., Bernard, P., Sokos, E., Makropoulos, K., 2015. The 2013 earthquake swarm in Helike, Greece: seismic activity at the root of old normal faults. Geophys. J. Int. 202, 2044–2073. https://doi.org/10.1093/gji/ggv249

Kaviris, G., Elias, P., Kapetanidis, V., Serpetsidaki, A., Karakonstantis, A., Plicka, V., De Barros, L., Sokos, E., Kassaras, I., Sakkas, V., Spingos, I., Lambotte, S., Duverger, C., Lengliné, O., Evangelidis, C.P., Fountoulakis, I., Ktenidou, O.-J., Gallovič, F., Bufféral, S., Klein, E., Aissaoui, E.M., Scotti, O., Lyon-Caen, H., Rigo, A., Papadimitriou, P., Voulgaris, N., Zahradnik, J., et al., 2021. The Western Gulf of Corinth (Greece) 2020–2021 Seismic Crisis and Cascading Events: First Results from the Corinth Rift Laboratory Network. Seism. Rec. 1, 85–95. https://doi.org/10.1785/0320210021

Michelini, A., Cianetti, S., Gaviano, S., Giunchi, C., Jozinović, D., Lauciani, V., 2021. INSTANCE – the Italian seismic dataset for machine learning. Earth Syst. Sci. Data 13, 5509–5544. https://doi.org/10.5194/essd-13-5509-2021

Mousavi, S.M., Ellsworth, W.L., Zhu, W., Chuang, L.Y., Beroza, G.C., 2020. Earthquake transformer—an attentive deep-learning model for simultaneous earthquake detection and phase picking. Nat. Commun. 11, 3952. https://doi.org/10.1038/

s41467-020-17591-w

National Observatory of Athens, Institute of Geodynamics, Athens, 1975. National Observatory of Athens Seismic Network. International Federation of Digital Seismograph Networks. https://doi.org/10.7914/SN/HL

Papadimitriou, E., Bonatis, P., Bountzis, P., Kostoglou, A., Kourouklas, Ch. & Karakostas, V, 2022. The intense 2020–2021 earthquake swarm in Corinth Gulf: Cluster analysis and seismotectonic implications from high resolution microseismicity. *Pure & Applied Geophysics*, 179, 3121–3155. https://doi.org/10.1007/s00024-022-03135-4

Ross, Z.E., Meier, M., Hauksson, E., 2018. P Wave Arrival Picking and First□Motion Polarity Determination With Deep Learning. J. Geophys. Res. Solid Earth 123, 5120–5129. https://doi.org/10.1029/2017JB015251

Serpetsidaki, A., Kapetanidis, V., Elias, P., Rigo, A., Spingos, I., De Barros, L., Lengliné, O., Bufféral, S., Karakonstantis, A., Bernard, P., Briole, P., Zahradník, J., Kaviris, G., Plicka, V., Sokos, E., Voulgaris, N., 2023. The 2020–2021 seismic sequence in the Western Gulf of Corinth: Insights on the triggering mechanisms through high resolution seismological and geodetic data analysis. Tectonophysics 863, 230011. https://doi.org/10.1016/j.tecto.2023.230011

University of Athens, 2008. Hellenic Seismological Network, University of Athens, Seismological Laboratory. International Federation of Digital Seismograph Networks. https://doi.org/10.7914/SN/HA

University of Patras, 2000. University of Patras, Seismological Laboratory. International Federation of Digital Seismograph Networks. https://doi.org/10.7914/SN/HP

Wessel, P., Smith, W.H.F., 1998. New, improved version of generic mapping tools released. Eos, Trans. Am. Geophys. Union. https://doi.org/10.1029/98eo00426

Zahradnik, J., Aissaoui, E.M., Bernard, P., Briole, P., Bufferal, S., De Barros, L., Deschamps, A., Elias, P., Evangelidis, C.P., Fountoulakis, I., Gallovic, F., Kapetanidis, V., Kaviris, G., Ktenidou, O., Lambotte, S., Lengline, O., Lyon-Caen, H., Noble, M., Plicka, V., Rigo, A., Roumelioti, Z., Serpetsidaki, A., Sokos, E., Voulgaris, N., 2022. An atypical shallow Mw 5.3, 2021 earthquake in the Western Corinth Rift (Greece). J. Geophys. Res. Solid Earth 127. https://doi.org/10.1029/2022JB024221

Zhao, M., Xiao, Z., Zhang, M., Yang, Y., Tang, L., Chen, S., 2023. DiTingMotion: A deep-learning first-motion-polarity classifier and its application to focal mechanism inversion. Front. Earth Sci. 11. https://doi.org/10.3389/feart.2023.1103914

Zhu, W., Beroza, G.C., 2019. PhaseNet: A deep-neural-network-based seismic arrival-time picking method. Geophys. J. Int. 216, 261–273. https://doi.org/10.1093/gji/ggy423

17th INTERNATIONAL CONGRESS
of the Geological Society of Greece

BULLETIN OF THE GEOLOGICAL SOCIETY OF GREECE, SP. PUBL.

EXTENDED ABSTRACT 133

Preliminary results of physicomechanical properties of lightweight mortars using palygorskite as sand replacement

Karachaliou A.T., Vogiatzis D., Kantiranis N.
Dept. of Mineralogy-Petrology-Economic Geology, School of Geology, Aristotle University, Thessaloniki, Greece, akaracha@geo.auth.gr

Introduction

Cements are any kind of solid or liquid fine-grained material that can be used as a binder for aggregates. After mixing with a liquid, which is mainly water, the cements harden and eventually solidify gradually. During this period of time, i.e. the change from harden to solidification, cement acquires its final form but also it develops specific properties (bonding and mechanical strength). Cements are divided either on the basis of their origin, into natural and artificial cements (Mohammed, 1996), or on the basis of the way of solidification and hardening, into air hardening and hydraulic mortars (Legakis, 1954 & Zacharopoulou, 2004).

Mortars are mixtures consisting of one or more cements, aggregates, any other special materials and mainly water and/or other mixing liquids. The strength of the mortars is mainly dependent on the type of aggregates they contain. Before drying they have good plasticity, but also workability, while after setting and hardening they develop high compressive strength, but also physical and chemical properties that depend on the materials they contain. Lightweight mortars are a subcategory of mortars. These are those with an apparent density of a dry powdered mortar of less than or equal to 1500 kg/m^3 (1.5 g/cm^3) according to ELOT EN 1015-10 (2000). They are characterized by low specific weight and high porosity. Depending on the aggregates used to prepare them, they can be fire-resistance or have sound and heat insulation properties. In general, the category of lightweight mortars is one of the many categories of mortar classification based on specific characteristics such as specific weight, application, type of cement, type of aggregate, etc. (Papagianni, 2000 & Vogiatzis, 2009).

According to the Greek Concrete Technology Regulation (2016), aggregates are defined as all those materials of geological or industrial origin, which are used either together with some kind of cement (in order to create mortars, concretes, etc.), or on their own in all kinds of technical works. This includes natural or artificial materials used either in their original form or after crushing, grinding or grading for the production of concrete and other applications. Included raw materials for the production of lime, cement or metallurgical fluxes.

The natural materials used in mortars include, among others, pumice, zeolites, vermiculite, perlite, diatomite, etc., while the artificial materials include fly ash, blast furnace slag, etc. The use of clays, particularly those rich in palygorskite, has not been studied in this particular application as a substitute for conventional sand for the production of lightweight mortars.

Palygorskite is a hydrated magnesium aluminosilicate mineral with the general chemical formula $(Mg,Al)_2Si_4O_{10}(OH)\cdot 4(H_2O)$. It occurs in the form of elongated (vacuum tube type) crystals and a structure that can be characterized as chain type. When dispersed its crystals remain inert and without any expansion. It retains liquids and gives thickening, thixotropic and other properties. It has a highly porous structure which makes it a very absorbent material but also shows resistance to high temperatures and to environments of high salinity and alkalinity.

The aim of this study is to evaluate the ability of a clay rich in palygkorskite from the Ventzia basin of the region of Grevena, Macedonia, Greece, in the preparation of lightweight mortars when used as a partial substitute of sand. A mixture was prepared, and standard samples were used to evaluate specific physicomechanical properties such as specific weight, porosity, uniaxial compressive strength and mineralogical composition of the standard samples of the prepared mixture.

Materials and methods

The materials used in the present work, for the creation of the mixtures, are palygorskite from the company Geohellas SA, commercial quality sand, which comes from the riverbed of the Axios river and Portland cement type CEM II/B-M 42.5 from the company ISOMAT. For the present study, ten 5 cm cubic specimens were prepared according to ASTM C109/109M, in which 50% of the sand was replaced by palygorskite and the specific weight, porosity, uniaxial compressive strength and mineralogical composition were evaluated for hardening period of 3, 7, 28 and 90 days. For the evaluation of the results, standard specimens were used which were prepared in previous work (Vogiatzis, 2009).

The specific weight was obtained as the result of dividing the volume of each cubic specimen by its weight after weighing on a high precision balance and is expressed in units of g/cm^3. This constitutes the most important property for classifying a mortar as lightweight. The porosity was calculated from the formula of Wyllie *et al.* (1956):

$$\frac{1}{Vp}=\frac{\varphi}{Vpf}+\frac{1-\varphi}{Vpm}$$

where the velocity V_p of primary (P) waves, in a material with porosity φ is given by the above relation in which V_{pf} is the velocity of wave travelling through the material with which the pores of the rock are filled, whether this is air (330 m/sec) or water (1,450 m/sec), and V_{pm} is the velocity of the wave travelling through the studied material without pores. The V_{pm} value used for this work is 5,840 m/sec (Berge *et al.,* 1995). A Pundit Lab type ultrasonic device was used to measure the velocity of the primary (P) waves in the studied specimens.

For the evaluation of the uniaxial compressive strength, a hydraulic press was used directly on the prepared specimens. The strength is calculated as the ratio of the value of the applied crushing force to its applied area, with the result given in MPa.

In order to determine the mineralogical composition of the samples both quantitatively and qualitatively, the X-ray diffraction method was used on a powder sample. A Bruker diffractometer (D8 ADVANCE), Cu tube and Ni filter were used to isolate $Cu_{K\alpha}$ radiation, at operating conditions of 40 kV & 40 mA, for a scanning range of 3-63° 2θ, step 0.02° and a step time of 0.25 sec. The results were qualitatively evaluated using the DIFFRAC.EVA (v7.1) software with PDF4+ (2004) database, while the quantification of the minerals identified was performed using Bruker's DIFFRAC.TOPAS v6 (2018).

All measurements were conducted in the laboratories of the School of Geology of Aristotle University of Thessaloniki.

Results and discussion

Concerning the raw materials, the sand mainly consists of feldspars, quartz and mica, while minor amounts of amphibole chlorite, serpentine and talc were also measured. As for the clay, the mineralogical analysis showed that it consists mainly of palygorskite (90 wt.%) and in minor amounts of serpentine and chlorite. The mineralogical analysis of the cement showed that it consists of hatrurite (33 wt.%), larnite (24 wt.%), anhydrite (12 wt.%), calcite (12 wt.%), dolomite (10 wt.%), gypsum (5 wt.%), brownmillerite (3 wt.%) and quartz (1 wt.%). In figure 1 the X-ray patterns of the raw materials were shown.

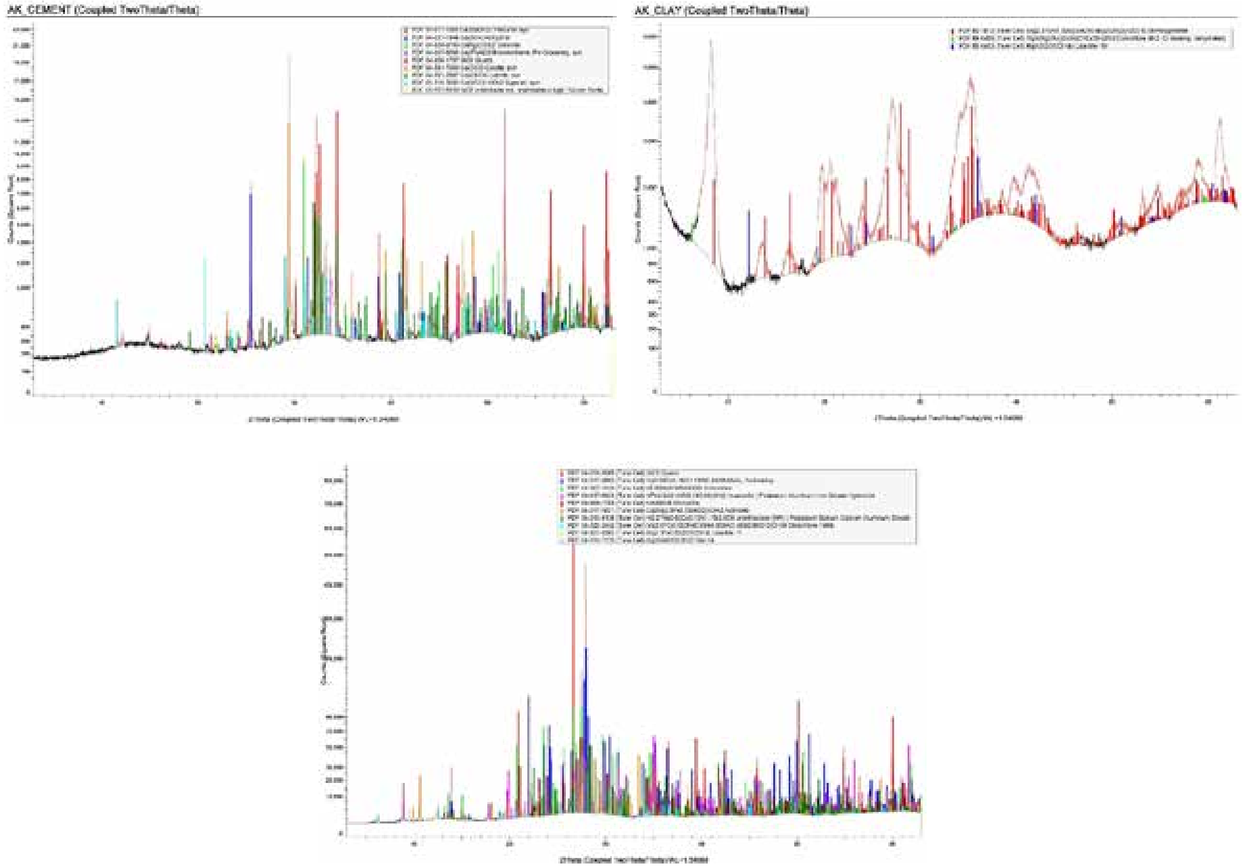

Figure 1. X-ray patterns of the raw materials (cement, clay, sand).

The physical properties of the studied mortar are presented in Table 1. Regarding the specific weight, the studied mortar does not show any change in the first 3 (1.298 g/cm^3) and 7 (1.300 g/cm^3) days, while a significant change in the specific weight occurs on the 28th (1.114 g/cm^3) day, which becomes more obvious on the 90th (0.731 g/cm^3) day. This continuous decrease in specific weight is caused by the porous structure of the palygorskite and the loss of water from the pores of the specimen throughout its compaction mainly due to hardening reactions and secondly to its contact with the atmosphere. This results in a relatively large and continuous final reduction in the specific weight of the mortar (90 days 0.731 g/cm^3) of 43.7% compared to the initial values (3 days 1.298 g/cm^3).

The velocity of the primary (P) waves (Tab. 1) has a decreasing trend from day 7 to day 90 which is mainly due to the increase in porosity during the same period. At 3 days of hardening the average P-wave velocity was measured 1414 m/sec, which at 90 days was measured at 1068 m/sec, i.e. the P-wave velocity at 90 days decrease to approximately 25% of the 3-day value. Standard cement:sand mortar (conventional mortar) shows at 90 days a P-wave velocity of 3.126 m/sec, while zeolitic mortar (50 wt.% replacement of sand by natural zeolite) specimens showed after 90-day of hardening a P-wave velocity of 2.736 m/sec (Vogiatzis *et al.,* 2008 & Vogiatzis, 2009).

Porosity, which is negatively correlated with P-wave velocity (Wyllie *et al.* 1956), showed an increasing trend throughout the hardening period. In the first week (3 and 7 days) of hardening a relatively similar values of 28.9 and 30.7% v/v, were calculated, while after 28 and 90 days of hardening porosity gradually increases to 35.9 and 38.7% v/v, respectively. This variation in porosity can be attributed to the porous structure of palygorskite, the gradual removal of pore water after day 7 until the end of hardening, but also to the hardening reactions that take place until the 90th day.

Table 1. Measurements of the physical properties of the mortar under testing.

Sample	Consolidation days	Specific weight, S.W. (g/cm^3)	Average value of S.W.	Vpx (m/sec)	Vpz (m/sec)	Vpy (m/sec)	Average Vp (m/sec)	Porosity (% v/v)
K3.1	3	1.390	1.298	1450	1405	1400	1414	30.7
K3.2		1.207		1398	1444	1387		
K7.1	7	1.364	1.300	1526	1522	1509	1525	28.9
K7.2		1.236		1408	1594	1589		
K28.1	28	1.114	1.114	1184	1143	1108	1172	35.9
K28.2		1.086		1126	1169	1154		
K28.3		1.125		1234	1235	1194		
K90.1	90	0.731	0.731	1026	1042	1065	1068	38.7
K90.2		0.686		1141	1188	1225		
K90.3		0.778		1044	958	923		

Uniaxial compression tests showed low strength values, varying from 1.6 MPa at 3 days to 1.0 MPa at 90 days of hardening. The uniaxial compressive strength values show an inversely proportional variation with P-wave velocity and porosity (Fig. 2), a behavior that is attributed to the increase of empty spaces in the specimens from the studied mortar which cause their break by applying a smaller force on the same specimen surface (Kantiranis *et al.,* 2000 & Kantiranis, 2001, Vogiatzis *et al.,* 2008).

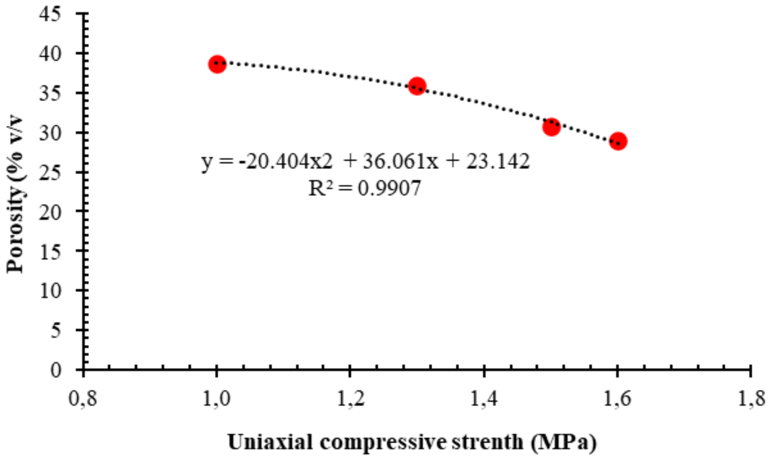

Figure 2. Variation of uniaxial compressive strength (MPa) with porosity (% v/v).

Mineralogical analysis of the studied mortar sample (Fig. 3) showed that the quantities of the mineral constituents (quartz, feldspar, mica, amphibolite, olivine, dolomite, calcite, chlorite, serpentine and palygorskite) of the original materials remain stable compared to the 90 days of compaction, with some variations in the relative variation of these phases on the intermediate days of compaction (3, 7 and 28 days). As for the cement phases, brownmillerite, tobermorite and larnite show stable values with relatively low percentages, while hatrurite shows an increase of 14% between day 3 and day 28. Finally, portlandite remains stable for the first 28 days, then gradually decreases, reaching a very low rate (0.5% w/w) on day 90. The findings of the present study are similar to previous studies, e.g. Vogiatzis *et al.* (2012).

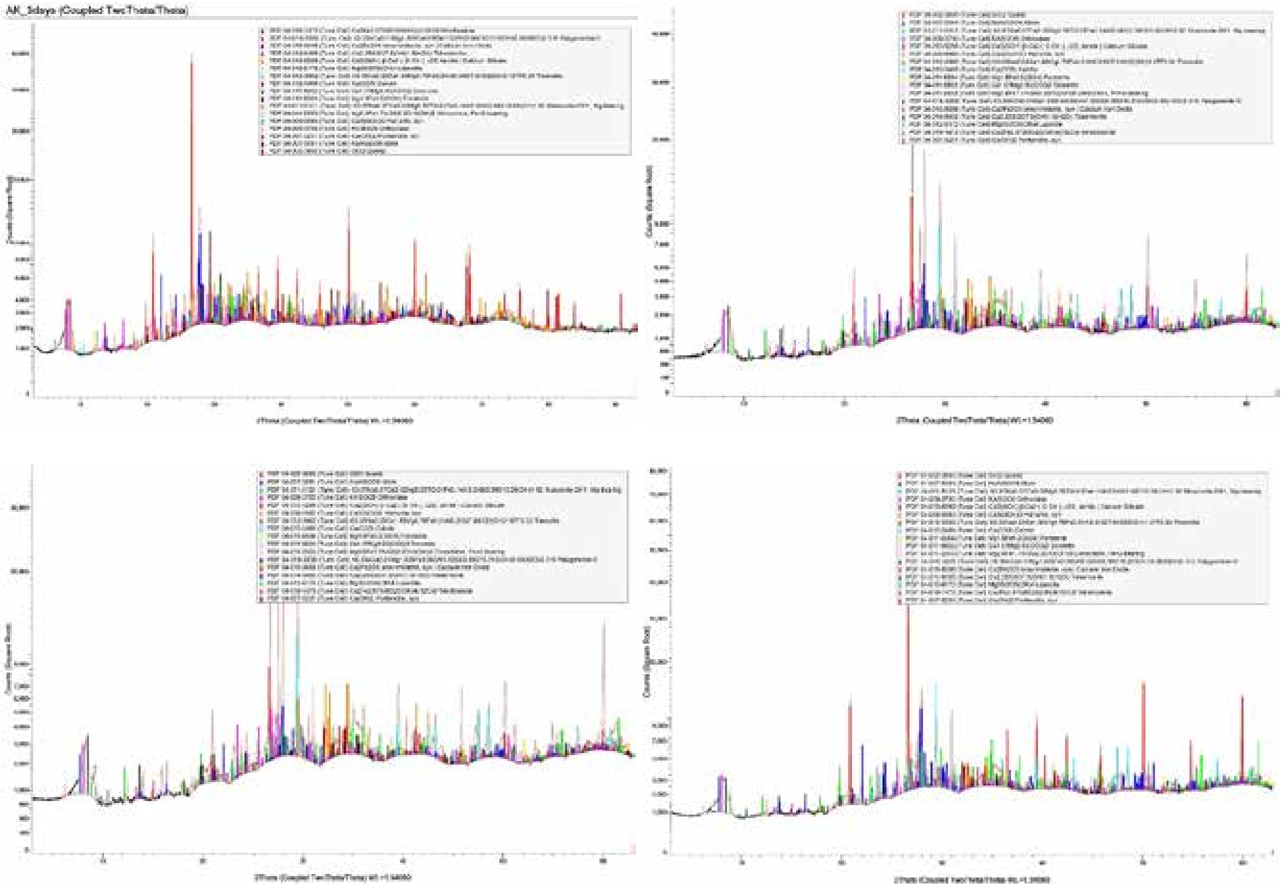

Figure 3. X-ray patterns of the studied mortar at 3, 7, 28 and 90 days of hardening.

It is worth mentioning that the use of clay minerals in mortars, more specifically that of palygorskite, can provide useful properties to the final products, which are the higher porosity and lower specific weight compared to conventional mortars or mortars using natural zeolites. Specifically, Table 2 presents the physical and mechanical properties of three different mortars: the conventional mortar (sand-cement-water) according to ASTM C109-109M (2002), the mortar with 50% wt. replacement of sand by natural zeolite and the mortar with 50% wt. replacement of sand by palygorskite clay. From the evaluation of the data in Tab. 2 it is clear that the use of palygorskite clay produces a much lighter mortar compared to both other mixes. It is observed a decrease in specific weight and an increase in porosity due to the unique microstructure (vacuum tube type) of palygorskite, which decisively affects the development of the final characteristics of the studied mortar. This variation is also observed in the mortar with natural zeolite content, which although not very pronounced, is attributed to the macro, micro & nano pores of zeolitic rock and the contained zeolite (clinoptilolite), respectively. In addition, the cementation and hardening reactions of the mortars play an important role in the change in specific weight and porosity, with zeolitic water having a significant influence on the progression and completion of these reactions (Vogiatzis, 2009).

Table 2. Comparative results of the physical and mechanical properties of mortars with different aggregates.

Samples	**Specific weight (g/cm^3)**	**Porosity (% v/v)**	**Uniaxial strength (MPa)**
Cement:Sand (conventional mortar)	1.869	19.0	14.6
Cement:1/2Sand:1/2 Natural zeolite	1.657	25.0	9.0
Cement:1/2 Sand:1/2 Palygorskite clay	0.731	38.7	1.0

Regarding the uniaxial compressive strength of these three mortars, the use of sand as the only aggregate (conventional mortar) produces the mortar with the highest strength values compared to mortars with natural zeolite rich in clinoptilolite and clay rich in palygorskite, since both these components, with their porous structure, give the mortars a higher porosity and therefore lead to lower uniaxial compressive strength. In comparison between mortars with clinoptilolite and those with palygorskite, the use of natural zeolite leads to higher uniaxial compressive strength values. According to ELOT EN 998-2 (2003), the mortar with palygorskite is classified as M1 (class with minimum compressive strength of 1 MPa), while that with natural zeolite is classified in M5 (class with minimum compressive strength of 5 MPa).

The specific weight was measured at lower values both in the mortar with palygorskite and in the one with natural zeolite, compared to the conventional mortar. Between them the mortars with sand replacement show a relatively large difference in specific weight, with palygorskite clay providing the mortar with values up to 50% lower than those of the mortar with natural zeolite. According to ELOT EN 1015-10 (2009), the specific weight value of palygorskite mortar meets the criteria for lightweight mortars.

Therefore, the addition of palygorskite clay can provide mortars with properties that classify them as lightweight, thus allowing their application in special uses, such as for thermal insulation, sound insulation, etc.

Conclusions

In the present study, the preparation and properties of lightweight mortars were studied through the partial replacement of sand, which is a basic aggregate component of conventional mortars, by palygorskite-rich clay, which is a natural clay material. The materials used include CEM II/B-M 42.5 type cement of the company ISOMAT, commercial sand from the Axios riverbed and palygorskite clay of GEOELLAS S.A. The mixing ratios of cement:aggregates:water were 1:2.75:0.485, with the aggregates consisting equally of sand and palygorskite clay. The aim of this study was to produce a mortar of lower specific weight than conventional mortars, which would be classified as a lightweight mortar, using palygorskite clay as a natural substitute for sand.

The specific weight showed a 43.7% reduction at 90 days, with values varying from 1.298 (3 days) to 0.731 g/cm³ (90 days), with the 90-day value being within the specifications for lightweight mortars. The porosity increased gradually during hardening, mainly due to the removal of pore water from the mixture, but also due to the mirco-structure of the palygorskite. Primary waves (P-waves) velocity showed a 25% decrease from 3 to 90 days of hardening, with mean values decreasing from 1.414 m/sec at 3 days to 1.068 m/sec at 90 days. This decrease is attributed to an increase in porosity, as the velocity of P-waves is inversely proportional to the porosity of a material. Consequently, the uniaxial compressive strength decreased, classifying the studied mortar in class M1 (minimum compressive strength of 1 MPa). Mineralogical analyses of the cement phases showed significant changes. Brownmillerite showed similar values in the first few (3 and 7) days of hardening, with a gradual increase thereafter due to its slow reaction with water. Hatrurite showed a strong increase in the first 28 days of hardening, with a decrease thereafter, as it reacts rapidly with water, contributing to the early increase in the strength of the mortal. Larnite decreased at 90 days of hardening, while tobermorite and portlandite showed constant values or a slight increase at the beginning, followed by a decrease at the end of hardening due to their involvement in hydration reactions. The use of palygorskite clay as a natural aggregate resulted in the production of mortar with low specific weight (0.73 g/cm³) and high porosity (38.7% v/v) at 90 days of hardening, fulfilling the criteria for lightweight mortars. The studied mortar, with 50% substitution of palygorskite clay for sand, was prepared without chemical or other treatment and based on its characteristics it is a lightweight mortar of low specific weight and high porosity.

Finally, further research on mixtures with different percentages of sand replacement by palygorskite-rich clay could lead to a complete evaluation of the specific properties and the identification of the optimal mixture for specific applications, especially in the field of thermal and acoustic insulation, making these mortars a promising material for construction applications.

Bibliography

ASTM C109/C109M, 2002. Standard Test Method for Compressive Strength of Hydraulic Cement Mortars (Using 2-in. or [50-mm] Cube Specimens).

Berge P.A., Bonner B.P., and Berryman J.G., 1995. Ultrasonic velocity□porosity relationships for sandstone analogs made from fused glass beads, Society of exploration geophysicists, Geophysics, Volume 60, Issue 1,January-February 1995.

DIFFRAC.TOPAS V6 (2018). A profile fitting based software for quantitative phase analysis, microstructure analysis and crystal structure analysis. Bruker Corporation, The Netherlands.

ΕΛΟΤ EN 1015-10, 2009. Methods of test for mortar for masonry - Part 10: Determination of dry bulk density of hardened mortar.

ΕΛΟΤ EN 998-2, 2003. Specification for mortar for masonry - Part 2: Masonry mortar.

Kantiranis N., 2001. Calcination study of the crystalline limestone from Agios Panteleimonas, Florina, Greece. PhD Thesis, School of Geology, Aristotle University, Thessaloniki, Greece, 194 p.

Kantiranis N., Christaras B., Filippidis A. and Tsirambides A., 2000. The usage of ultrasonic techniques at calcination studies. *European Commission, Directorate General X, Compatible materials recommendations for the preservation of European cultural heritage, PACT*, 59: 231-237.

Legakis A., 1954. Structural Materials, Library of the Technician, Volume A, Eugenidou Foundation, Athens.

Muhammad M., 1996. Preparation of new mortars with traditional materials for Venetian monuments conservation applications - Study of the compatibility of building stones, their strength and marine corrosion, School of Mineral Resources Engineering, MSc Thesis, Technical University of Crete, Chania.

Papayianni I., Stefanidou M., 2000, Repair mortars for monuments in Byzantine Architecture, 5th International Congress on Restoration of Architectural Heritage, Firenze, 1671-1683.

Regulation on the Technology of Concrete, 2016. Approval of the Concrete Technology Regulation 2016 (CTS-2016). FEK B'1561/2-6-2016, 18057-18171.

Vogiatzis D., 2009. Use of fly ash and natural zeolite in the preparation of lightweight mortars, School of Geology, Ph.D Thesis (in Greek), Aristotle University, Thessaloniki, Greece.

Vogiatzis D., Christaras V., Filippidis A., Kassoli-Fournaraki A., Kantiranis N., Moropoulou A., and Bakolas A., 2008. Evaluation of cement-sand-natural zeolite mortar hardening by ultrasonic techniques. 1st Panhellenic Conference on Structural Materials and Elements, T.C.G., Athens, Greece, Proceedings, B: 1099-1110.

Vogiatzis D., Kantiranis N., Filippidis A., Tzamos E. and Sikalidis C., 2012. Hellenic Natural Zeolite as a replacement of sand in mortar: Mineralogy monitoring and evaluation of its influence on mechanical properties. Geosciences, 2(4), 298-307.

Wyllie M. R. J., Gregory A. R., and Gardner L. W., 1965. Elastic wave velocities in heterogeneous and porous media, Geophysics 21: 41-70.

Zacharopoulou G., 2004. Production of high reactivity building lime suitable for conservation of monuments and historical buildings, School of Civil Engineering, PhD Thesis (in Greek), Aristotle University, Thessaloniki, Greece.

17th INTERNATIONAL CONGRESS
of the Geological Society of Greece

BULLETIN OF THE GEOLOGICAL SOCIETY OF GREECE, SP. PUBL.

EXTENDED ABSTRACT 134

Microtremor array explorations and the importance of local site effect in Western Türkiye

Karagöz Ö.[1], Tan O.[2]

(1) Çanakkale Onsekiz Mart University, Faculty of Engineering, Department of Geophysical Engineering, Çanakkale, Türkiye. ozlemkaragoz@comu.edu.tr

(2) İstanbul University-Cerrahpaşa, Faculty of Engineering, Department of Geophysical Engineering, İstanbul, Türkiye.

Introduction

The seismic hazard analysis aims to minimize the damage by determining local site conditions and peak ground acceleration before an earthquake as much as possible. Engineering geophysical methods are one of the fast and economical ways to determine the strength of the soil that will carry engineering structures, the thickness of the layers, water content, behavior under dynamic load, etc. The surface wave analyses allow to S-wave velocity model of the soil layers from the shallow surface to the engineering/seismic bedrock at a site.

In the last 25 years, seismic hazard studies have become important for seismological and earthquake engineering applications in the world. Turkey is one of the countries that have suffered from destructive earthquakes, especially since the 1999 Kocaeli earthquake. The latest 6 February 2023 Kahramanmaraş earthquakes, defined as catastrophe earthquakes, show that we have not made enough progress in reducing earthquake risk since 1999.

Western Türkiye covers rapidly growing areas and encompasses the main financial and industrial centers, especially Istanbul, which is one of the most populated cities in the world, and the other cities in the Marmara Region, such as Tekirdag, Çanakkale, and Balıkesir are the part of the Marmara Supersite that are a high priority to the geohazard community (Figure 1). Additionally, Izmir, the third biggest city, is also located in western Türkiye and affected by earthquakes.

Historical records show that destructive earthquakes frequently visit the region. In the last century, the 9 August 1912 Mürefte (Mw 7.3) earthquake hit the western part while the 17 August 1999 Kocaeli (Mw 7.4) earthquake destroyed the eastern part of the Marmara Region. The Gokceada earthquake (24 May 2014, Mw 6.9) also affected the west of the region. The last destructive earthquake occurred on 30 October 2020, in the north of Samos Island. Even the Bornova Basin, where the city of İzmir is mainly settled, is 70 km away from the earthquake epicenter, significant damage occurred in the city center because of the tick sediment basin. The number of collapsed, heavily damaged and moderately damaged buildings in İzmir is 54, 676 and 789, respectively. A total of 7,683 buildings were labeled as slightly damaged. Totally 117 people died during the mainshock.

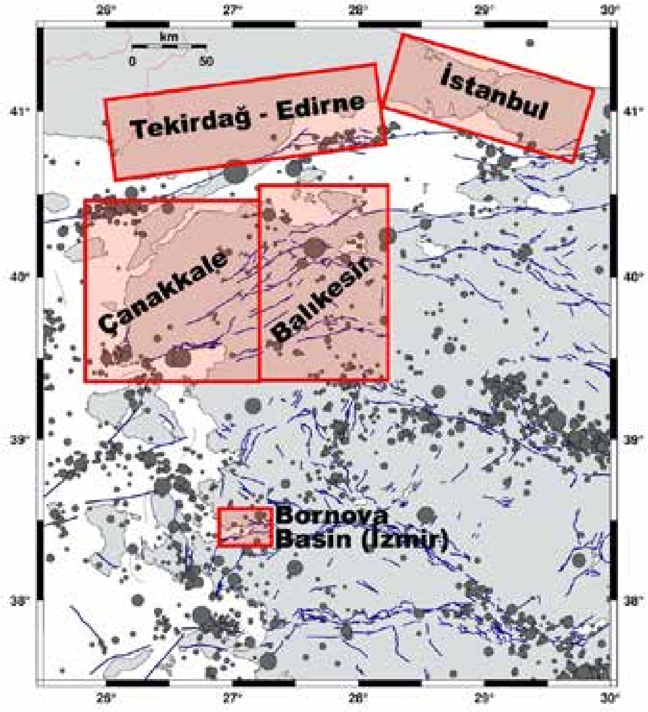

Figure 1. Microtremor study areas in the western Türkiye.

One of the important points for local seismic hazard studies is to define 1D S-wave velocity (Vs) structures from the surface to the seismic or engineering bedrock. This is necessary to know site responses to estimate the ground motion impact on the buildings. The local geology significantly modifies ground motion characteristics and controls the irregular distribution of damage during large earthquakes. Therefore, shallow low-velocity layers are responsible for the variation of earthquake ground motion amplification at a site. Heterogeneity of the soil structures, velocity impedance differences between layers, resonant effects, irregular topography of the layers beneath a basin, the effect of the surface topography, nonlinear soil behavior, fault geometry and lateral variation of Vs causes variation of earthquake ground motion amplifications. It is important to estimate the Vs structure in near-surface layers for estimating strong motion characteristics during an earthquake. Furthermore, investigating the amplification of shallow soil structures is essential as accurately as possible to close the real ones. It is the first step to reduce casualties and collapse buildings before an earthquake for damage assessment. The amplitude, frequency content, and duration of strong ground motions are generally controlled by the local soil structures and have the main role for building damage during an earthquake.

To reduce the earthquake local site effect, a 1D soil profile can be obtained by different geophysical methods, using earthquake data or ambient noise recording to retrieve the vertical soil structure as well as borehole logging. The 1D assumption of the soil structure is widely accepted and easy to implement. Array explorations of microtremors (i.e. SPAC) and MASW methods have been gaining much popularity in the world to obtain 1D Vs profiles. Because they are one of the economic methods and easily applicable for the estimation of Vs structure by a simple circular array with a few seismometers (Figure 2). The Rayleigh waves are considered when vertical sensors are used for microtremor records. Surface wave phase velocity dispersion curves from microtremor records can be utilized to investigate 1D S-wave velocity structures for shallow soil structures.

In this study, the results of array microtremor studies in western Türkiye are presented. The data are collected by the international and national projects from October 2013 to August 2024. The projects were focused on different methods and practices for disaster mitigation for western Türkiye. One of the main research fields of the projects is the determination of the deep and shallow velocity structure for “seismic characterization and damage prediction” that aims to improve the prediction accuracy of estimating the damages induced by strong ground motions.

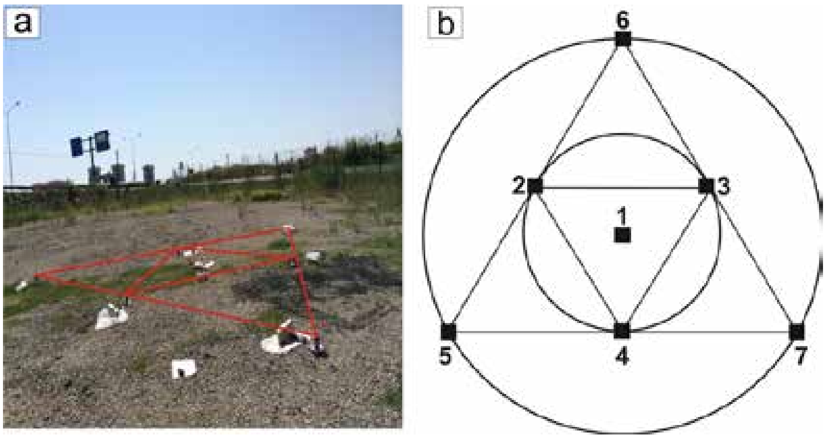

Figure 2. Photo from field measurement in Tekirdag city center (a) and diagram (b) of microtremor array configuration. Numbers show sensor location.

Results and Conclusions

1D Vs structures of shallow sedimentary layers down to the engineering bedrock were explored by applying short-period microtremor Spatial Autocorrelation (SPAC) array measurements (Aki, 1957; Okada, 2003) on the different geological units in Istanbul (Zeytinburnu), Tekirdağ, Edirne, Çanakkale, Balıkesir and İzmir in western Türkiye (Figure 1, 2).

The microtremor array data was gathered with temporarily installed seismic sensors, which were set by using the small and large array circles measurements (Figure 2). Phase velocities of Rayleigh waves were estimated from vertical components of microtremors using the SPAC method proposed by Okada (2003). The SPAC method computes cross-correlations between station pairs in the array with the SPAC coefficients for the calculation of phase velocity at different frequencies. Each vertical-component record was divided into 81.92 s time segments. Then, the transient and artificial noises generated by local conditions, such as pedestrians and cars near the sensors during the measurements, were removed. The Parzen window with a bandwidth of 0.2 Hz was chosen for smoothing in the data processing. We used the 6-14 segments (average 10) for averaging to get the phase velocity at each frequency (Karagoz et al., 2015).

The observed phase velocities were used for the estimation of 1D S-wave velocity structure profiles using the hybrid heuristic method (Yamanaka 2007) as an inversion method to find an optimal S-wave velocity model. This method searches a 1D soil profile by minimizing the misfit function that is defined as a sum of squared differences between the observed and calculated phase velocities. The method used for theoretical dispersion curves of the fundamental mode of Rayleigh waves is based on Haskell (1953). We assumed a horizontally layered, isotropic and homogenous model. The layer model is characterized by four parameters; thickness (h), density (ρ), P-wave velocity (Vp) and S-wave velocity (Vs) for each layer. Thicknesses and shear-wave velocities are the unknown parameters in the inversion. The density was assumed to increase with increasing S-wave velocity. P-wave velocity is not inverted but derived from S-wave velocity by using the empirical relation by Kitsunezaki et al. (1990), defined as

$$Vp = 1.29+1.11*Vs$$

where the units of Vp and Vs are expressed in km/s (Karagoz et al., 2015).

The observed Rayleigh wave phase velocities from field studies were between ~200 and 1000 m/s, ~90 and 930 m/s, ~120 and 850 m/s, ~200 and 1000 m/s in a frequency range from 2 to 30 Hz, respectively, for Zeytinburnu, Tekirdag, Çanakkale and İzmir, respectively. Most of the sites in Tekirdag had predominant frequencies higher than 2 Hz., 0.5 Hz for Zeytinburnu, 0.8 Hz Çanakale, and 0.5 Hz for Izmir (Figure 3). The high amplifications at low frequencies are related to the thick sedimentary layers beneath the cities. Therefore, the reality of the seismic risk of the cities where close to the potential seismic sources (faults) and are on sedimentary basins must be considered for a sustainable future.

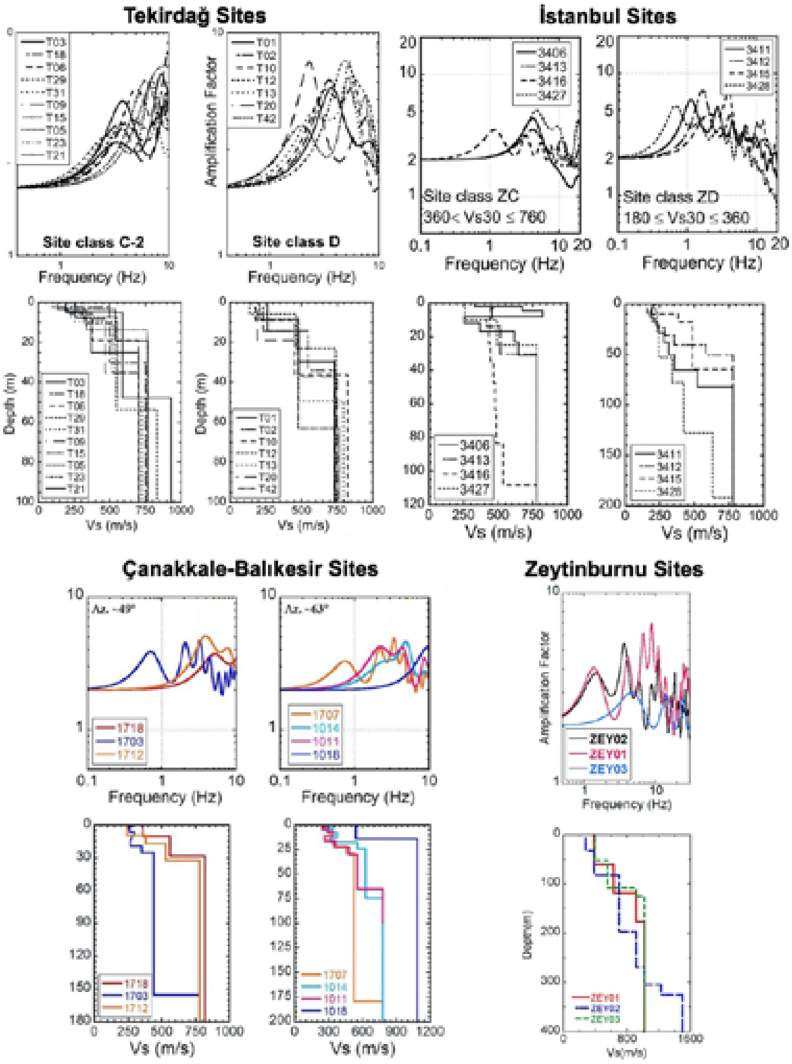

Figure 3. Examples of shallow soil structures and corresponding site amplifications from western Türkiye.

References

Aki, K., 1957. Space and time spectra of stationary stochastic waves, with special reference to microtremors. BERI, 35, 415-456.

Haskell NA (1953) The dispersion of surface waves on multilayered media. Bull Seism Soc Am 43:17–34

Karagoz, O., Chimoto, K., Citak, S., Ozel, O., Yamanaka, H., Hatayama, K., 2015. Estimation of shallow S-wave velocity structure and site response characteristics by microtremor array measurements in Tekirdag region, NW Turkey. Earth, Planets and Space, 67(1), 1-17.

Kitsunezaki C, Goto N, Kobayashi Y, Ikawa T, Horike M, Saito T, Kurota T, Yamabe K, Okuzumi K (1990) Estimation of P- and S-wave velocities in deep soil deposits for evaluating ground vibrations in earthquake. J Japan Soc for Natural Disaster Scie 9:1–17

Okada H., 2003. The microtremor survey method. Geoph. Monog. Series. SEG, 12.

Yamanaka H (2007) Inversion of surface-wave phase velocity using hybrid heuristic search method. Butsuri Tansa 60:265–275. doi:10.3124/segj.60.265 (in Japanese)

17th INTERNATIONAL CONGRESS
of the Geological Society of Greece

BULLETIN OF THE GEOLOGICAL
SOCIETY OF GREECE, SP. PUBL.

EXTENDED ABSTRACT 135

The 2025 seismicity burst in the Santorini – Amorgos seismovolcanic zone

Karakostas, V.[1], Lomax, A.[2], Anagnostou, V.[1], Papadimitriou, E.[1], Acocella, V.[3], Hicks, S.[4], Henry, P.[5]

(1) Geophysics Department, Aristotle University of Thessaloniki, GR54124, Greece, vkarak@geo.auth.gr (2) ALomax Scientific, Mouans Sartoux, France, (3) Universita Roma Tre, Rome, Italy, (4) University College London, UK, (5) Aix Marseille University, CNRS, IRD, INRAE, College de France, CEREGE, Aix–en–Provence, France

Introduction

In January 2025, an intense earthquake activity started in the Santorini volcano area, southern Aegean, causing great concern among the local population and resulting in actions such as school closures and spontaneous evacuation. Seismic activity and geodetic motion increased inside the Santorini caldera in the last second half of 2024, intensifying in mid–January 2025 and extending offshore to the northeast around the Anydros islet between Santorini and Amorgos islands. This activity was remarkably dense, with turbulent variations over space and time (Figure 1). Up to 13 March 2025 over 4000 earthquakes exceeding *M*1.0 occurred and analyzed.

Santorini is an active stratovolcano in the volcanic arc of the Hellenic subduction zone, with several smaller craters in addition to a main caldera, which collapsed around 1625 BC (known as Minoan eruption). Volcanic centers (volcanoes, fumaroles or solfatara fields), epicenters of strong shallow earthquakes (with focal depths up to 20 km) and epicenters of intermediate depth strong earthquakes (with focal depths between 120 and 160 km) in the southern Aegean volcanic arc can be grouped into five well defined, linear clusters trending about N60^{o}E, corresponding to five extensional zones (Papazachos and Panagiotopoulos, 1993).

Regional seismicity is mostly low-rate crustal activity. However, the largest instrumental earthquake in Greece during the 20th century is an *Mw*7.7 rupture in 1956 (Pacheco and Sykes, 1992), just south of Amorgos Island, caused extensive destruction in the southern Aegean. The earthquake ruptured an ENE–striking normal fault that lies parallel to the southern coastline of Amorgos (Papadimitriou et al., 2005). The area of the 2025 swarm coincides with the rupture area of the *M*6.9 main shock, that occurred 13 minutes after the first 1956 M_w7.7 main shock.

Relocated microseismicity recorded by a temporary network deployed in 2003 to investigate microseismicity of the Santorini volcanic center, revealed two clusters. The main cluster was located at the Columbo Reef, which is the top of a submarine volcano, whereas a smaller cluster was located near the Anydros islet, without seismicity inside Santorini caldera, both clusters were aligned in a NE–SW direction (Dimitriadis et al., 2009). During February 2011 an intense microseismicity was initiated within the caldera and lasted until March 2012. In addition to increased seismicity, the volcano showed significant ground uplift, reaching 14 cm within this period (Foumelis et al., 2013). Manual analysis and relocation provided high-resolution image of the activated fault segments (Papadimitriou et al., 2015). The NE–SW activity inside the caldera, with dextral strike slip motion, was rapidly diminished after the activation of an offshore area to its southwest. Normal faulting activity expanded to the northeast offshore area, near Anydros, where the 2025 swarm is manifested. Since 2012, the activity inside the caldera was low and with relative quiescent periods, whereas near Columbo it has been more frequent and continuous (Karakostas and Papadimitriou, 2025).

High–precision earthquake locations

We used the NLL algorithm (Lomax et al., 2000, 2014) and the multiscale high precision NLL–SSST–coherence procedure (Lomax and Savvaidis, 2022) to relocate a manually picked set of earthquakes with data taken from the bulletins from the Geophysics Department of Aristotle University of Thessaloniki (doi:10.7914/SN/HT) and National Observatory of Athens (doi:10.7914/SN/HL) and a set of picks obtained with machine learning (ML). For the relocation of the manually picked earthquakes the recordings of 31 seismic stations were used. Fourteen of them were in operation on Santorini Island since the beginning of our study (January 2024). Seven stations were installed or started their operation after long interruption in February 2025 [Anydros (Feb. 03), Anafi and Amorgos (Feb. 04), Gavrilos (Feb. 07), Astypalaia (Feb. 10), Ios (Feb. 12), Christiana (Feb. 26)]. For the ML picking we analysed waveform data during 1 January–28 February 2025, from 21 broadband stations located in distances up 120 km from the seismicity centroid (https://eida.gein.noa.gr/). The earthquake detection and phase picking were performed by Phasenet (Zhu and Beroza, 2018), a deep–neural–network–based arrival-time picker. Phase picks are then associated using the REAL software (Zhang et al., 2019). REAL is a grid–search phase association algorithm that performs phase association and an initial location of earthquakes, primarily through counting the number of P and S picks that appear within a travel–time curve threshold determined by the user and secondarily from travel time residuals (Zhang et al., 2019).

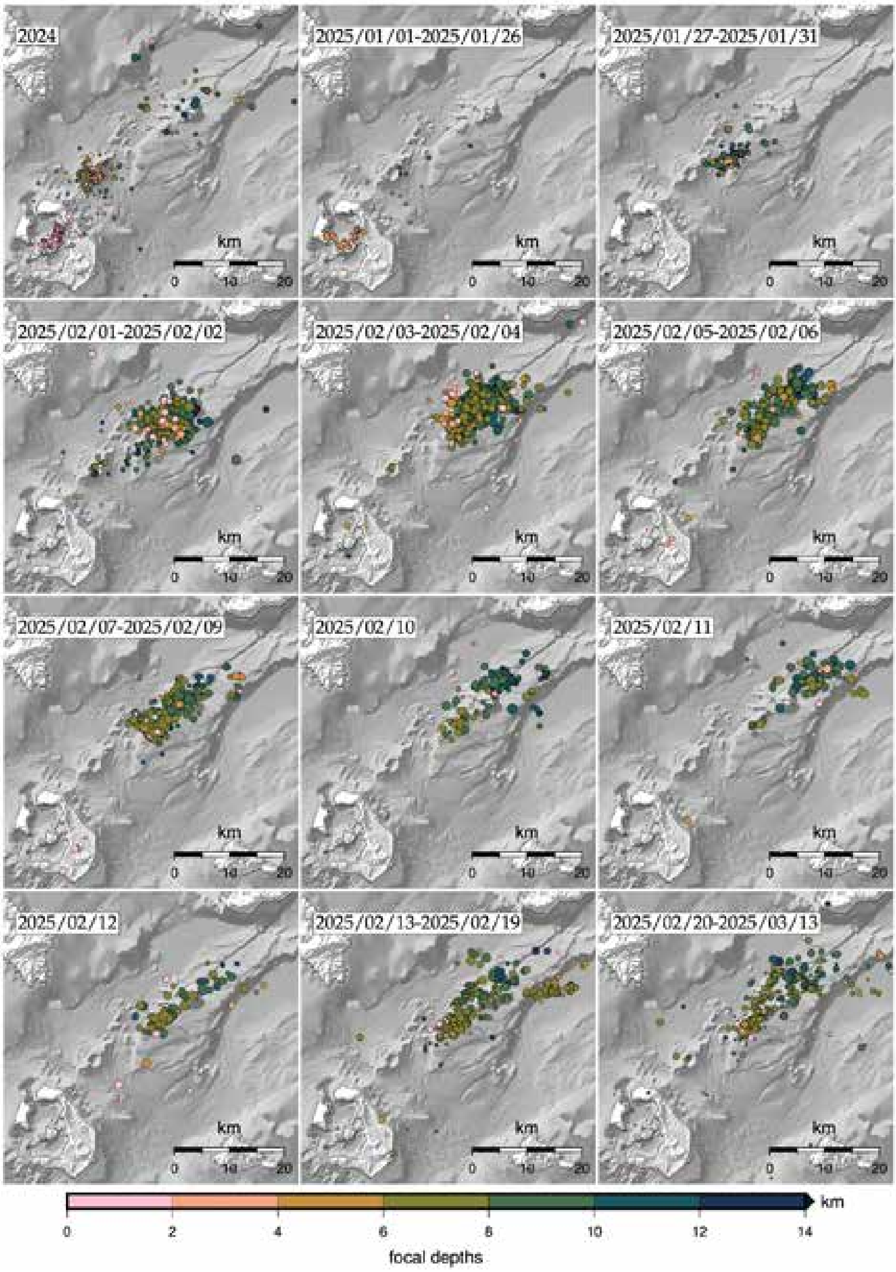

Figure 1. Seismicity evolution in map views for consecutive time windows as indicated inside each snapshot. The size of the symbols is proportional to the earthquake magnitude.

Relocated manually picked seismicity is shown in the maps of Figure 1, covering consecutive time intervals. Background seismicity during 2024 exhibits quite shallow clustering inside Santorini caldera (pink symbols), more dense clustering around the Columbo reef (offshore area NE of Santorini Island) with seismicity up to ~10 km deep, and a third cluster, along with sparse activity, to the northeast and around Anydros islet with focal depths in the brittle crust (5–15 km, inside the seismogenic layer of the back–arc Aegean area, Hatzfeld et al., 1999; among others) with the majority of them getting focal depths between 6–12 km.

With the Machine Learning detection and picking we obtained a catalog with 34442 earthquakes. We relocated the detected seismicity using the same procedure as the manually picked catalogue (Figure 2).

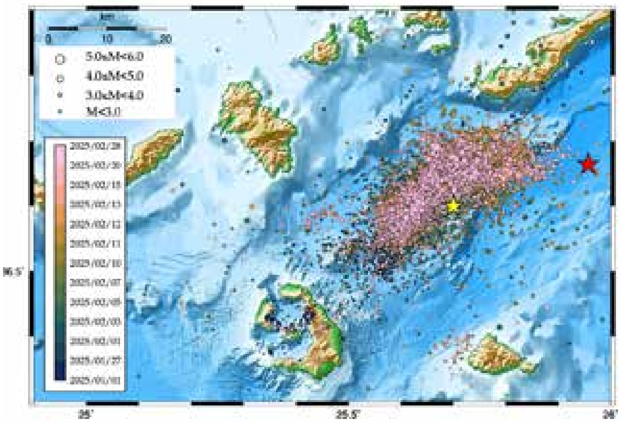

Figure 2. Relocated seismicity during 01/01/2025–28/02/2025 using machine learning detection and NLL–coherence location. The red and yellow stars depict the epicenters of the 1956 M7.7 and M6.9 main shocks, respectively (Bondar et al., 2015; ISC, 2024).

Discussion

Seismic activity intensified during the first weeks of 2025 (1–26 January), including mainly small magnitude seismic activity within the caldera at shallow depths. The main activity abruptly jumped to the northeast offshore area during 27–31 January. Beginning on 1 and up to 4 February, an unusually high number of moderate magnitude earthquakes occurred, the most intense ever reported during the instrumental era anywhere in Greece, with three earthquakes of $M \geq 5.0$ and eighty with $M \geq 4.0$. The activity formed a ~20 km–long NE–SW trend, in accordance with the strike of the 1956 second main shock (M6.9).

The epicentral area of the 2025 swarm was strictly confined within the Anydros basin, which is bounded on both sides by NE–SW striking normal faults. It appears that further migration of the activity along the Amorgos fault zone almost ceased. The shallower focal depths occupy the southwestern part of the seismicity zone, where NE–SW trending small volcanic cones are also located. Over the next two days (on 5 and 6 February) the main seismicity to the northeast became slightly more compact, with 47 (forty–seven) M4+ earthquakes, and around 10 km depth, whereas activity near Columbo decreased. Between 7 and 9 February, 39 (thirty–nine) M4+ earthquakes were concentrated in an even more localized area, but sparser seismicity extends as far as 40 km NE of Santorini. Two additional M5+ earthquakes struck on 10 and 12 February, with the M4+ occurrence rate appearing to decline. The main concentration of activity from 10–11 February migrated and jumped to over 10 km NE of Anydros Island, before rapidly returning back to the SW of Anydros by 12 February. During these last days, when the M4+ activity was more constrained we could distinguish multiple small structures within the fault network that hosts the seismicity burst.

By 13 February, seismic activity had dramatically decreased, to only a few M4+ earthquakes per day, and the last recorded M5+ earthquake on 17 February. From 13 February and through at least 13 March (Figure 1), small clusters took place to the north and eastern edges of the activated area.

Coulomb seismicity–stress imaging of the swarm

The 3D, scalar ΔCFS field due to finite–fault slip or dike opening can be obtained through integration over the fault or dike of the point–source ΔCFS field of stresses due to a point shear dislocation or tensile opening in an elastic half–space (Haskell 1964; Kikuchi & Kanamori 1982; Okada 1992; King et al. 1994; Materna & Wong 2023). This procedure is a forward calculation, with the resulting ΔCFS field often assessed by how well it agrees with the surrounding distribution of seismicity. The corresponding inverse problem is to infer a distribution of finite–fault slip or dike opening given the 3D distribution of aftershocks or other seismicity and the physics of the Coulomb failure stress criteria. Here we infer the space–time distribution of fault slip or dike opening through an imaging methodology: for specified point source slip or dike opening and receiver fault orientations, we obtain 3D maps of extended slip or dike opening through correlation of point–source ΔCFS kernels across the spatial distribution of seismicity. This seismicity–stress procedure finds a 3D distribution of relative fault slip or dike opening which can explain, in accordance with the physics of the Coulomb failure stress criteria, the surrounding distribution of seismicity.

We performed Coulomb seismicity – stress imaging (Lomax, 2025) of the 2025 Santorini – Amorgos earthquake swarm to determine whether the swarm activity could be driven by ΔCFS either from pure normal faulting source (Figure 3) or a vertical dike source with tensile opening (Figure 4). The results for the normal faulting source (Figure 3) show broad lobes of maximum source potential which are separated from and extend far to the northwest and southeast of the swarm seismicity, and which are not parallel to the steep, 65°SE dip of the target normal faulting source. Seismicity-stress imaging supports a given source and receiver configuration when the maximum source potential is a) concentrated within the seismicity distribution and in areas of no or low seismicity, and b) flattened and extended parallel to a source fault or fracture plane orientation. Thus, these seismicity-stress imaging results do not support extended normal faulting as a driver of the swarm seismicity.

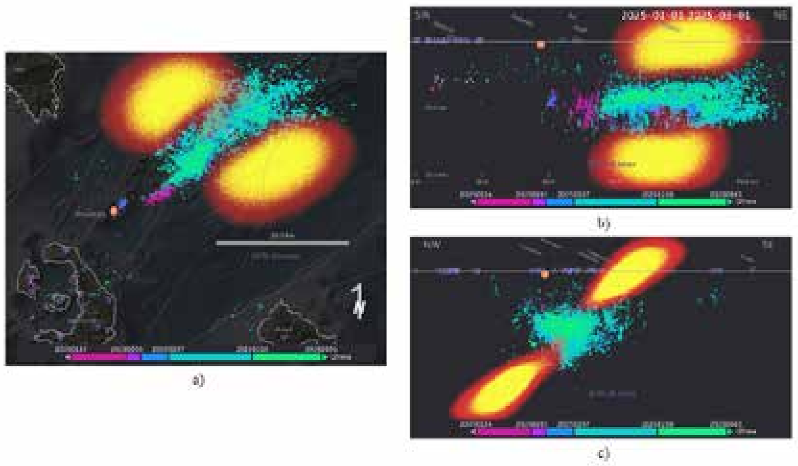

a)

b)

c)

Figure 3. Seismicity-stress imaging of the 2025 Santorini-Amorgos swarm seismicity using a pure normal faulting source specified by a representative mechanism for the M_w7.7, 1956 Amorgos earthquake from Brüstle et al. (2014; strike N36°E, dip 65°SE, rake -102°). 3D density clouds of relative amplitudes of the high-potential portions of the imaged seismicity-stress finite-source fields (yellow and red show normalized correlation ≥ 0.8 and ≥ 0.7, respectively) are shown in a) map view, b) profile view from the SE, and c) profile view from the SW. Dots show NLL-SC-ML relocated swarm seismicity from 2025-01-01 through 2025-02-28, color coded according to occurrence time. Light red lines show mapped surface faults (NOAFaults v6.0); blue inverted pyramids show seismic stations used for ML picking and NLL-SC relocation.

In contrast, the 3D maps of seismicity-stress imaging over the swarm seismicity for a vertical tensile source (Figure 4) show an elongated volume of highest source potential that is mainly below and partly surrounded by the seismicity, abuts high-density limits of the seismicity, is aligned parallel to the trend of the swarm, and is flattened towards a vertical plane. All of these characteristics are compatible with and support a vertical, opening fracture or dyke as a stress source that causes the swarm seismicity.

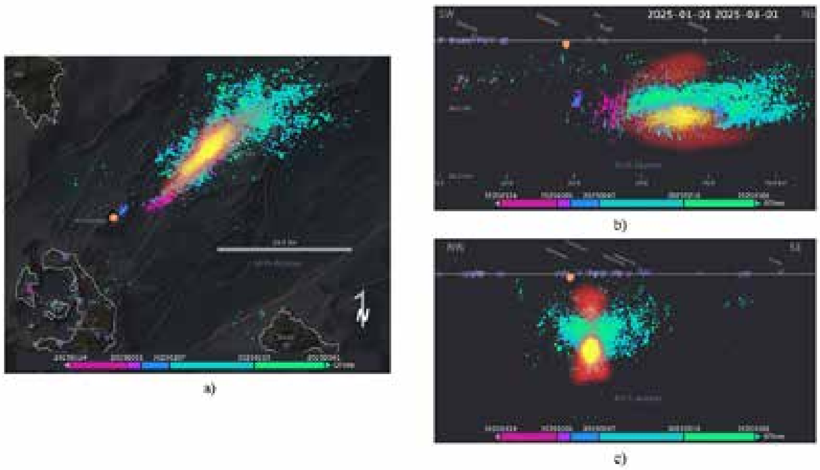

a)

b)

c)

Figure 4. Seismicity-stress imaging of the 2025 Santorini-Amorgos swarm seismicity for a dike source with tensile opening on vertical planes. 3D density clouds of relative amplitudes of the high-potential portions of the imaged seismicity-stress finite-source fields (yellow and red show normalized correlation ≥ 0.8 and ≥ 0.7, respectively) are shown in a) map view, b) profile view from the SE, and c) profile view from the SW. Dots show NLL-SC-ML relocated swarm seismicity from 2025-01-01 through 2025-02-28, color coded according to occurrence time. Light red lines show mapped surface faults (NOAFaults v6.0); blue inverted pyramids show seismic stations used for ML picking and NLL-SC relocation.

Acknowledgements

The authors acknowledge the OSCARS project, which has received funding from the European Commission's Horizon Europe Research and Innovation programme under grant agreement No. 10112975.

OSCARS
Open Science Clusters' Action for Research & Society

Funded by European Union

References

Bondár, I., Engdahl, E.R., Villaseñor, A., J. Harris, J., Storchak, D. A., 2015. ISC-GEM: Global Instrumental Earthquake Catalogue (1900-2009): II. Location and seismicity patterns. Physics Earth Planetary Interiors 239, 2–13, doi:10.1016/j.pepi.2014.06.002.

Brüstle, A., Friederich, W., Meier, T., & Gross, C., 2014. Focal mechanism and depth of the 1956 Amorgos twin earthquakes from waveform matching of analogue seismograms. Solid Earth, 5(2), 1027–1044. https://doi.org/10.5194/se-5-1027-2014

Dimitriadis, I., Karagianni, E., Panagiotopoulos, D., Papazachos, C., Hatzidimitriou, P., Bohnhoff, M., Rische, M., Meier, T., 2009. Seismicity and active tectonics at Coloumbo Reef (Aegean Sea, Greece): monitoring an active volcano at Santorini volcanic center using a temporary seismic network. Tectonophysics 465, 136–149. http://dx.doi.org/10.1016/j.tecto.2008.11.005

Foumelis, M., Trasatti, E., Papageorgiou, E., Stramondo, S. Parcharidis, I., 2013. Monitoring Santorini volcano (Greece) breathing from space. Geophysical Journal International 193, 161–170 doi:10.1093/gji/ggs135

Haskell, N.A., 1964. Total energy and energy spectral density of elastic wave radiation from propagating faults. Bulletin Seismological Society America 54, 1811–1841 doi:10.1785/BSSA05406A1811

Hatzfeld, D., Ziazia, M., Kementzetzidou, D., Hatzidimitriou, P., Panagiotopoulos, D., Makropoulos, K., Papadimitriou, P. and Deschamps, A., 1999. Microseismicity and focal mechanisms at the western termination of the North Anatolian Fault and their implications for continental tectonics. Geophysical Journal International 137, 891–908.

International Seismological Centre, 2024. ISC-GEM Earthquake Catalogue, https://doi.org/10.31905/d808b825

Karakostas, V., Papadimitriou, E., 2025. A review of the relationship between seismicity and volcanic activity in Santorini volcano. AGU Chapman conference, Caldera – Forming Eruptions at Basaltic Volcanoes, Hilo, Hawaii, February 10–14, 2025.

Kikuchi, M., Kanamori, H., 1982. Inversion of complex body waves. Bulletin Seismological Society America 72, 491–506 doi:10.1785/BSSA0720020491

King, G. C. P., Stein, R. S., Lin, J., 1994. Static stress changes and the triggering of earthquakes. Bulletin Seismological Society America 84, 935–953.

Lomax, A., 2025. Mapping finite fault earthquake slip using spatial correlation between seismicity and point source Coulomb failure stress change. Seismica 4(1), https://doi.org/10.26443/seismica.v4i1.1412

Lomax, A., Savvaidis, A., 2022. High–precision earthquake location using source–specific station terms and inter–event waveform similarity. Journal Geophysical Research: Solid Earth 127(1), e2021JB023190. https://doi.org/10.1029/2021JB023190

Lomax, A., Virieux, J., Volant, P., Berge–Thierry, C., 2000. Probabilistic earthquake location in 3D and layered models. In: C. H. Thurber and N. Rabinowitz (Eds.). Advances in Seismic Event Location (vol. 18, pp. 101 – 134). Dordrecht: Springer Netherlands, https://doi.org/10.1007/978-94-015-9536-0_5

Lomax, A., Michelini, A., Curtis, A., 2014. Earthquake Location, Direct, Global-Search Methods. in Encyclopedia of Complexity and Systems Science, pp. 1–33, ed. Meyers, R.A., Springer New York. doi:10.1007/978-3-642-27737-5_150-2

Materna, K., Wong, J., 2023, May 20. Elastic_stresses_py (version 1.0.0). https://github.com/kmaterna/Elastic_stresses_py, Zenodo. doi:10.5281/zenodo.7951979

Okada, Y., 1992. Internal deformation due to shear and tensile faults in a half–space. Bulletin Seismological Society America 82, 1018–1040.

Pacheco, J. F. and Sykes, L. R. (1992). Seismic moment catalog of large shallow earthquakes, 1900 to 1989. Bulletin Seismological Society America 82, 1306–1349.

Papadimitriou, E. E., Sourlas, G., Karakostas, B. G., 2005. Seismicity variations in the southern Aegean, Greece, before and after the large (Mw7.7) 1956 Amorgos earthquake due to evolving stress. Pure Applied Geophysics 162, 783–804.

Papadimitriou, P., Kapetanidis, V., Karakonstantis, A., Kaviris, G., Voulgaris, N. and Makropoulos, K., 2015. The Santorini Volcanic Complex: a detailed multi – parameter seismological approach with emphasis on the 2011–2012 unrest period. Journal Geodynamics 85, 32–57. http://dx.doi.org/10.1016/j.jog.2014.12.004

Papazachos, B. C., Panagiotopoulos, D. G., 1993. Normal faults associated with volcanic activity and deep rupture zones in the southern Aegean volcanic arc. Tectonophysics 220, 301–308.

Zhang, M., Ellsworth, W. L. and Beroza, G. C., 2019. Rapid Earthquake Association and Location. Seismological Research Letters 90(6), 2276–2284. https://doi.org/10.1785/0220190052

Zhu, W. and Beroza, G. C., 2019. PhaseNet: a deep-neural-network-based seismic arrival-time picking method. Geophysical Journal International 216(1), 261–273. https://doi.org/10.1093/gji/ggy423